NEAR-IR ABSORBING BODIPY FUNCTIONALIZED SPIONs: A POTENTIAL MAGNETIC NANOPLATFORM FOR DIAGNOSIS AND THERAPY

A THESIS
SUBMITTED TO THE MATERIALS SCIENCE AND NANOTECHNOLOGY
PROGRAM OF THE GRADUATE SCHOOL OF ENGINEERING AND SCIENCE
OF BİLKENT UNIVERSITY
IN PARTIAL FULFILLMENT OF THE REQUIREMENTS
FOR THE DEGREE OF
MASTER OF SCIENCE

By
ELİF ERTEM
JULY 2012

I certify that I have read this thesis and that in my opinion it is fully adequate, in scope and in quality, as a thesis of the degree of Master of Science.

………………………………….
Prof. Dr. Engin U. Akkaya (Principal Advisor)

I certify that I have read this thesis and that in my opinion it is fully adequate, in scope and in quality, as a thesis of the degree of Master of Science.

………………………………….
Assist. Prof. Dr. Salih Özçubukçu

I certify that I have read this thesis and that in my opinion it is fully adequate, in scope and in quality, as a thesis of the degree of Master of Science.

………………………………….
Assoc. Prof. Dr. Mustafa Özgür Güler

Approved for the Graduate School of Engineering and Science:

………………………………….
Prof. Dr. Levent Onural
Director of the Graduate School of Engineering and Science

ABSTRACT

NEAR-IR ABSORBING BODIPY FUNCTIONALIZED SPIONs: A POTENTIAL MAGNETIC NANOPLATFORM FOR DIAGNOSIS AND THERAPY

Elif Ertem

M.S. in Materials Science and Nanotechnology
Supervisor: Prof. Dr. Engin U. Akkaya
July, 2012

Photodynamic therapy (PDT), especially with the recent advances in photosensitizer design has already been established as a noninvasive technique for cancer treatment. In PDT, photosensitizers (PSs) are targeted to tumor sites either actively or passively, and are irradiated with a laser of appropriate wavelength. The stimulated PSs transfer excitation energy to endogenous oxygen converting it to reactive oxygen species (ROS) that can kill tumor cells. Up to now, numerous nanomaterials tailored to suitable size, have been studied for effective delivery of PSs. Recently, Near IR-based absorbing nanomaterials which have a rising potency to implement light-triggered tumor ablation have attracted much attention since near-IR light in the 650–850 nm range penetrates more deeply in tissues. In addition, imaging of these nanomaterials carrying PSs is very important in order to prevent damage to the healthy tissues upon irradiation. Magnetic resonance imaging (MRI) is a powerful technique due to its excellent spatial resolution and depth for *in vivo* imaging. In this study, a multidisciplinary approach was utilized to create MRI active, near IR-based functional nanomaterials. This approach involves (i) nanochemistry to prepare silica coated super paramagnetic iron oxide (core-shell) nanoparticles, (ii) organic chemistry to synthesize four different type of near- IR absorbing Bodipy derivatives as PSs, and (iii) spectroscopy to verify singlet oxygen production. Four different type of Bodipy based PSs were covalently attached to MRI active, biocompatible, and nontoxic nanocarriers and generation of singlet oxygen capabilities were evaluated. It was demonstrated that these core-shell nanoparticles are promising delivery vehicles of PSs for the use in diagnosis and therapy.

Keywords: Bodipy, photodynamic therapy, photosensitizer, magnetic resonance imaging, super paramagnetic iron oxide nanoparticle, core-shell nanoparticle

ÖZET

YAKIN KIZIL ÖTESİ BÖLGEDE ABSORBE EDEN BODIPY TÜREVLERİ İLE FONKSİYONLANDIRILMIŞ SÜPER PARAMANYETİK DEMİR OKSİT NANOPARÇACIKLARI: TANI VE TERAPİ İÇİN POTANSİYEL MANYETİK NANOPLATFORM

Elif Ertem
Malzeme Bilimi ve Nanoteknoloji Programı, Yüksek Lisans
Tez Yöneticisi: Prof. Dr. Engin U. Akkaya
Temmuz, 2012

Fotodinamik terapi, fotoduyarlaştırıcılarda süregelen gelişmelerle birlikte, kanser tedavisinde çoktan yerleşmiş invazif olmayan bir tedavi yöntemidir. Fotodinamik terapide, fotoduyarlaştırıcıya tümörlü bölgeler aktif veya pasif olarak hedefletilir ve lazer ile uyarılır. Uyarılmış fotoduyarlaştırıcılar enerjisini içerdeki oksijene transfer eder, oksijen o enerjiyi tümör hücrelerini öldüren reaktif oksijen türlerine dönüştürür. Şimdiye kadar, uygun boyuta ayarlanmış çok sayıda nanomaddenin fotoduyarlaştırıcıları verimli bir şekilde hedefe ulaştırdıkları gösterilmiştir. Son zamanlarda, ışık uyarısıyla tümör yokedilmesi uygulamalarında yükselen bir potansiyele sahip olduğu için yakın kızıl ötesi bölgesi temelli nanomalzemeler büyük ölçüde ilgi toplamıştır. Çünkü 650–850 nm arası olan yakın kızıl ötesi ışık deride çok daha derinlere ilerleyebilmektedir. Ek olarak, fotoduyarlaştırıcıları taşıyan nanomateryallari görüntülemek uyarma esnasında sağlıklı deriye zarar vermeme açısından çok önemlidir. Manyetik rezonans görüntülemesi (MRI) canlı görüntülemesindeki mükemmel uzaysal çözünürlüğü ve derinliği açısından çok güçlü bir tekniktir. Bu çalışmada, MRI aktif, yakın kızıl ötesi bölgesi temelli fonksiyonel nanomalzemeler hazırlamak için çok disiplinli bir yaklaşım kullanılmıştır. Bu yaklaşım şunları içermektedir: (i) silica kaplı süper paramanyetik demir oksit nanoparçacıklarını hazırlamak için (çekirdek-kabuk), nanokimya, (ii) fotoduyarlaştırıcı olarak yakın kızıl ötesi bölgede absorplayan dört farklı bodipy çeşidini sentezlemek için, organik kimya ve (iii) singlet oksijen ölçümünü kanıtlamak için, spektroskopi. Dört farklı bodipy tabanlı fotoduyarlaştırıcı kovalent olarak MRI aktif, biyouyumlu ve toksik olmayan nanotaşıyıcılara bağlayarak, singlet oksijen üretme kapasiteleri değerlendirilmiştir. Bu çekirdek-kabuk nanoparçalarının tanı ve terapi için fotoduyarlaştırıcı taşımada ümit verici olduğu gösterilmiştir.

Anahtar Kelimeler: Bodipy, fotodinamik terapi, fotoduyarlaştırıcı, manyetik rezonans görüntüleme, süper paramanyetik demir oksit nanoparçacık, çekirdek-kabuk nanoparçacık

ACKNOWLEDGMENT

I would like to express my sincere thanks to my supervisor Prof. Dr. Engin U. Akkaya for his guidance, support, and patience during the course of this research. I am also grateful to him for teaching us how to become a good scientist by looking everything from different point of views. I will never forget his support throughout my life.

I owe a special thank to Ahmet Bekdemir for his partnership in this research. I owe him a lot for his valuable friendship and encouragement.

I would like to thank our group members Esra Eçik Tanrıverdi, Ayşegül Gümüş, Murat Işık, Ruslan Guliyev, Bilal Kılıç, Safacan Kölemen, Sündüs Erbaş Çakmak, Yusuf Çakmak, Seda Demirel, Tuğba Özdemir Kütük, Onur Büyükçakır, İlke Şimşek Turan, Nisa Yeşilgül, Hatice Turgut, Ziya Köstereli, Şeyma Öztürk, Fatma Pir Çakmak, Hande Boyacı, Tuğçe Durgut, F. Tuba Yaşar, Muhammed Büyüktemiz, Taha Bilal Uyar, Ahmet Atılgan, Yiğit Altay, and rest of the SCL members for valuable friendships, wonderful collaborations, and great ambiance in the laboratory. It was wonderful to work with them.

I would like to express my special thanks to my friends Esra Eroğlu, Burçak Dölek, Özden Çelikbilek, Şeyma Ekiz, Çağatay Dengiz, Murat Kadir Deliömeroğlu, and Gizem Çeltek. They were always with me during the course of this research.

I would like to thank to TÜBİTAK (The Scientific and Technological Research Council of Turkey) for financial support during my master studies.

Finally, I want to express my gratitude to Okan Yılmaz and my family especially my parents for their love, support, and understanding. I owe them a lot.

LIST OF ABBREVIATIONS

PDT: Photodynamic Therapy
PS: Photosensitizer
BODIPY: Boradiazaindacene
MRI: Magnetic Resonance Imaging
XPS: X-ray Photoelectron Spectroscopy
ISC: Intersystem Crossing
LED: Light Emitting Diode
ALA: 5-Aminolevulinic acid
BPD-MA: Benzoporphyrin Derivative Monoacid Ring A
FRET: Förster Resonance Energy Transfer
ROS: Reactive Oxygen Species
PEG: Polyethylene Glycol
SPION: Superparamagnetic Ironoxide Nanoparticles
MNP: Magnetic Nanoparticles
PET: Positron Emission Tomography
SPECT: Single Photon Emission Computed Tomography
DMF: Dimethylformamide
THF: Tetrahydrofuran
TFA: Trifluoroacetic Acid
DPBF: 1, 3 Diphenylisobenzofuran
EDAX: Energy Dispersive Analysis X-Ray
APTES: 3-Aminopropyltriethoxysilane
TEOS: Tetraethyl Orthosilicate
TEM: Transmission Electron Microscopy
XRD: X-ray Diffraction
VSM: Magnetic Sample Magnetometry

TABLE OF CONTENTS

LIST OF FIGURES

LIST OF TABLES

CHAPTER 1

INTRODUCTION

1.1 Photodynamic Therapy

For more than 25 years, photodynamic therapy (PDT) has been recognized as a non-invasive therapeutic procedure in malignant cancer treatment, it is now starting to be implemented clinically.[1] Compared to existing treatments including chemotherapy, radiation therapy and surgery, PDT is an efficient and selective technique of destroying only diseased tissues without harming healthy tissues.[2] In addition to oncological applications, PDT is a promising tool for a diversity of cardiovascular, dermatogical, and ophthalmic diseases.[3] In PDT, a photosensitizer (PS) which is defined as non-toxic drug or dye is administered systemically, locally, or topically.[4, 5] After an incubation period, it accumulates in the malignant tissue selectively **(Fig. 1)**. Then, a tumor locus is illuminated with a light of appropriate wavelength which results in activation of PSs. In the presence of oxygen, these activated PSs lead to the generation of cytotoxic species and highly toxic singlet oxygen ($^1O_2$) and finally to cell death and tissue damage.[6, 7]

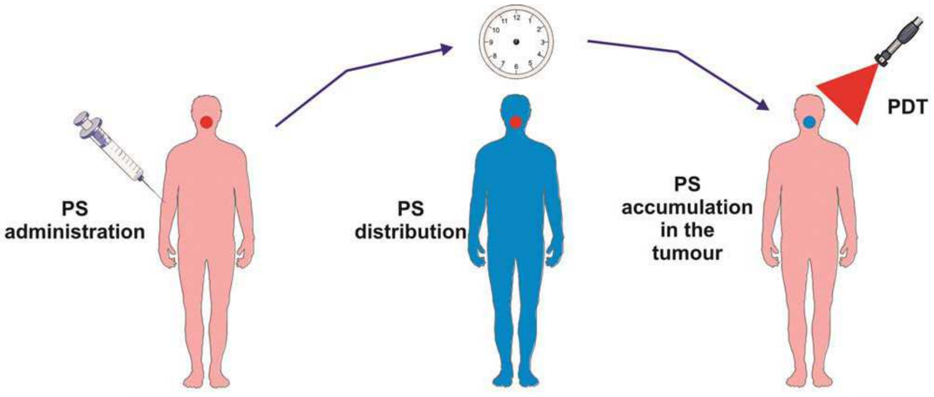

Figure 1: *The Principles of Photodynamic Therapy (PDT).*[8] *Copyright © 2011 American Cancer Society. Adapted with permission.*

1.2 Elements that Play a Significant Role in Photodynamic Therapy

Three main elements are required to produce singlet oxygen for PDT, namely; a photosensitizer, appropriate wavelength of light, and oxygen.[9] If one of these components lacks, the technique cannot be succeeded to treat malignant tumors. In addition, understanding photochemistry & photophysics of PDT and subcellular localization of PSs is essential in order to make rational selection from various types of PSs and light sources available and design novel photosensitizers.[10]

1.2.1 Photophysics and Photochemistry of PDT

Fig. 2 graphically demonstrates the mechanism of light absorption and energy transfer that are at the core of PDT. The ground state PS possesses two electrons with opposite spins located in the low energy molecular orbital. Since two electrons have opposite spins in a molecular orbital, this is known as singlet state. When PS at singlet ground state is irradiated with light, the absorption of light (photons) gives rise to a removal of one electron to a higher energy orbital with keeping its spin (first excited singlet state). The resulting excited PS is short lived (nanoseconds) species, and due to its instability it can lose its energy by fluorescence (by emitting light) or heat. Instead, excited PS may consume its excess energy by intersystem crossing in order to create more stable (long-lived (microseconds)) excited triplet state specie that has electrons which spin in a parallel conformation.[10,11]

The PS in triplet excited state can loss its energy by various ways (**Fig. 2**). One of them is spin forbidden transfer of electron at excited triplet state to singlet state directly. This is known as emission of light (phosphorescence).[9]

In addition to phosphorescence process, the PS excited triplet can undergo two kinds of reactions to form cytotoxic species: Type I and Type II processes.[10] Both Type I and Type II processes can take place at the same time, and the ratio between these reactions depend on the sort of PS used, as well as the concentrations of substrate which takes place in type I reaction and oxygen.[12,13]

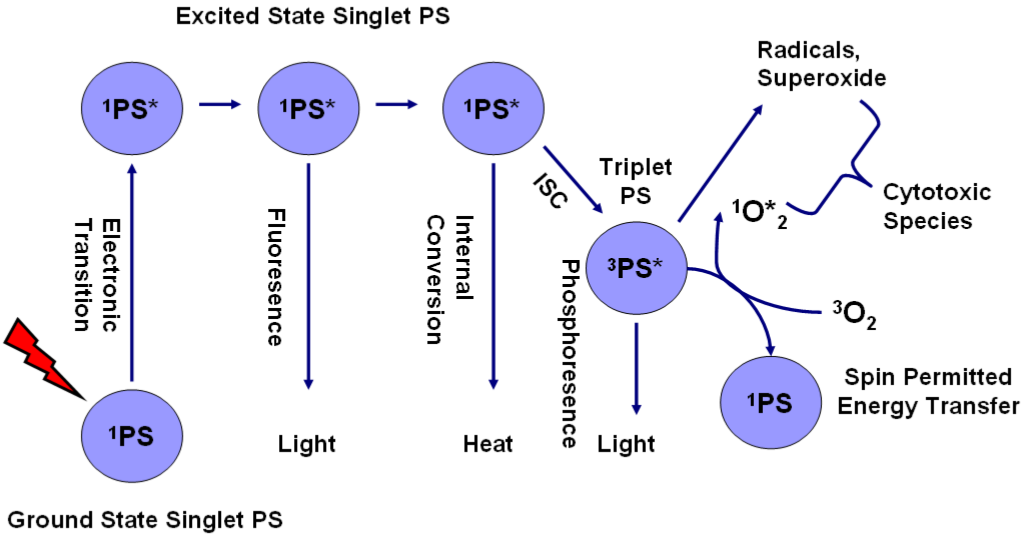

Figure 2: *Schematic representation of the photophysical and photochemical mechanisms of PDT*

In Type I reaction, PS at triplet excited state reacts directly with a substrate such as an organic molecule in a cellular microenvironment or cell membrane and transport a proton or an electron to create a radical anion or cation, respectively. Reactive oxygen species (ROS) may be formed as a result of further reactions between these radicals and oxygen.[12]

Firstly, a superoxide anion radical ($O_2^{\cdot -}$) is formed due to electron transfer from the triplet PS to molecular oxygen.[14,15] Superoxide itself is not biologically reactive and does not lead to oxidative damage. It can undergo reaction with itself (known as dismutation reaction) to create hydrogen peroxide (H_2O_2) and oxygen which is catalyzed by superoxide dismutase (SOD) enzyme. Hydrogen peroxide which have biological importance in terms of maintainability of enzyme functionality in cells undergo one-electron reduction to form a strong and literally indiscriminate oxidant hydroxyl radical (HO•). In the process of hydroxy radical formation, superoxide donates one electron to reduce metal ions in cell medium. Then, these reduced metal ions catalyze the cleavage of the oxygen-oxygen bond of hydrogen peroxide to generate a hydroxyl radical (HO•) and a hydroxide ion (HO^-). In addition, singlet oxygen can be generated due to the reaction between the hydroxyl radical (HO•) and superoxide.[16,17]

This powerful oxidizing agent (HO•) radical can easily react with any organic molecule in cellular environment. The resulting substrates are again a radical, and can react with other molecules in chain reactions. Generation of these ROS due to chain reactions is responsible for the damage to various cell membranes including mitochondria, lysosomal and nuclear membranes.[10,12]

In Type II reaction, PS at excited triplet state transfer its energy to molecular oxygen ($^3O_2$) in order to form excited state singlet oxygen ($^1O_2$) which shows high cytotoxicity. Formation of ROS via Type II process is mechanistically easier than via Type I process. Therefore, most PSs are considered to operate via Type II process.[16,8]

1.2.2 Photosensitizers

One of the most critical factors in PDT is the photosensitizer, which must be positioned at the site of tumor loci, absorb suitable wavelength of light and generate biological response.[18] A great number of photosensitizers have been tested in vitro and in vivo in PDT experiments, but very small number of them has shown ideal properties. As a result, latest studies have focused on the improvement and efficiency of novel photosensitizers.

The ideal photosensitizer should meet some necessities[18,19] (1) be chemically pure with invariable composition and a steady shelf life, (2) be ideally water soluble or soluble in a risk-free aqueous solvent mixture, (3) not aggregate improperly in biological environments which decrease photochemical efficacy, (4) have low level of dark toxicity and low occurrence of administrative toxicity (i.e. allergic reactions or hypotension), (5) absorb light with high absorption coefficients (>20,000-30,000M^{-1} cm^{-1}) in order to reduce the dose of PSs needed to attain the desired effect, (6) absorb light in the red or far-red wavelengths (600-800 nm), (7) be easily and cheaply synthesized and modified to make large scale production possible, (8) have short time period between injection and maximum accumulation at tumor loci and should be eliminated from the patient rapidly in order to avoid side effects of light exposure, (9) have a high quantum yield for singlet oxygen or super oxide generation.[20] The reason why absorption wavelength of photosensitizers is needed to be between 600 – 800 nm is that at shorter wavelengths, tissue penetration of light is very small and skin photosensitivity is high (the power in sunlight is elevated at $\lambda < 600$ nm). In addition, at high wavelengths (> 800 nm) the photons have not sufficient energy to produce singlet oxygen since energy at PS triplet state cannot be transferred to the gound state oxygen molecule to stimulate it to the singlet state[21]. Through the use of optical fibers of appropriate wavelength, PSs at tumor sites can be illuminated externally or internally (endoscopically).[18]

In addition, photosensitizers possessing heavy atoms (i.e. bromine, iodine) in their structures were proved to generate singlet oxygen more effectively when compared to the ones without heavy atoms. O’Shea et al. studied this phenomenon in BODIPY dyes and observed that presence of two bromine atom in molecule increases the effectiveness of singlet oxygen generation up to thousand folds. This observation is a result of increase in intersystem crossing due to heavy atom effect.[22] ISC is spin-forbidden process since electrons transfer from a singlet to a triplet excited state within a molecule and this process happens ineffectively for many compounds. Increase in spin-orbit coupling is required to make transition between states of different spin multiplicities much easier.

Spin-orbit Hamiltonian term is relative to fourth power of Z. Thus, existence of heavy atom enhances spin-orbit perturbation and spin forbidden singlet-triplet radiationless transition (ISC). Spin- orbit Hamiltonian formulation for hydrogen-like atom is shown below.[23,,24]

$$H_{SO} = \frac{e^2 . Z^4}{2a_0 m^2 c^2 n^3} L.S \qquad (1)$$

Where a_o is Bohr's radius, m is mass of electron, c is speed of light, n is principle quantum number, e is electron charge, Z is atomic number, L is angular momentum operator and S is spin operator.

1.2.3 Light Delivery & Light Sources

In order to achieve effective PDT action in vivo, adequate light should reach all the diseased tissue. In PDT, predicting spatial/temporal distribution of light through the tissue is prominent. When light enters the tissue, it is either absorbed or scattered and the degree of both routes depends on the wavelength of light and tissue type. Scattering is the most significant element restricting light penetration.[10]

Scattering is mainly due to turbidity of tissue since there are lots of inhomogenities such as cell organelles, macromolecules, organized cell structures etc. This turbid environment led to multiple scattering of light which in turn cause spreading of a light beam and loss of directionality. Absorption is mainly because of important tissue chromophores such as myoglobin, hemoglobin and cytochromes.[11] These factors are minimal between 600 and 1200 nm which is called 'optical window of tissue'. Therefore, red and infrared light penetrate more deeply through tissue, whereas blue light penetrates less effectively (**Fig. 3**). On the other hand, light up to approximately 800 nm can produce singlet oxygen ($^1O_2$) since energy of longer wavelengths is not enough to trigger photodynamic action. For PDT action, the typical efficient penetration depth is about 1—3 mm at near approximately 600 nm (intensity is reduced by 37 %), while penetration is approximately twice that at 700-850 nm. Thus, synthesis of novel PSs absorbing at longer wavelengths is prominent.[25,26]

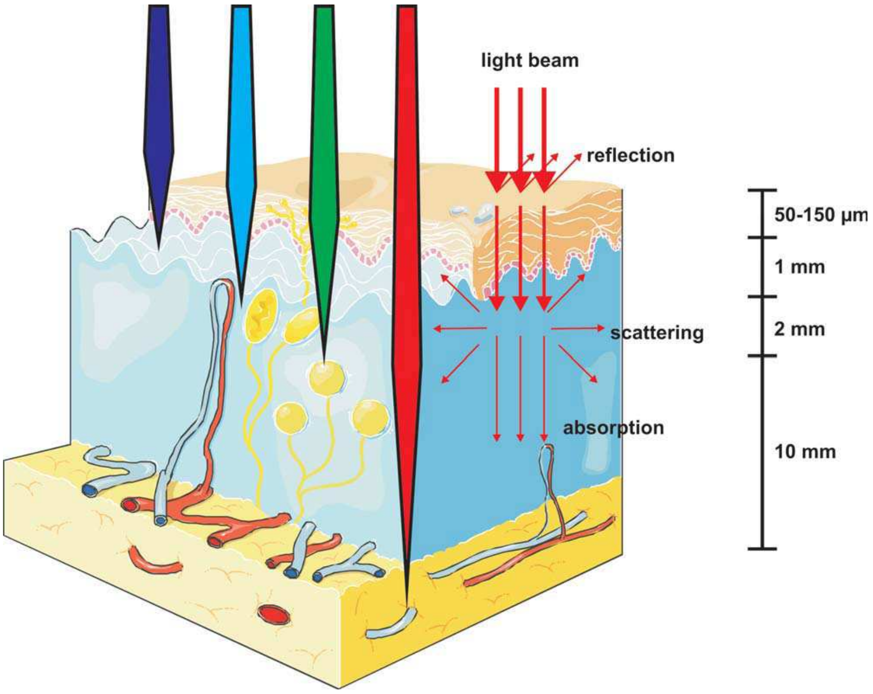

Figure 3: *Light penetration through the tissues.*[8] *Copyright © 2011 American Cancer Society. Adapted with permission.*

PS should be illuminated such a light source that it should display appropriate spectral characteristics that overlap with the maximum absorption wavelength range of the PS. In addition, light source should be selected with respect to disease characteristic (size of lesions, accessibility, and location) and cost.[17,27]

Light-emitting diodes (LEDs), lasers, and incandescent light sources have been implemented for PDT. Incandescent light sources and lasers display comparable efficiencies. However, lasers offer the precise selection of wavelengths and the specific application of light when compared to conventional incandescent lamps.

Among type of lasers, semiconductor diode lasers are generally preferred due to minimal cost, easier installation, calibration features and extended operational life. In addition, the introduction of lasers attached into fibers reformed PDT by allowing the endoscopic delivery of light to nearly every locus deep in the body under image guidance.[28,29,30]

1.2.4 Pathways of PDT Triggered Cell Damage

Within few minutes after irradiation, plasma membrane damage can be detected as result of PDT action. Since sensitizers do not have tendency to cover in cell nuclei, DNA damage, carcinogenesis, and mutations are rarely expected pathways[31]. The plasma membrane damage can be noticed as flaking of vesicles containing lysosomal and cytosolic enyzmes, swelling, blebbing, plasma membrane depolarization, active transport decrease, retardation of plasma membrane enzyme (Na^+ K^+ – ATPase) activity, regulation of surface antigens, a increase in Ca^{2+}, etc.[32]

Three different mechanisms have been accepted for contribution of tumor destruction due to PDT action (**Fig. 4**).[33] Firstly, cytotoxicity due to ROS can cause the death of tumor cells directly by apoptosis and/or necrosis.[6,11,34] Secondly, PDT is believed to eradicate diseased tissue by the shutdown of tissue vasculature which leads to lack of nutrients and oxygen at the tumor loci.[35] Thirdly, discharge of stress response proteins & cytokines and inflammation induced by PDT in tumor loci can cause invasion of leukocytes.[36,37] This phenomenon can both cause tumor destruction and the immune system stimulation which in turn lead to recognition and destruction tumor cells even at remote locations. These three mechanisms can affect each other. It is still unclear that which of these three mechanisms have significant effect on overall tumor damage, therefore; further research is needed.[33]

In apoptosis, cells are usually fragments into membrane enclosed vesicles called apoptotic bodies. These apoptotic bodies are then phagocytized by the neighboring cells without involving inflammation and cells die in an immunologically programmed way. During later stages of apoptosis, structural integrity of organelles and plasma membrane are still preserved. Functionality of the mitochondria and lysosomes are also active for quite a long period. Transcriptional activation of specific genes counting the activation of endonucleases, DNA degradation into oligonucleosomal fragments, and consequently activation of caspases is the significant events of apoptosis.[35,38]

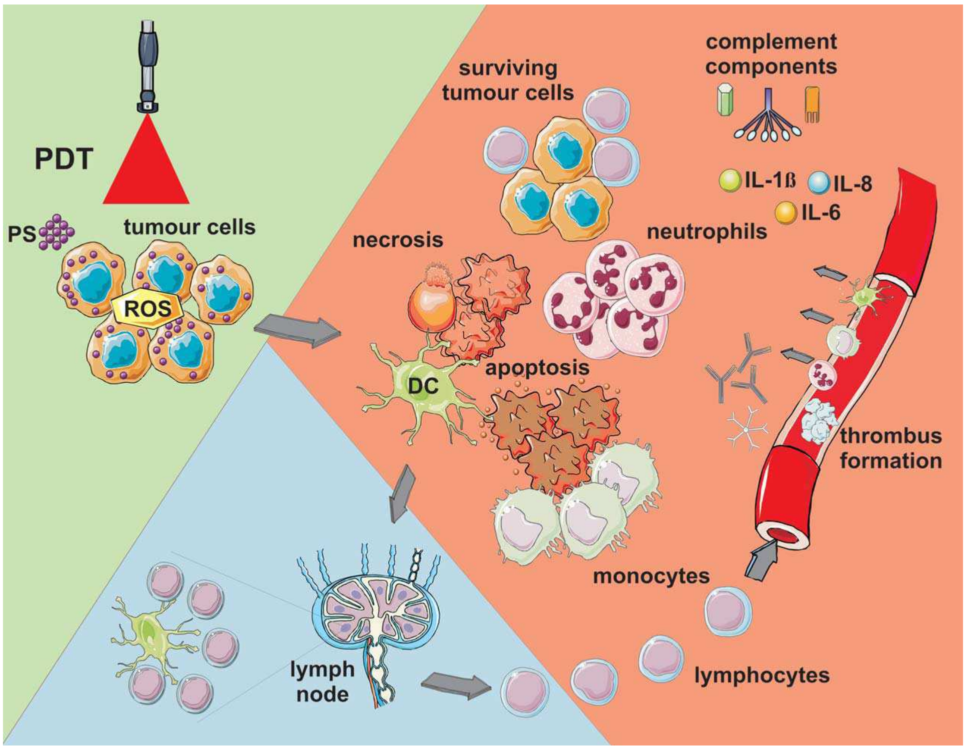

Figure 4: *Pathways of PDT triggered cell damage. ROS lead apoptotic and necrotic cell death. Damage to microvasculature (not shown) is another reason of tumor destruction. PDT also triggers immune response noticed by inflammatory cells, such as lymphocytes, plasma cells, and macrophages.*[8] *Copyright © 2011 American Cancer Society. Adapted with permission.*

Necrosis is unprogrammed cell death pathway due to physical or chemical damage and considered as an accidental cell death. Unlike apoptosis, in the early stages of necrosis, cells begin to swell and it is followed by distruption of organelles and plasma membrane followed by release of the cytoplasmic content. In constrast to apoptosis, necrosis induces inflammatory response in the tissue.[39]

1.2.5 Localization of Photosensitizers in Subcellular Level

For efficient PDT action, uptake of photosensitizers by tumor cells is crucial because ROS are short lived species and affect specifically the site of generation. Once PS enters into cells, it can localize within many cellular organelles such as mitochondria, lysosomes, plasma membrane, and endoplasmic reticulum.[36] Efficiency of accumulation at tumor loci and specificity of localization are mainly based on three factors. One of them is hydrophilic or lipophilic character of PS which is articulated as the logarithm of the octanol/water partition coefficient. Since PSs especially accumulate in the lipophilic organells of tumor cells, it is observed that lipophilic PSs preferentially gather at tumor loci. In additon, since these PSs can enter cells by passing lipophilic cell membrane, it is important to design drug delivery systems such as micelles, liposomes, polymeric nano and micro particles etc.[10]

Generally, hydrophilic sensitizers kill tumor cells indirectly by giving harm to blood vessels and disrupt the supply of nutrients and oxygen. Hydrophobic drugs attack hyperproliferating cells with direct interactions.[31]

Second factor is the degree of asymmetry in the sensitizers and the third one is net charge which can be between -4 and +4. Hydrophobic PSs possessing two or less negative charges ($\geq$-2) can enter the cells and localize cellular compartments. On the other hand, less hydrophobic PSs having more than two negative charges (<-2) are too polar to pass through cell membrane. Therefore, they are taken by endocytosis. It should be keep in mind that other elements such as lower pH at tumor loci can also be related to effective accumulation and uptake of PSs. Due to lack of oxygen and high glycolytic activity, low pH value is generally assigned for tumor locus. Because albumin and other serum proteins carry drugs, it is revealed that there is accumulation of PSs within the vascular loci of tumor sites and the interstitial space.[40,41,42]

1.3 Photosensitizers in Literature

The majority of PSs implemented both experimentally and clinically has a heterocyclic ring structure similar to that of heme in hemoglobin or chlorophyll. In 1980s and 1990s, lots of PSs were designed and synthesized. It is still in progess that new ones are introduced regularly[43].

According to their origin and chemical structures, PSs can be classified into three main broad categories: (i) PSs based on porphyrin platform (e.g., Photofrin, BPD-MA, ALA/PpIX), (ii) PSs based on chlorophyll platform (e.g., chlorins, bacteriochlorins, and purpurins), and (iii) dyes (e.g., napthalocyanine, phtalocyanine, and BODIPY) PSs which are mainly composed of the porphyrins introduced in the 1970s and early 1980s are named first generation PSs (*e.g.,* Photofrin). After the late 1980s, porphyrin derivatives or other PSs synthesized are called second generation PSs (*e.g.,* ALA). Third generation PSs usually refer to the alterations such as biologic conjugates (*e.g.,* antibody or liposome conjugate). Although these terms are still being used, they are not acknowledged unanimously.[43,44]

Table 1: Photosensitizer Categories

Porphyrin platform
HpD (hematoporphyrin derivative)
HpD-based
BPD (benzoporphyrin derivative)
ALA (5-aminolevulinic acid)
Texaphyrins
Chlorophyll platform
Chlorins
Purpurins
Bacteriochlorins
Dyes
Phtalocyanine
Napthalocyanine

Natural porphyrins are entirely conjugated tetrapyrroles and differ in the number and sort of side groups mostly carboxylic acid groups. The main disadvantages of Photofrin (clinically approved) and other porphyrin-based PSs are that they have weak absorbance in the red region of the spectrum (therapeutic window region) and trigger long-term skin photosensitivity (4-6 weeks).[10]

Another group is based on chlorophyll platform. Chlorin core is obtained by reduction of one pyrrole ring on the porphyrin periphery, and when one of pyrole on chlorin periphery is further reduced, it gives bacteriochlorin. Both of these classes absorp light at longer wavelengths (λ_{max}: 730-800 nm for bacteriochlorins and 650-670 nm for chlorins) and they are effective singlet oxygen generators. Bacteriochlorins are seemed to be more efficient PSs than chlorins, however; there are some questions about their stability upon storage. Numerous bacteriochlorin and chlorin derivatives are in different stage of assessment for PDT.[10,45]

In the dye family, phthalocyanines, naphthocyanines, and their relatives are mostly used in clinical trials. They have absorption band 650—850 nm range and most of them are hydrophobic necessitating delivery systems for clinical implementation like liposomes. Attaching these dyes to a diversity of metals seems to improve efficiency. Due to existence of four phenyl groups in the structure, solubility and aggregation problems are raised. Therefore, PCs are commonly modified with sulfonic acid groups to give water solubility.[10]

BODIPY dyes (borondipyrromethene) have also rising potency for PDT due to their high photostabilities and high extinction coeffients. Since multiple chemical modifications can be done straightforwardly on these molecules, attachment of moieties that would allow selective targeting, water solubility is possible. Moreover, chemical groups that enhance the PDT action can be easily attached to BODIPY dyes.[46,47] Synthetic conjugated pyrrolic ring systems including such structures as sapphyrins,[48] texaphyrins,[18] and porphycenes[49] are also broad class of potential PSs. Hypericin comes from this class. Another broad class is composed of non-tetrapyrrole derived natural or synthetic dyes such as toluidine blue O and Rose Bengal.[10]

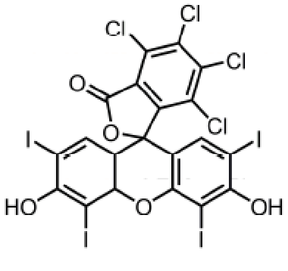

Rose Bengal

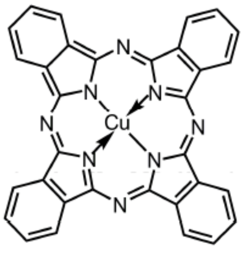

Phthalocyanine

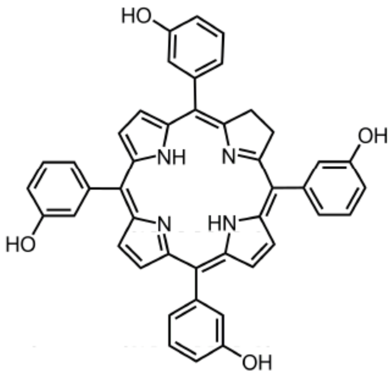

Chlorin Dyes

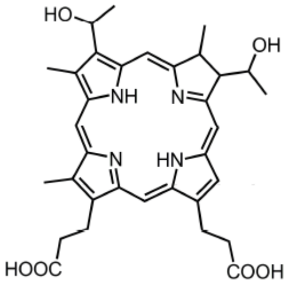

Hematoporphyrin

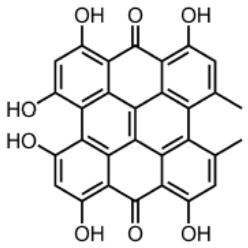

Hypericin

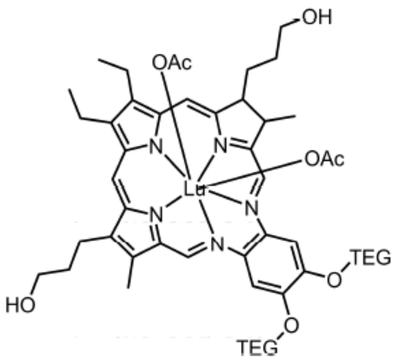

Texaphyrin

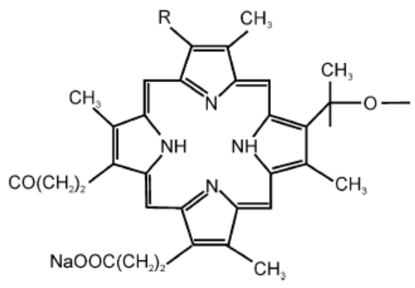

Photofrin

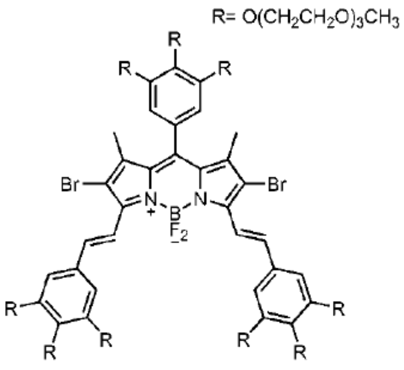

BODIPY- based photosensitizer

Figure 5: *Structures of Some Photosensitizers in Literature.*

1.4 Clinical Applications of PDT

Numerous products can act as PS and new ones are frequently introduced. However, few of them have been implemented into clinical studies and even fewer commercially exist. **Table 2** demonstrates currently available PSs.[19]

Table 2: Photosensitizers on the Market

Platform	Drug	Substance	Manufacturer
Porphyrin	Photofrin®	HpD	Axcan Pharma, Inc.
Porphyrin	Levulan®	ALA	DUSA Pharma, Inc.
Porphyrin	Metvix®	M-ALA	PhotoCure ASA
Porphyrin	Visudyne®	Vertiporfin	Novartis Pharmaceuticals
Texaphyrin	Antrin®	Lutexaphyrin	Pharmacyclics
Chlorin	Foscan®	Temoporfin	Biolitec Pharma Ltd.
Chlorin	LS11	Talaporfin	Light Science
Chlorin	Photochlor	HPPH	RPCl
Dye	Photosens®	Phthalocyanine	General Physics Institute

Clinical methods have been proposed for different cancer types over the past 30 years and there have been over 200 clinical studies now.[18] These are including cancers of the head and neck,[50] lung,[51] bladder,[52] gastrointestinal tract,[53] prostate,[54] actinic keratosis, and nonmelanoma skin cancers.[55] Most of the patients response positively to PDT and when compared to other treatment methods, reoccurrence is very low.[18]

For noncancerous diseases such as age-related macular degeneration, psoriasis, atherosclerosis, PDT is successfully employed.[56,57] In addition, it is also shown that PDT has effect against viral diseases like herpes.[58]

1.5 Developing Strategies in PDT

Different approaches towards PDT are currently investigated preclinically. These are based on different chemistry, photophysics, and photobiological mechanism.[8]

1.5.1 Nanotechnology in PDT

There are several approaches in nanotechnology to improve PDT efficacy. One of the significant advantages of nanoparticles is that they can be loaded with high concentration of PSs and modified with targeting groups such as peptides and antibodies. Or, photochemical and photophysical properties of PSs can be separate from activation and delivery process since NPs take the role of these processes.[59] Here are some examples from literature.

Liposomal nanoparticles can be implemented clinically in order to make hydrophobic PSs water soluble.[60] Biodegradable polymers, silica and metallic (gold, iron oxide) nanoparticles are commonly studied. Moreover, magnetic nanoparticles are also very useful since accumulation of NP based PSs at tumor loci can be enhanced by changing magnetic field.[61] By designing hybrid nanoparticles other therapeutic strategies like hyperthermia or imaging technique like MRI can be coupled together. Nanotechnology provides novel approaches to solve problem of need for red region absorbed PSs. When quantum dots are attached to a PSs, they absorp the light effectively and transfer this energy to PS. Upconverting particles are also one of the hot topics since they can absorp at red region of spectrum and transformed into shorter wavelength light that illuminates the linked PS[61]. Finally, one of the latest methods is the encapsulation of PS by polymeric NPs. Then, it is integrated into liposomes possessing a second antiangiogenic agent.[62]

1.5.2 PDT Molecular Beacons

PDT molecular beacons (MBs) are designed in such a way that they enable controlled production of singlet oxygen with a high tumor-to-nontumor specificity, therefore; damage to healthy tissues is minimized. In MBs, a quenching molecule is attached to PS, so that PS cannot generate singlet oxygen until the linker between quencher and PS is cleaved. In some designs, other unquenching methods are used instead of cleavage. There are many approaches to build MB using different type of quenchers, quenching mechanisms and cleavage mechanisms. One of the designs is based on the usage of linkers (e.g. peptide) which can be easily cleaved by target specific enyzmes that are overexpressed in tumor cells. Singlet oxygen production capability of photosensitizer is prevented because of the existence of quencher in close proximity to allow Förster resonance energy transfer (FRET). When peptide linker is cleaved with tumor selective enzyme by causing removal of quencher, FRET is blocked and PDT action become activated **(Fig. 6)**. Instead, oligonucleotide (hairpin) loop which is unfastened by hybridization to complementary mRNA can be utilized as a linker. When hairpin loop is opened, FRET will be prevented since quencher and PSs cannot become in close proximity.[63,64]

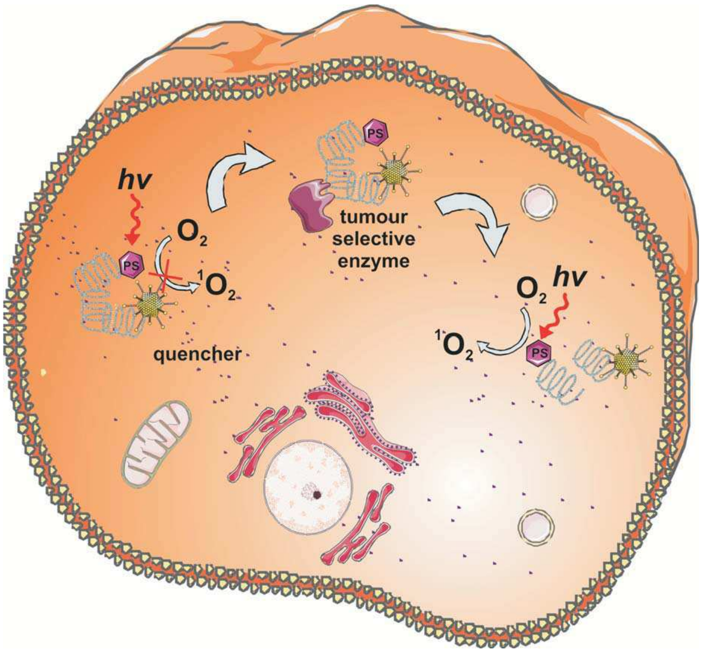

Figure 6: *Photodynamic Therapy Molecular Beacons Based on Peptide Linker.*[8] *Copyright © 2011 American Cancer Society. Adapted with permission.*

There are also other approaches to activate photosensitizers. One remarkable model of such PSs as BODIPY derivative was synthesized by Akkaya et al **(Fig. 7)**. [65] In this design, photosensitizer activation requires to use two different control parameters functioning as a logic controller. These parameters are two important physiological parameters for tumor cells; sodium and pH. In cancer cells, sodium concentration is higher and pH is lower when compared to healthy cells. Pyridine groups become protonated in acidic media and results a bathochromic shift in the absorbance spectrum and shifts to 660 nm. When PS is illuminated with 660 nm light, protonated molecules excited and show PDT action since photo-induced electron transfer (PET) is deactivated by Na^+ binding to crown ether moiety. Thus, this PS was proved to have 6 times higher singlet oxygen generation capacity at low pH and high sodium concentration when compared to the condition at higher pH and lower sodium concentration.

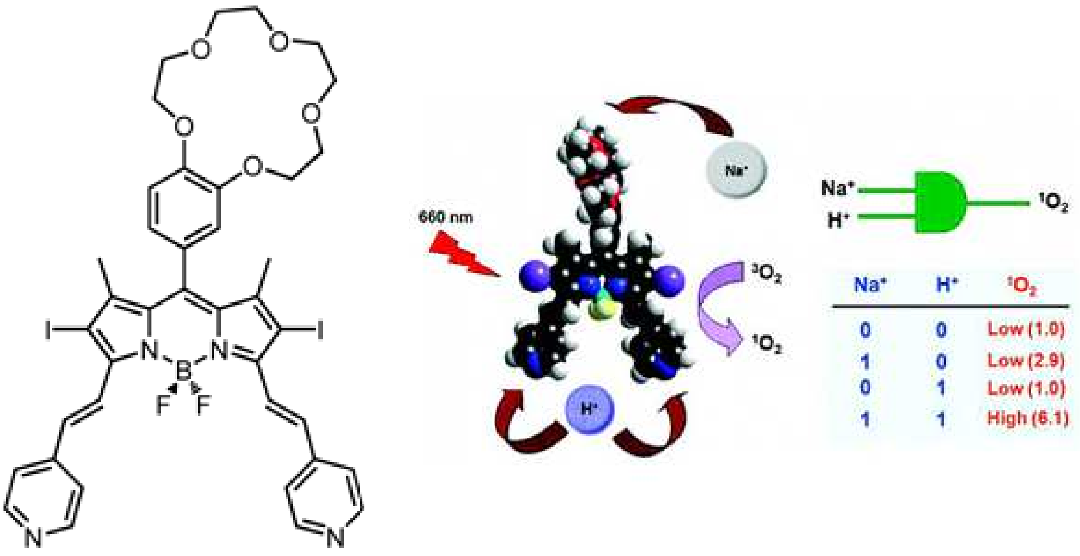

Figure 7: *Logic gate based activatable photosensitizer.*[65] *Copyright © 2009 American Chemical Society. Adapted with permission.*

1.5.3 Two-Photon PDT

The concept of 2-photon PDT depends on simultaneous absorption of two light photons upon irradiation with short (roughly 100 femtosecond) laser pulses having high peak power. After illumination, the succeeding photobiological and photochemical mechanisms are similar to that of one-photon PDT. The main advantage of two-photon PDT is that since each photon supplies only one-half of the excitation energy, longer wavelength (near-IR) light can be implemented. It is reported by Starkey et al that 2-cm depth is attained for effective treatment in tumor xenogafts. When the penetration depth compared to that of one-photon absorption, this depth is noticeably geater.[66,67]

1.5.4 Metronomic PDT

Both light and PS are used at very small dose rates over an extended time (hours–days) in metronomic PDT (mPDT). By mPDT, tumor cell-specific apoptosis is encouraged with nominal tissue necrosis. Up to now, primary motivation of mPDT is to reduce direct PDT damage to neighboring normal brain in glioma disease. In addition, it prevents from the damage caused by inflammatory reaction to PDT-triggered tumor necrosis.[8]

1.6 Future of Photodynamic Therapy in Oncology

Although PDT has been used in oncology more than 25 years, PDT is still considered to be a fresh and promising antitumor approach. Its full potential and range of applications have not been revealed yet. PDT has not become a mainstream in oncology yet due to several reasons; hospital and clinician opposition to a new technique, the obscurity in the introduction of the optimal variables for a treatment, need for low-cost and suitable light sources, and the principal cost of building a PDT centre. The most important reason should be that application of present combinations of light sources and drugs have not demonstrated apparent advantages over other alternatives (e.g. radiotherapy) in large randomized clinical studies. This condition is most likely due to the fact that most drugs (PSs) have not been optimal in terms of efficacy.[68]

Up to now, most PSs have been developed chemically rather than biologically, or clinically. Generally, focus has been given to improve optical properties of PSs, however; there are many problems of early PSs need to be solved. These are low selectivity, prolonged skin photosensitivity, and inconveniently lengthy drug-to-light gap. To overcome existing problems, modifications of PSs moieties through its physicochemical properties are needed. In addition, targeting must be improved by tailoring PSs with moieties such as peptide scaffolds, antibodies, or polymers. Therefore, improved drugs without prolonged skin photosensitivity and with more selectivity is needed. If such drugs can be implemented, the benefits of PDT in regards to patient and practitioner convenience, minimal invasion in the body, and health economics will guarantee a considerable future role for PDT in oncology. Moreover, since PDT has an interdisciplinary uniqueness, it inspires most specialists in chemistry, physics, biology, and medicine. Thus, novel improvements and applications can only be restricted by their enormous imagination.[7,8]

1.7 Biological Applications of Nanoparticles

Combination of biology and material science give rise to the utilization of nanomaterials in biotechnology. Nanoparticles (10-100 nm) are colloidal particles generally synthesized in either organic or aqueous phases.[69,70] Nanoparticles can straightforwardly flow through blood vessels and enter the target tumor cells.[71] Nanoparticles being a functional platform have great potency for broad range of therapeutic applications since there are various core materials existing with tunable surface properties.[72] Uniqueness of nanoparticles in terms of utility and properties come from many attributes. First, similar size of nanoparticles with macromolecules such as proteins and polynucleic acids provides an interaction of nanoparticles with these molecules, therefore; allows the application of biosensing. In addition, the size (<100 nm) of these particles enables conjugation with various molecular markers, which can interact at molecular and cellular levels. Thus, nanoparticles can be designed straightforwardly for targeting many diseases.[73] Moreover, nanoparticles can be tailored with a broad range of semiconductor and metal core materials possessing functional properties like magnetic behavior and fluorescence.[74] Moreover, the surface of these core materials can be modified with a variety of ligands with respect to purpose of their applications. **Table 3** shows the characteristics of some recognized core materials and related probable ligands utilized for surface modification with their applications.

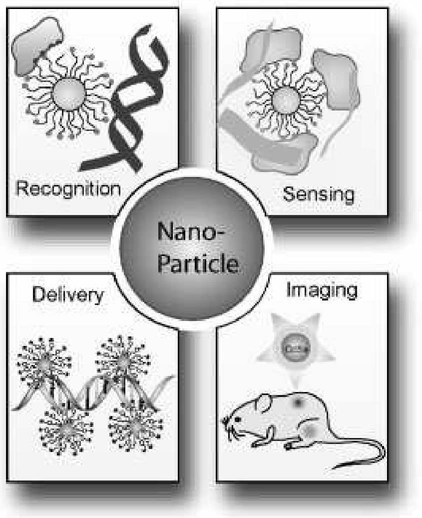

Figure 8: *Main Applications of Nanoparticles.*[75] *Copyright © 2008 WILEY-VCH Verlag GmbH & Co. KGaA, Weinheim. Adapted with permission.*

There are three main area of nanoparticle application in biology **(Fig. 8)**, namely; biosensing, bioimaging, drug and gene delivery.[75]

Table 3: Characteristics, ligands, and main applications for well-known core materials

Core material	Characteristics	Ligand(s)	Applications
Au	Optical absorption, fluorescence and fluorescence quenching, stability	Thiol, disulfide, phosphine, amine	Biomolecular recognition, delivery, sensing
Ag	Surface-enhanced fluorescence	Thiol	Sensing
Pt	Catalytic property	Thiol, phosphine, amine, isocyanide	Bio-catalyst, sensing
CdSe	Luminescence, photo-stability	Thiol, phosphine, pyridine	Imaging, sensing
Fe_2O_3	Magnetic property	Dopamine derivative Amine, Diol,	MR imaging biomolecule purification
SiO_2	Biocompatibility	Alkoxysilane	Biocompatible by surface coating

1.8 Theranostic Nanoparticles

Theranostic nanoparticles combine diagnostic and therapeutic abilities in one dose.[76] Nanotheranostic platforms have several advantages when compared to conventional delivery systems.[77] One of the most important benefits of these nanoplatforms is the capability of targeting to diseased loci, therefore; reduce systemic toxicity. In addition, labile or hydrophobic drugs can be solubilized by including them in the medium of the nanoparticle during the formulation, which in turn leads to enhanced pharmacokinetics. Moreover, nanotheranostic platforms have geat potency to treat, image and predict therapeutic response.[77]

One of the unique properties of theranostic nanoplatforms based systems is multifunctionality. These nanoparticles can be designed such a way that can hold various components (Fig. 9). These consist of (i) therapeutic agents, (ii) imaging agents, (iii) targeting agents such as peptides, antibodies, aptamers, lectins, proteins, and protein fragments,[78] (iv) hiding agents that circumvent intrusion with the immune system.[79-87]

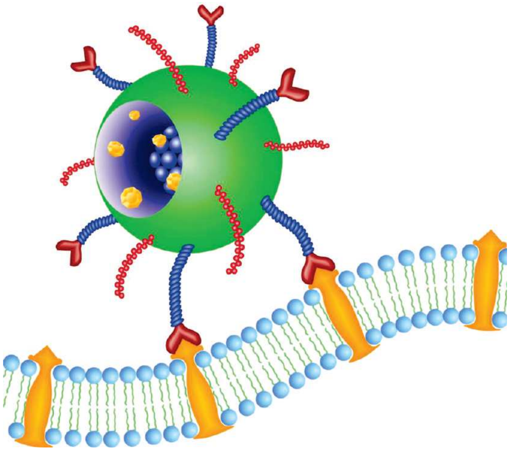

Figure 9: *Representative Theranostic Nanoparticle. Ligands on the surface of multifunctional nanoparticles target to specific surface receptor of tumor cells. Blue and yellow spheres within a core represent imaging and therapeutic agent, respectively.*[77] *Copyright © 2010, American Chemical Society. Adapted with permission.*

In fact, targeting to tumor loci can also be achieved without attachment of targeting ligands. Accumulation at tumor loci can occur through passive targeting besides active targeting. Passive targeting based on enhanced retention and permeation effect in tumor loci in which nanoparticles escape from leaky vasculature of tumor and gather nonspecifically in the diseased loci. Shape, size, and charge of NPs determine the effectiveness of passive targeting. NPs which have the following properties removed from circulation by the liver fast (<15 min) before gathering at lesion: (1) having zeta potential between -20 mV and +20 mV, (2) being larger than 100 nm, (3) possessing solid cores.[88]

Theranostic nanoparticles provide effective method for detection of tumor (imaging), treatment and follow-up screening of tumor response (**Fig.10)**.[89] Chemotherapy, nucleic acid and gene delivery, hyperthermia (photothermal ablation), radiation and photodynamic therapy are therapeutic strategies that can be coupled with one or more imaging modes for both in *vivo* and in *vitro* studies.

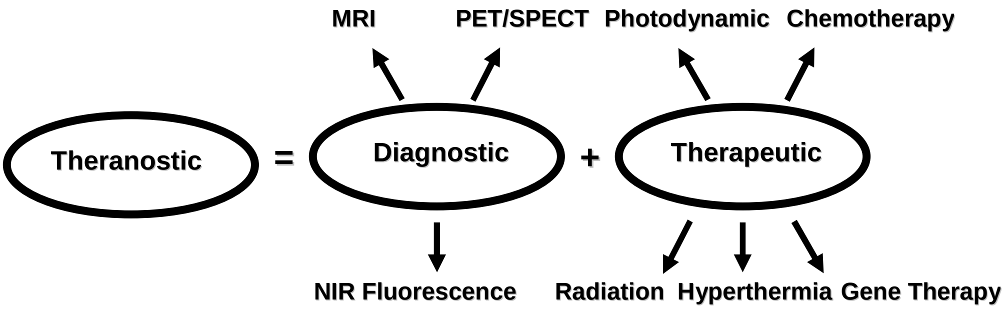

Figure 10: *Theranostic Nanoparticles can be decorated with various diagnostic and therapeutic modalities. MRI (magnetic resonance imaging), PET (positron emission tomography), SPECT (single photon emission computed tomography).*

Imaging probes, such as fluorescent labeling agents (e.g. organic fluorescent dyes, quantum dots), MRI contrast agents, and nuclear imaging agents (SPECT/ PET agents) can be incorporated onto either or therapeutic delivery vehicles or therapeutic agents.[76] Imaging techniques depend on fluorescent labeling agents can provide monitoring at a cellular level with high-resolution images defining organelles inside the cell. Other techniques such as MRI, PET or SPECT are generally preferred for in vivo studies, since they are lack of the problems of photobleaching and background fluorescence.[76]

1.9 Magnetic Nanoparticles as Magnetic Resonance Imaging (MRI) Probes

Metals such as iron, cobalt, and nickel or metal oxides are magnetic materials which can be found in wide range of devices such as hard disks, motors, generators, sensors, videotapes etc. Thus, there is an increasing interest to minimize these magnetic materials. However, very miniature scale magnetic materials typically 10-20 nm range display different properties from the bulk material. One of the most important differences is that magnetic nanoparticles which are smaller than single domain limit (10-20 nm) shows superparamagnetism at room temperature. In other words, above its Curie temperature, ferrimagnetic or ferromagnetic materials typically experience a transition to a paramagnetic state. However, when the size of MNPs becomes smaller in nm scale, NPs undergo unusual transition to superparamagnetism below Curie temperature. Superparamagnetism depends on the size of the MNP.[90,91,92]

The route of magnetism depends on the spin motions and the orbitals of electrons. Spin and angular momentum of electrons are related with a magnetic moment.[92] Magnetic order is caused by the the interaction among the magnetic moments of atoms in the below a certain temperature.[93] Magnetic domains are region of bulk magnetic materials in which there is an alignment of magnetic moments. When the size of material is minimized, every MNPs become one single domain and magnetic properties are changed.[94]

Since every MNPs are single domain, thermal energy is enough to alter magnetization spontaneously within each MNP and this cause superparamagnetism phenomena. The reason of this phenomena is free random rotation of magnetic moments of each particle (in correlation with orientation of MNPs) under the influence of temperature **(Fig.11)**. Therefore, the net magnetic moment of the MNPs is zero at sufficient temperature in the nonexistence of an electromagnetic field. On the other hand, there will be a net statistical arrangement of magnetic moments in the existence of a field causing large constant magnetic moment. This concept is analogous to that of paramagnetic materials, but this case all MNPs behave like a huge paramagnetic atom. MNPs containing many atoms respond fast to applied magnetic field with negligible residual magnetism and coercivity. Coercivity is the field necessary to convey to magnetization to zero. Since the probability of agglomeration is small at room temperature, superparamagnetic nanoparticles can be implemented for various biomedical applications.[90,94] Susceptibility (w) and coercivity (Hc) of MNPs which are main factors effecting magnetic properties is determined by the shape and size of MNPs, crystallogaphic structure, vacancies & defects, composition, and magnetic anisotropy.[95]

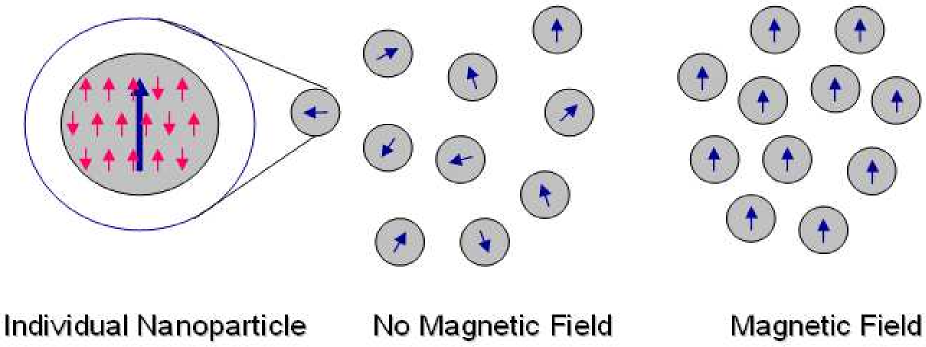

Figure 11: *Aligment of Magnetic Moments of MNPs in the Absence and in the Presence of Magnetic Field.*

Upon storage on longer periods, it is usual that MNPs tend to aggregate since they want to minimize energy related to the high surface area. In addition, bare nanoparticles are chemically instable because they can simply oxidized in air which leads to loss of dispersibility and magnetism. To prevent these kinds of situations, coating of MNPs plays a critical role. Coatings can be done with inorganic layer such as carbon, silica; organic layer such as polymers or surfactants. In addition, by the usage of these layers further modifications like attachment of various ligands or other nanoparticles is possible.[90] However, coating of MNPs can lead to decrease in the saturation magnetization.[96]

1.9.1 Basic Principles of MRI Contrast Improvement

When magnetic field is applied, magnetic dipole moment of MNPs is induced causing to creation of local magnetic fields. This causes the decrease of relaxation times (T1 and T2) of water molecules which diffuse into the edge of induced dipole moment. This is called proton relaxation and enhancement effect and cause the adjustment of the Nuclear Magnetic Resonance (NMR) signal intensity which results in the darkening in T2- weighted MRI images **(Fig. 12)**.[97,98]

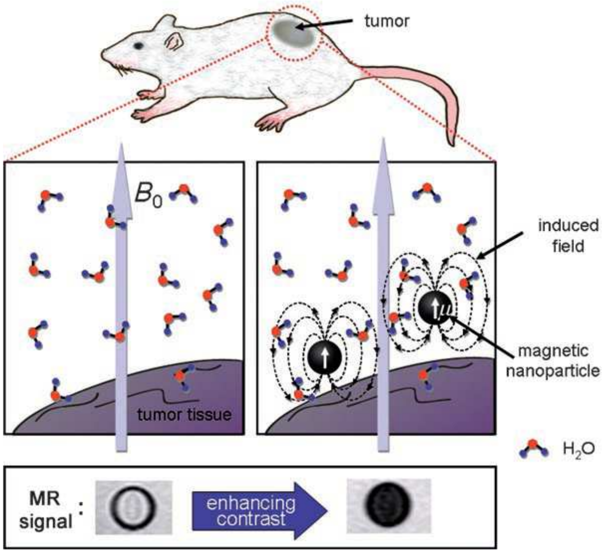

Figure 12: *Proton Relaxation and Enhancement Effect of MNPs in MRI.*[97] *Copyright © 2008 WILEY-VCH Verlag GmbH & Co. KGaA, Weinheim. Adapted with permission.*

Spin–spin relaxivity R2 (R2=1/T2) represents the level of T2 contrast effect. Higher the value of R2 leads to greater contrast impact. T1 and T2 represent the longitudinal and transverse proton relaxation times, respectively. T1 is related to reorganization of the nuclear spin population to attain the thermal equilibrium distribution. T1 evaluates dipolar coupling of the proton moments to neighboring. T2 is associated to the 'decoherence' of magnetization of the protons that have magnetic interactions with each other and with other inconsistent moments in neighboring.[98,99]

1.9.2 Superparamagnetic Iron Oxide Nanoparticles

Generally, larger magnetic moments are preferred for most application since it minimizes the amount of MNPs necessary. On the other hand, biocompatibility has great importance for biological applications. Thus, a balance between necessity of biocompatibility and larger magnetic moments should be reached. Therefore, iron oxide superparamagnetic particles (SPIONs) are often preferred to other superparamagnetic metals which are more toxic.[98,100] Up to now, SPIONs have been used in humans for MRI diagnosis. However, in a near future they are expected to be utilized for therapeutic applications.[101]

Magnetite (Fe_3O_4), maghemite (γ-Fe_2O_3), and haematite (α-Fe_2O_3) are types of SPIONs. Magnetite is promising in terms of biocompatibility among them.[102]

SPIONs need to possess several properties in order to guarantee the effectiveness as MRI contrast agent. The method chosen to synthesize SPIONs affects all properties of SPIONs.[103] SPIONs should be uniform in size since it has impact on the biodistribution and biocompatibility in *vivo.* NPs greater than 50nm in diameter are removed by reticulo-endothelial system (RES).[104,105] Low toxicity and high colloidal stability of SPIONs are important since they bring SPIONs at the stage of clinical applications.[103] They also can be attached to a range of enzymes, drugs, proteins, antibodies etc. for biomedical uses. Saturation magnetization (electromagnetic unit/gram, [emu/g]) values are a measure of the magnetic moment, therefore; stronger MRI signals are obtained at higher values of saturation magnetization.[103,104,105] Magnetization values for SPIONS are typically between 30-50 emu/g.[105,106] The highest magnetization value occurs typically in the 6-20 nm particle size range.

1.9.2.1 Chemical Routes for the Synthesis of SPIONS

Since SPIONs have crystalline structures, synthesis involves two processes, nucleation and growth. Solution should be saturated for precipitation to take place since any excess solute added cause the formation of nanocrystals.[107] The solution should be supersaturated for nucleation to occur which leads to a short single burst of nucleation. The concentration decrease and nucleation end after the short burst in nucleation. Then, solutes from solution diffuse onto the nuclear surfaces till equilibrium concentration is attained. This stage refers to growth of nanoparticles.[108,103] Monodisperse SPIONs can be obtained if nucleation and growth progress separately. This can be achieved by either the end of nucleation or before critical supersaturation.[104]

There are several routes for the synthesis of SPIONs for applications to MRI.[104] Method of chemical precipitation, high temperature reaction, and constrained environments reactions are significant ones.[73]

The chemical precipitation method is the easiest pathway to obtain SPIONs.[107] Either maghemite or magnetite can be obtained by coprecipitation of stoichiometric combination of ferric and ferrous salts in an aqueous media. The pH should be between 8 and 14, and ratio of 2:1 for Fe^{2+}/ Fe^{3+} should be attained. The precipitated magnetite is black and the overall reaction can be written as:[104]

$$Fe^{2+} + 2Fe^{3+} + 8OH^{-} \rightarrow Fe_3O_4 + 4H_2O \qquad \textbf{(2)}$$

The reaction should be carried under nitrogen to prevent oxidation of magnetite to maghemite.[104]

In high temperature method, iron complexes are decomposed in the presence of surfactants and organic solvents at high temperatures. SPIONs with high monodispersity and high crystallinity can be obtained. The resulting SPIONs are highly dispersible in organic solvents rather than aqueous medium.[109] Sun and Zeng produce SPIONs in size of 4 nm by decomposition of iron (III) acetylacetonate upon heating to 265°C in phenyl ether, alcohol, oleic acid, and oleylamine.[110]

In the method of constrained environments, formation of SPIONs progress inside the lipid-based structures with dendrimers or amphiphiles. In other words, iron oxide core is stabilized by these surfactants, which restrict particle nucleation and growth process. Liposomes, micelles, microemulsions, lipid based NPs are amphiphilic molecules that can be used for this purpose. These amphiphilic molecules gather into aggregates in an aqueous solution spontaneously which results various size and geometries such as spherical, cylindrical, and bilayered of SPIONs.[111,112]

1.9.2.2 Silica Monolayer for Superparamagnetic Iron Oxide Nanoparticles

SPIONs should be stabilized to prevent oxidation and aggregation. There are numerous ways of attaining stability and solubility. These methods can be coating with inorganic layers such as silica, carboxylates such as citrid acid, and polymers such as dextran and PEG.[73] Here, silica monolayer will be discussed.

Silica is an inert and biocompatible molecule that coats the surface of SPIONs. Layer of silica reduce aggregation and improve stability. Reduction in aggregation results from sheltering of the magnetic dipole interaction by the silica shell. Since silica has negative charge on it, it makes SPIONs stable in aqueous medium.[113,114]

There are two common methods for silica coating of SPIONs. One of them is called Stober method, and it depends on the hydrolysis and condensation of a sol-gel precursor such as tetraethyl orthosilicate (TEOS). Second method is based on microemulsion process. Reverse micelles is utilized to confine and direct the silica coating. These reverse micelles are formed by non-ionic surfactants.[115]

CHAPTER 2

EXPERIMENTAL PROCEDURES

2.1 General

^1H NMR and ^{13}C NMR spectra were recorded on Bruker DPX–400 (operating at 400 MHz for ^1H NMR and 100 MHz for ^{13}C NMR) in CDCl3 solvent with tetramethylsilane as internal standard. All spectra were recorded at 25 ^oC and coupling constants (J values) are given in Hz. Chemical shifts are given in parts per million (ppm). Mass spectra were recorded with Agilent Technologies 6224 TOF LC/MS. Absorption spectra were performed by using a Varian Cary–100 and Varian Cary 5000 UV-VIS-NIR absorption spectrophotometer. Fluorescence measurements were conducted on a Varian Eclipse spectrofluometer. Nano-ZS Zetasizer dynamic light scattering (DLS) system (Malvern Instruments, U.K.) was used to measure the particle size and surface charge of bodipy functionalized magnetic nanoparticles. TEM images were aquired in UNAM, Ankara, using FEI Technai G2 F30 high resolution transmission electron microscope and carbon gid. The dried, as-synthesized nanoparticles were characterized with X-ray powder diffractometry (XRD) (PANalytical X'Pert powder diffractometer, Netherlands) by using Cu Kα radiation in a range of $2\theta = 20–70^o$. The infrared spectra of the nanoparticles were obtained by using a Fourier transform infrared spectrometer (FTIR) (Bruker-VERTEX70, Germany). X-ray photoelectron spectroscopy (XPS) measurements were carried with Thermo Scientific, K-Alpha-Monochromated high-performance XPS spectrometer. VSM measurements have been performed with use of Quantum Design PPMS (9T) system at the Gebze Institute of Technology, Gebze-Kocaeli, Turkey.

All chemicals and solvents purchased from Aldrich and Merck were used without further purification. Column chromatography of all products was performed using Merck Silica Gel 60 (particle size: 0.040–0.063 mm, 230–400 mesh ASTM). Reactions were monitored by thin layer chromatography using Merck TLC Silica gel 60 F254. Anhydrous tetrahydrofuran was obtained by refluxing over sodium/benzophenone prior to use. In singlet oxygen measurements 1,3-Diphenylisobenzofuran was used as a singlet oxygen trap in dichloromethane and isopropyl alcohol measurements and was purchased from Sigma.

2.2 Experimental Part

2.2.1 Design of Nanoplatform for PDT and MRI

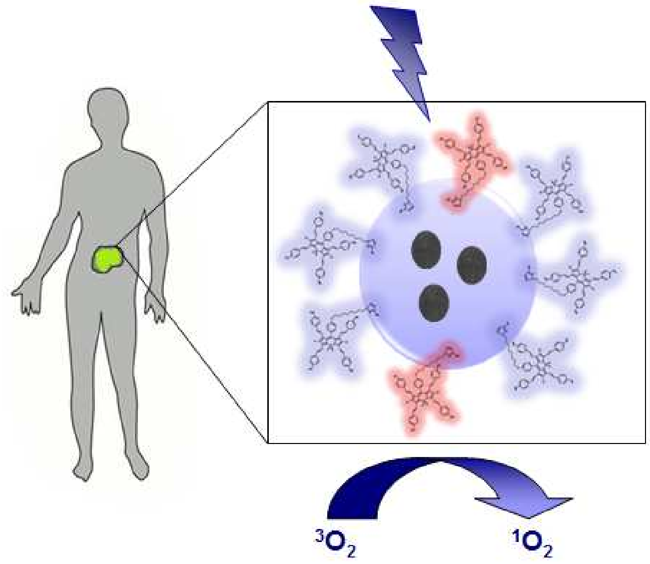

Figure 13: *Representative Design of Target Nanoplatform*

In this study, four different BODIPY-based PSs (**Compound 13, 14, 15, 16**) are attached to SPIONs core- silica shell nanoparticles. Bromines are attached to enhance intersystem crossing, thus provide spin forbidden singlet-triplet transition leading to enhanced singlet oxygen production. In our design, SPIONs are synthesized as a MRI contrast agent. Then, it is covered with silica shell which prevents agglomeration of SPIONs. In addition, it provides a platform which is easily functionalized.

2.2.2 Synthesis of Photosensitizers

2.2.2.1 Synthesis of Compounds 2, 3, 4, 5

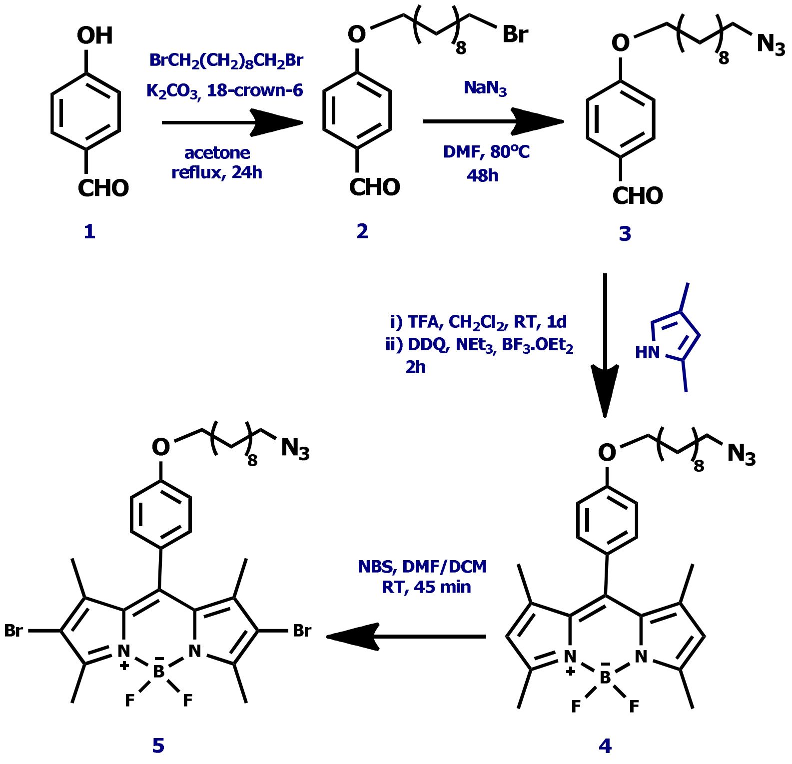

Figure 14: *Synthesis of Compounds 2, 3, 4, 5*

Synthesis of Compound 2:

1,4-hydroxybenzaldehyde (1.25 g, 10 mmol) and 1,10 dibromodecane (9.2 mL, 40 mmol) were dissolved in acetone (400 mL). K_2CO_3 (6.9 g, 50 mmol) and a few crystals of 18-crown–6 were added. The reaction mixture was refluxed for 24 h at 55–56 ^{o}C. Then, acetone was evaporated in vacuo and extracted with water and chloroform. Organic layer is dried with Na_2SO_4 and evaporated in vacuo. The product was purified by silica gel column chromatography using Hex/EtOAc (75:25, v/v). Fraction containing compound 2 was collected, then the solvent was removed under reduced pressure to yield the desired product as a white solid (1.69 g, 48.3%).

^{1}H NMR (400 MHz, $CDCl_3$): δ 9.90 (s, 1H), 7.89 – 7.79 (m, 2H), 7.01 (dd, J = 9.1, 2.2 Hz, 2H), 4.06 (t, J = 6.5 Hz, 2H), 3.43 (t, J = 6.9 Hz, 2H), 1.93 – 1.76 (m, 4H), 1.48 (td, J = 14.3, 7.0 Hz, 4H), 1.43 – 1.22 (m, 9H).

^{13}C NMR (100 MHz, CDCl3, δ ppm): 190.42, 164.14, 131.83, 129.71, 114.68, 68.31, 33.92, 32.76, 29.37, 29.30, 29.23, 29.00, 28.68, 28.10, 25.89. MS HRMS (TOF-APCI): m/z calculated for $[M+H]^+$ 341. 1100, found 341.1098, Δ = -0.58 ppm

Synthesis of Compound 3:

4-(10-bromodecyloxy) benzaldehyde, **compound 2**, (1.5 g, 4.4 mmol) and NaN_3 (2.3 g, 35.2 mmol) were dissolved in 20 mL DMF. Then, a few crystals of benzo-18-crown-6 and 100 mg KI were added to the reaction flask. This reaction mixture was then heated to 80 ^oC and stirred at this temperature for 48 hours. The mixture was extracted six times with water and chloroform to remove DMF. Organic layer was dried with Na_2SO_4 and evaporated in vacuo. The product was purified by silica gel column chromatography using $CHCl_3$/Hex (1:2, v/v). Fraction containing compound 3 was collected, then the solvent was removed under reduced pressure to yield the brown oily product (1.29 g, 96.9%).

^{1}H NMR (400 MHz, $CDCl_3$): δ 9.80 (s, 1H), 7.81 – 7.62 (m, 2H), 6.96 – 6.77 (m, 2H), 3.96 (t, *J* = 6.5 Hz, 3H), 3.18 (t, *J* = 6.9 Hz, 3H), 1.73 (dq, *J* = 13.1, 6.6 Hz, 3H), 1.57 – 1.46 (m, 3H), 1.44 – 1.33 (m, 3H), 1.26 (d, *J* = 16.9 Hz, 13H).

^{13}C NMR (100 MHz, $CDCl_3$, δ ppm): 190.7, 164.26, 131.97, 129.77, 114.75, 68.39, 51.47, 29.40, 29.37, 29.27, 29.09, 29.04, 28.82, 26.69, 25.93. MS HRMS (TOF-APCI): m/z calculated for $[M+H]^+$ 304.2001, found 304.2005, Δ = 1.32 ppm

Synthesis of Compound 4:

4-(10-azidodecyloxy) benzaldehyde, **compound 3**, (1 g, 3.30 mmol) and 2,4-dimethyl pyrrole (0.725 g, 7.6 mmol) were added to 400 mL CH_2Cl_2 which was purged with Ar for 30 min. The color of the solution turned into red after the addition of 3 drops of trifluoroacetic acid. The reaction mixture was stirred at room temperature for 24 h. After 24 h, 1.054 g DDQ (2,3-dichloro-5,6-dicyanobenzoquinone) was added and the reaction mixture was stirred at room temperature for 60 min. Then, triethyl amine (5 mL) and boron trifluoride diethyl etherate (5 mL) were added sequentially. After stirring at room temperature for 60 min, it was extracted with water. Organic layer was dried with Na_2SO_4 and evaporated under vacuo. First, the product was purified by silica gel column chromatography using $CHCl_3$. Then, second silica gel column chromatography using Hex/EtOAc (3:1, v/v) was performed for further purification. Fraction containing compound 4 was collected, and then the solvent was removed under reduced pressure (414 mg, 0.79 mmol, 24 %).

^{1}H NMR (400 MHz, $CDCl_3$): δ 7.05 (d, *J* = 8.4 Hz, 2H), 6.89 (d, *J* = 10.3 Hz, 2H), 5.89 (s, 2H), 3.92 (t, *J* = 6.6 Hz, 2H), 3.14 (t, J = 6.9 Hz, 2H), 2.46 (s, 6H), 1.79 – 1.68 (m, 2H), 1.57 – 1.46 (m, 2H), 1.40 (m, *J* = 14.8, 7.0 Hz, 2H), 1.35 (s, 6H), 1.32 – 1.21 (m, 12H).

^{13}C NMR (100 MHz, $CDCl_3$, δ ppm): 159.74, 155.18, 143.17, 142.01, 128.38, 126.81, 121.07, 116.98, 114.04, 68.14, 51.47, 29.44, 29.40, 29.26, 29.13, 28.84, 26.71, 26.06, 14.56. MS HRMS (TOF-APCI): m/z calculated for $[M]^+$ 521.3100, found 521.3131, Δ = 5.95 ppm

Synthesis of Compound 5:

1,3,5,7-Tetramethyl-8-(4-(10-azidodecyloxy))-4,4-difloroboradiaza-s indacene, **compound 4**, (200 mg, 0.384 mmol) was dissolved in DMF/DCM mixture (15 mL: 15 mL). Then, *N*-bromosuccinimide; NBS (0.157 g, 0.882 mmol) was dissolved in 15 mL DCM and added to previous solution dropwise. Followed by TLC, it was stirred at room temperature for 45 min. Then, it was extracted with water and dichloromethane five times. Organic layer was dried with Na_2SO_4 and evaporated in vacuo. The product was purified by silica gel column chromatography using Hex/EtOAc (5.25:1, v/v). Fraction containing compound 5 was collected, then the solvent was removed under reduced pressure to give red waxy product (247 mg, 0.365 mmol, 95 %).

^{1}H NMR (400 MHz, $CDCl_3$): δ 7.14 (d, 2H), 7.04 (d, *J* = 4.1, 2.3 Hz, 2H), 4.04 (t, *J* = 6.4 Hz, 2H), 3.28 (t, *J* = 6.4 Hz 2H), 2.62 (s, 6H), 1.89 – 1.79 (m, 2H), 1.63 (p, *J* = 6.8 Hz, 2H), 1.51 (dd, *J* = 14.9, 7.6 Hz, 2H), 1.45 (s, 6H), 1.38 (d, *J* = 16.9 Hz, 10H).

^{13}C NMR (100 MHz, $CDCl_3$, δ ppm): 160.15, 153.68, 142.48, 140.66, 130.62, 129.55, 127.44, 126.09, 116.52, 111.65, 68.19, 51.48, 29.44, 29.40, 29.22, 29.14, 28.85, 26.72, 26.05, 23.76, 22.99, 13.86, 13.65. MS HRMS (TOF-APCI): m/z calculated for $[M-F]^+$ 660.1343, found 660.1362 , Δ = -2.88 ppm

2.2.2.2 Synthesis of Compounds 7 and 8

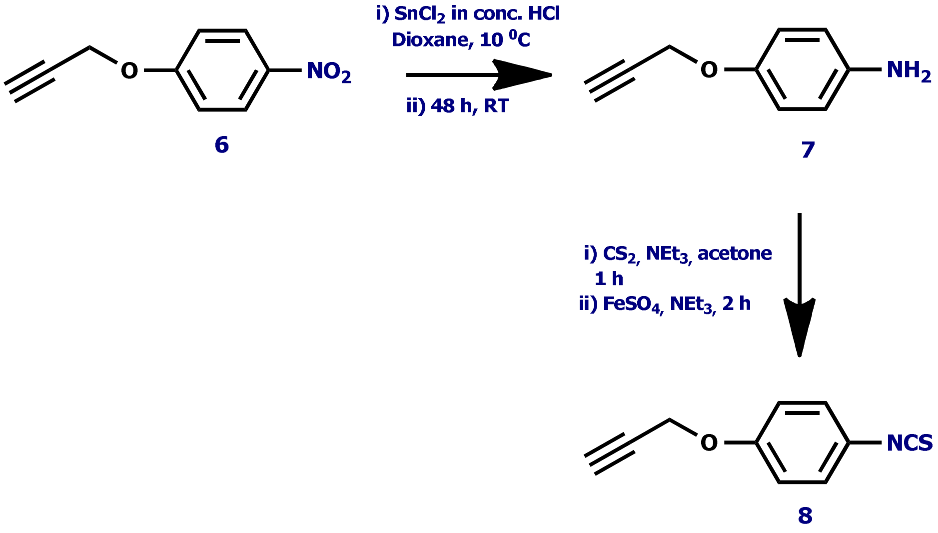

Figure 15: *Synthesis of Compounds 7 and 8*

Synthesis of Compound 7:

Compound 7, p-aminophenyl propargyl ether, was prepared according to the literature.[115] Stannous chloride dihydrate (10.15 g, 45 mmol) was dissolved in 25 mL concentrated HCl. Then, cooled solution of stannous chloride dihydrate was added dropwise to a solution of p-nitrophenyl propargyl ether (1.595 g, 9 mmol) in dioxane at 10 ^{o}C. The reaction mixture was stirred for 48 h at room temperature. Then, it was neutralized with aqueous sodium hydroxide, the solution was extracted with dichloromethane (4 × 50 mL). Organic layer was dried with Na_2SO_4 and evaporated in vacuo. The product was purified by silica gel column chromatography using $CHCl_3$/Hex (3:1, v/v). After the removal of solvent under reduced pressure, it was crystallized to yield brownish platelet crystals (800 mg, 65 %).

^{1}H NMR (400 MHz, $CDCl_3$): δ 6.76 – 6.72 (m, 2H), 6.72 – 6.45 (m, 2H), 4.51 (t, J = 2.0 Hz, 2H), 3.37 (s, 2H), 2.49 – 2.32 (m, 1H).

^{13}C NMR (100 MHz, $CDCl_{3,}$ δ ppm): 150.70, 140.97, 116.42, 116.23, 79.16, 75.17, 56.76 MS HRMS (TOF-APCI): m/z calculated for $[M+H]^+$ 148.0762, found 148.0765 , Δ = 0.01 ppm

Synthesis of Compound 8:

Compound 8, p-isothiocyanatophenyl propargyl ether, was synthesized according to the literature with slight modifications.[116] Compound 7, p-aminophenyl propargyl ether, (600 mg, 4.08 mmol) is dissolved in acetone (5 mL). Then, carbon disulfide (0.2 mL), triethylamine (2.3 mL) was added to the reaction mixture.

The mixture was allowed to stir at room temperature for 1 h. Catalytic amount ferrous sulfate and triethylamine was added to this reaction flask, and the stirring was continued for 2 h. When starting material was consumed, excess carbon disulfide was removed by distillation. After quenching the reaction mass in 25 mL ice-cold water with constant stirring, the product was isolated by filtration and dried under vacuo. The product was purified by silica gel column chromatography using $CHCl_3$/Hex (50:50, v/v). Fraction containing compound 8 was collected, then the solvent was removed under reduced pressure to yield the white platelet crystals (341 mg, 44 %).

^{1}H NMR (400 MHz, $CDCl_3$): δ 7.31 – 7.14 (m, 2H), 7.01 – 6.89 (m, 2H), 4.70 (dd, *J* = 12.7, 2.4 Hz, 2H), 2.59 – 2.50 (m, 1H).

^{13}C NMR (100 MHz, $CDCl_{3,}$ δ ppm): 155.69, 134.29, 126.25, 123.87, 115.20, 77.18, 75.37, 55.38. MS HRMS (TOF-APCI): m/z calculated for $[M\text{-}NCS]^-$ 132.0575, found 132.0315, Δ = 196. 88 ppm

2.2.2.3 Synthesis of Compound 9

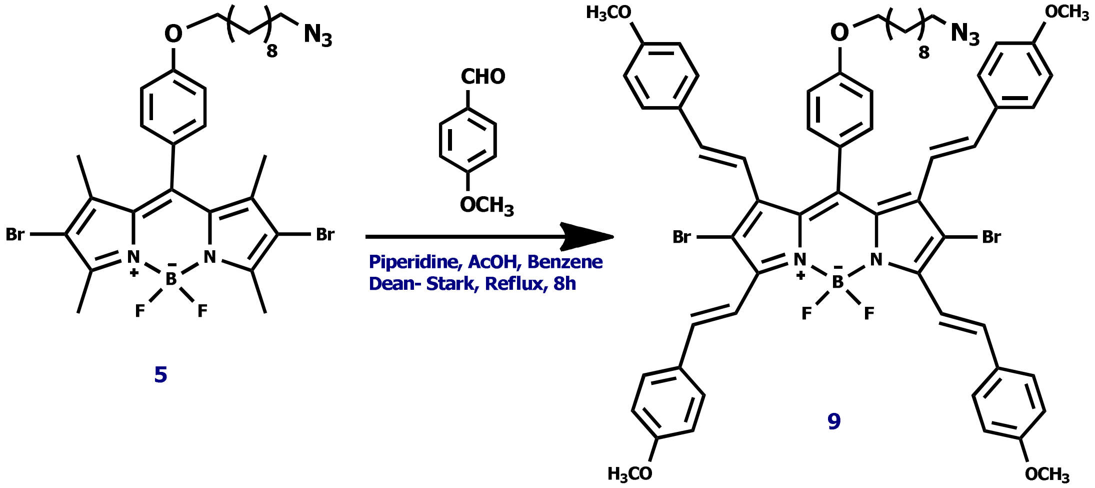

Figure 16: *Synthesis of Compound 9*

2,6-Dibromo-1,3,5,7-Tetramethyl-8-(4-(10-azidodecyloxy))-4,4 difloroboradiaza-s-indacene, **compound 5**, (190 mg, 0.292 mmol) and 4-methoxybenzaldehyde (318 mg, 2.34 mmol) were dissolved in benzene (45 mL). Piperidine (0.5 mL) and glacial acetic acid (0.5 mL) were added respectively. The reaction mixture was refluxed using Dean-Stark apparatus at 110 ^{o}C. When the solution was concentrated, reaction was followed by TLC until dark green colored product became the major product. Then, benzene was evaporated in vacuo. It was extracted with $CHCl_3$ and water. Organic layer was dried with Na_2SO_4 and evaporated under reduced pressure. Then, it was dissolved in minimum amount of chloroform and precipitated in methanol to remove aldehyde. The product was purified by silica gel column chromatography using $CHCl_3$/MeOH (99:1, v/v). Fraction containing compound 9 was collected, then the solvent was removed under reduced pressure to get compound 9 as dark green powder (219 mg, 65%).

^{1}H NMR (400 MHz, $CDCl_3$): δ 8.15 (d, J = 16.7 Hz, 2H), 7.65 (t, J = 9.8 Hz, 6H), 7.26 (d, J = 8.5 Hz, 2H), 7.20 (t, J = 8.9 Hz, 1H), 7.06 – 6.89 (m, 13H), 6.77 (d, J

= 8.7 Hz, 4H), 5.71 (d, *J* = 16.5 Hz, 2H), 3.90 (s, 6H), 3.82 (s, 8H), 3.30 (t, *J* = 6.9 Hz, 2H), 1.85 (dd, *J* = 14.8, 7.6 Hz, 3H), 1.64 (dd, *J* = 13.6, 6.8 Hz, 2H), 1.55 (d, *J* = 16.4 Hz, 4H), 1.38 (s, 12H), 1.30 – 1.22 (m, 6H).

^{13}C NMR (100 MHz, $CDCl_3$, δ ppm): 160.79, 160.24, 159.75 , 139.20, 134.54, 131.49, 129.75, 129.31, 127.98 , 126.94 , 126.37, 118.34, 116.14 , 115.75, 115.34, 114.34, 113.78, 68.22, 56.08 , 55.42, 55.24, 51.50, 29.70, 29.54, 29.48, 29.19, 28.87, 26.75, 26.30. MS HRMS (TOF-APCI): m/z calculated for $[M]^+$ 1151.3002, found 1151.3065, Δ = 5.47 ppm

2.2.2.4 Synthesis of Compound 10

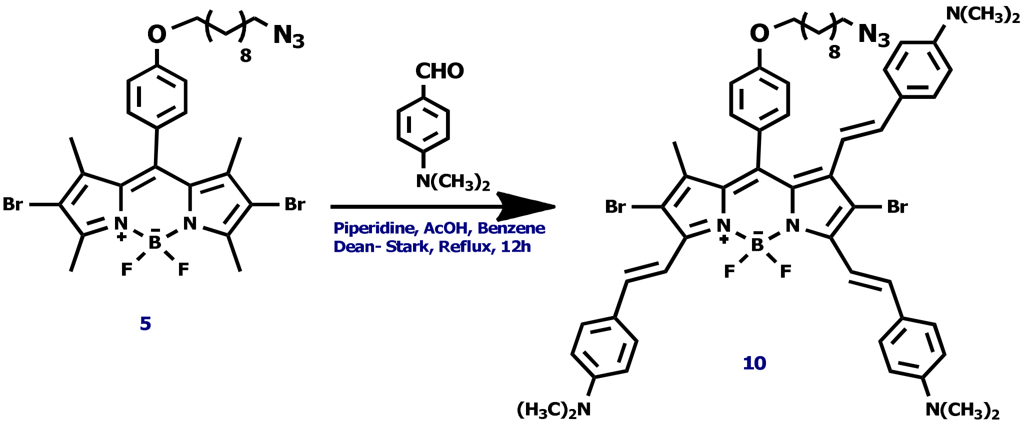

Figure 17: *Synthesis of Compound 10*

2,6-Dibromo-1,3,5,7-Tetramethyl-8-(4-(10-azidodecyloxy))-4,4-difloroboradiaza-s-indacene, **compound 5**, (100 mg, 0.154 mmol) and 4-(Dimethylamino)-benzaldehyde (160 mg, 1.078 mmol) were added to a 100 mL round-bottomed flask containing 45 mL benzene. Piperidine (0.5 mL) and glacial acetic acid (0.5 mL) were added respectively to this mixture. The reaction mixture was refluxed using Dean-Stark apparatus at 115 °C and the reaction was monitored by TLC. When black colored product became the major product, the mixture was cooled to room temperature and solvent was evaporated. It was extracted with $CHCl_3$ and water. Organic layer was dried with Na_2SO_4 and evaporated under reduced pressure. Then, it was dissolved in minimum amount of chloroform and precipitated in methanol to remove aldehyde. The product was purified by silica gel column chromatography using $CHCl_3$. It yielded compound 10 as black colored powder (50 mg, 30%).

^{1}H NMR (400 MHz, $CDCl_3$): δ 8.14 (d, *J* = 15.9 Hz, 2H), 7.60 (s, 6H), 7.21 (d, *J* = 7.1 Hz, 2H), 7.02 (d, *J* = 14.5 Hz, 3H), 6.89 (d, *J* = 7.2 Hz, 2H), 6.75 (s, 4H), 6.57 (d, *J* = 7.6 Hz, 2H), 5.59 (d, *J* = 16.9 Hz, 1H), 3.94 (s, 2H), 3.21 (d, *J* = 57.3 Hz, 2H), 3.06 (s, 12H), 2.98 (s, 6H), 1.85 (s, 3H), 1.63 (s, 3H), 1.50 (s, 6H), 1.35 (s, 12H), 1.27 (s, 3H).

^{13}C NMR (100 MHz, $CDCl_{3,}$ δ ppm): 159.94, 151.21, 151.14, 150.29, 139.99, 139.27, 134.84, 130.80, 129.39, 129.27, 127.90, 127.14, 127.01, 125.53, 125.45, 122.56, 116.25, 115.75, 115.23, 112.1, 112.13, 111.90, 68.1 , 62.34 , 50.50, 40.35 , 40.31, 40.28, 30.27, 29.69, 29.49, 29.45, 29.36 , 28.99, 26.49 , 26.19 , 14.11, 8.68 . MS HRMS (TOF-APCI): m/z calculated for $[M+H]^+$ 1073.3610, found 1073.3669 , Δ = 5.49 ppm

2.2.2.5 Synthesis of Compound 11

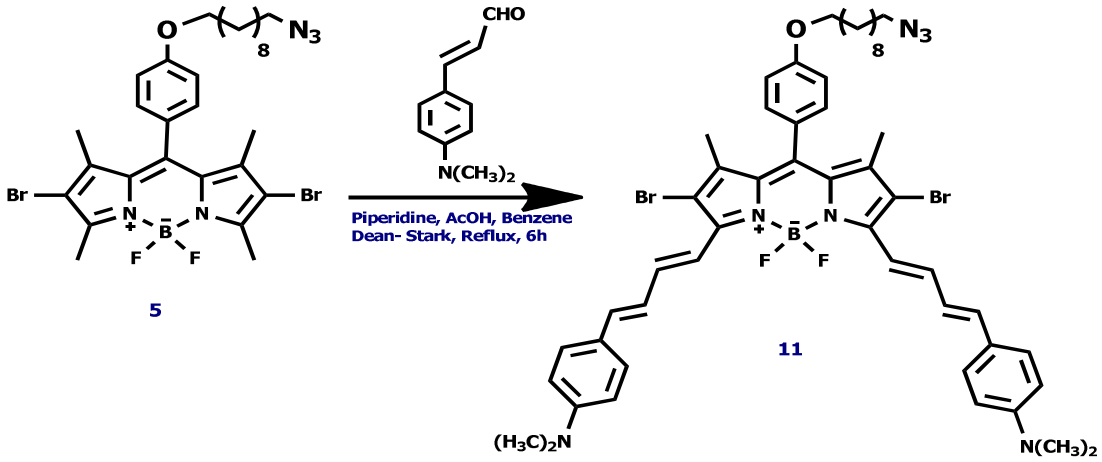

Figure 18: *Synthesis of Compound 11*

2,6-Dibromo-1,3,5,7-Tetramethyl-8-(4-(10-azidodecyloxy))-4,4-difloroboradiaza-s-indacene, **compound 5**, (100 mg, 0.154 mmol) and trans-4-(Dimethylamino)-cinnamaldehyde (81 mg, 0.462 mmol) were dissolved in benzene (60 mL). Piperidine (0.4 mL) and glacial acetic acid (0.4 mL) were added respectively. The reaction mixture was refluxed using Dean-Stark apparatus at 100 ^{o}C. When the solution was concentrated, reaction was followed by TLC until black colored product became the major product. Then, benzene was evaporated in vacuo. It was extracted with $CHCl_3$ and water. Organic layer was dried with Na_2SO_4 and evaporated under reduced pressure. The product was purified by silica gel column chromatography using $CHCl_3$/Hex (75:25, v/v). Fraction containing compound 11 was collected then the solvent was removed under reduced pressure (70 mg, 46%).

^{1}H NMR (400 MHz, $CDCl_3$): δ 8.15 (dd, *J* = 16.4, 11.0 Hz, 1H), 8.09 – 7.96 (m, 1H), 7.67 – 7.56 (m, 3H), 7.42 (dd, *J* = 11.7, 9.5 Hz, 2H), 7.26 – 7.13 (m, 3H), 7.06 – 6.95 (m, 3H), 6.84 (dd, *J* = 15.2, 8.8 Hz, 1H), 6.73 (dt, *J* = 22.1, 9.9 Hz, 4H), 4.05 (t, *J* = 6.3 Hz, 2H), 3.28 (t, 2H), 3.07 (s, 6H), 3.04 (s, 5H), 1.86 (s, 2H), 1.63 (dd, *J* = 13.6, 6.7 Hz, 2H), 1.52 (dd, *J* = 17.3, 9.9 Hz, 3H), 1.50 – 1.44 (m, 6H), 1.36 (s, 11H).

^{13}C NMR (100 MHz, $CDCl_{3,}$ δ ppm): 159.93, 151.22, 150.56, 140.0,139.56, 139.17, 138.39, 137.93, 129.86, 129.43, 129.34, 128.55, 128.48, 127.06, 126.44, 126.32, 125.45, 125.34, 119.90, 115.16, 113.91, 112.17, 68.22 , 51.50, 40.29, 29.45, 29.41, 29.25, 29.15, 28.85, 26.73, 26.06, 13.89 , 13.86, 13.76. MS HRMS (TOF-APCI): m/z calculated for $[M]^+$ 993.3110, found 993.3131, Δ = 2.11 ppm

2.2.2.6 Synthesis of Compound 12

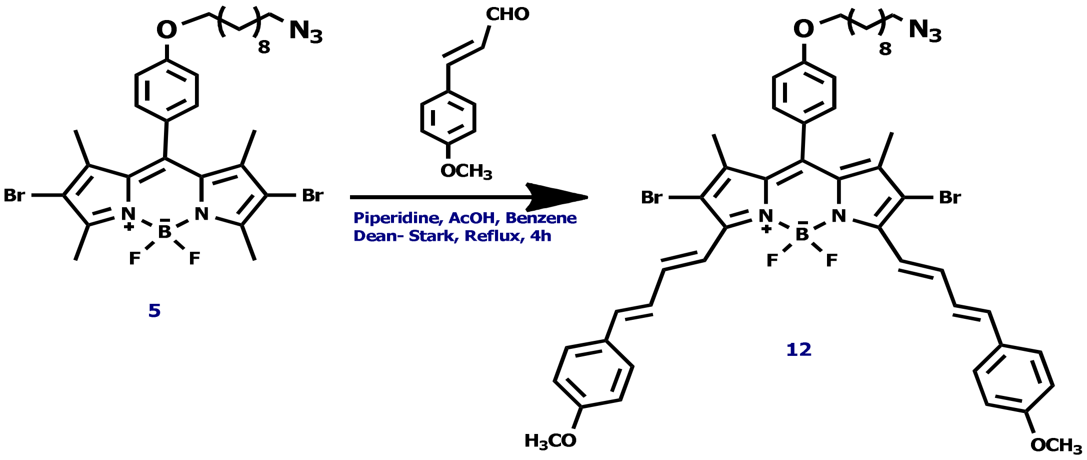

Figure 19: *Synthesis of Compound 12*

2,6-Dibromo-1,3,5,7-Tetramethyl-8-(4-(10-azidodecyloxy))-4,4-difloroboradiaza-s-indacene, **compound 4**, (100 mg, 0.154 mmol) and trans-4-methoxycinnamaldehyde (75 mg, 0.462 mmol) were added to a 100 mL round-bottomed flask containing 60 mL benzene. Piperidine (0.4 mL) and glacial acetic acid (0.4 mL) were added respectively to this mixture. The reaction mixture was refluxed using Dean-Stark apparatus at 95 °C and the reaction was monitored by TLC. When green colored product became the major product, the mixture was cooled to room temperature and solvent was evaporated. It was extracted with $CHCl_3$ and water. Organic layer was dried with Na_2SO_4 and evaporated under reduced pressure. The product was purified by silica gel column chromatography using $CHCl_3$/Hex (80:20, v/v). It yielded light green colored powder (82 mg, 55%).

^{1}H NMR (400 MHz, $CDCl_3$): δ 8.01 (t, *J* = 18.1 Hz, 1H), 7.92 (dd, *J* = 15.7, 10.7 Hz, 1H), 7.60 – 7.44 (m, 2H), 7.37 (dd, *J* = 8.7, 3.5 Hz, 3H), 7.19 (dd, *J* = 15.7, 10.7 Hz, 2H), 7.10 – 6.98 (m, 2H), 6.97 – 6.90 (m, 2H), 6.87 (dd, *J* = 15.2, 6.6 Hz, 2H), 6.85 – 6.70 (m, 4H), 3.94 (t, *J* = 6.5 Hz, 2H), 3.74 (dt, *J* = 12.5, 9.5 Hz, 6H), 3.19 (t, *J* = 6.9 Hz, 2H), 1.82 – 1.63 (m, 2H), 1.59 – 1.48 (m, 2H), 1.45 – 1.35 (m, 7H), 1.35 – 1.16 (m, 13H).

^{13}C NMR (101 MHz, $CDCl_3$): δ 167.75, 160.76 , 160.09 , 132.47, 130.87, 129.85 129.64, 129.27, 128.80, 128.42, 126.68, 115.30, 114.32, 68.20, 55.38, 51.49, 38.74, 30.37, 29.70, 29.3, 28.89, 26.72, 26.05, 23.75, 22.83, 14.21, 13.59, 10.96. MS HRMS (TOF-APCI): m/z calculated for $[M-H]^-$ 966.2399, found 966.2211, Δ = -19.46 ppm

2.2.2.7 Synthesis of Compound 13

Both **compound 8** (0.13 mmol, 24 mg) and **compound 9** (0.065 mmol, 75 mg) were dissolved in a 10 mL round-bottomed flask containing 2 mL $CHCl_3$ and 1 mL EtOH. Saturated solution of Sodium ascorbate and $CuSO_4.5H_2O$ were prepared in 1 mL water, separately. Then, 0.75 mL of $CuSO_4$ and 0.75 mL of Sodium ascorbate solution were added to the flask, respectively. Catalytic amount of copper powder is added to this reaction mixture. The reaction was allowed to stirred for 8 h. Copper powder was eliminated by using filtration paper. Then, it was extracted with $CHCl_3$ and water. Organic layer was dried with Na_2SO_4 and evaporated under reduced pressure. The product was purified by silica gel column chromatography using $CHCl_3$/methanol (98:2, v/v). Fraction containing **compound 13** was collected, then the solvent was removed under reduced pressure (56 mg, 64%). **Extinction coefficient (Ɛ)**; 76,633 $cm^{-1}mol^{-1}L$ in $CHCl_3$. **λ_{abs}:** 698 nm

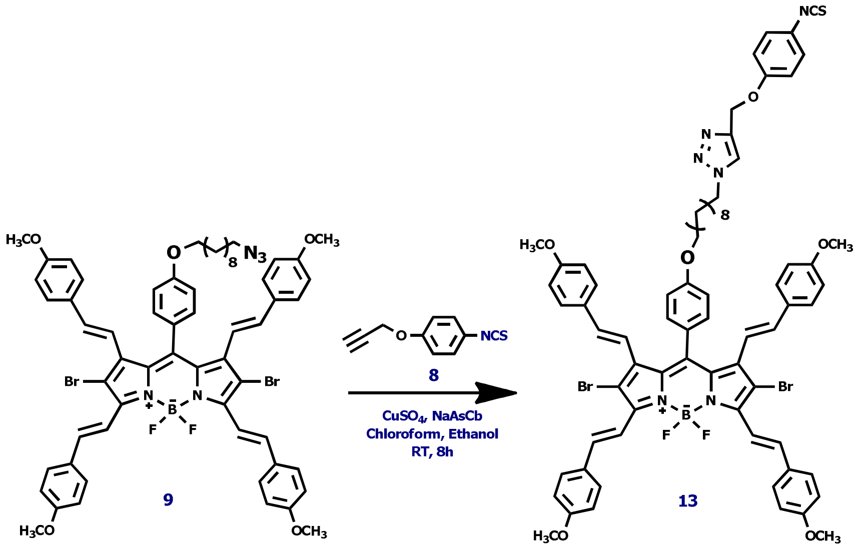

Figure 20: *Synthesis of Compound 13*

^{1}H NMR (400 MHz, $CDCl_3$): δ 8.15 (d, *J* = 16.6 Hz, 2H), 7.65 (d, *J* = 7.2 Hz, 5H), 7.59 (t, *J* = 11.0 Hz, 2H), 7.24 (d, *J* = 8.5 Hz, 2H), 7.18 (dd, *J* = 6.8, 2.1 Hz, 2H), 7.03 (s, 1H), 7.00 – 6.95 (m, 7H), 6.93 (d, *J* = 8.7 Hz, 6H), 6.76 (d, *J* = 8.6 Hz, 4H), 5.70 (d, *J* = 16.6 Hz, 2H), 5.21 (s, 2H), 4.38 (t, *J* = 7.2 Hz, 2H), 3.84 (d, 14H), 1.94 (d, *J* = 6.6 Hz, 2H), 1.88 – 1.77 (m, 2H), 1.56 (d, *J* = 36.0 Hz, 3H), 1.47 – 1.25 (m, 13H).

^{13}C NMR (100 MHz, $CDCl_{3,}$ δ ppm): 160.80, 160.22, 159.73, 157.17, 149.32, 140.19, 139.22, 138.26, 134.44, 133.05, 131.50, 130.87, 129.83, 129.66, 129.32, 128.80, 127.98, 127.01, 126.38, 124.23, 122.53, 118.35, 116.12, 115.75, 115.34, 114.34, 113.78, 105.93, 68.19, 62.36, 55.34, 50.49, 30.32, 29.46, 29.36, 28.97, 26.49, 26.27, 23.76, 22.98. MS HRMS (TOF-APCI): m/z calculated for $[M]^+$ 1340.3250, found 1340.3359 , Δ = 8.13 ppm

2.2.2.8 Synthesis of Compound 14

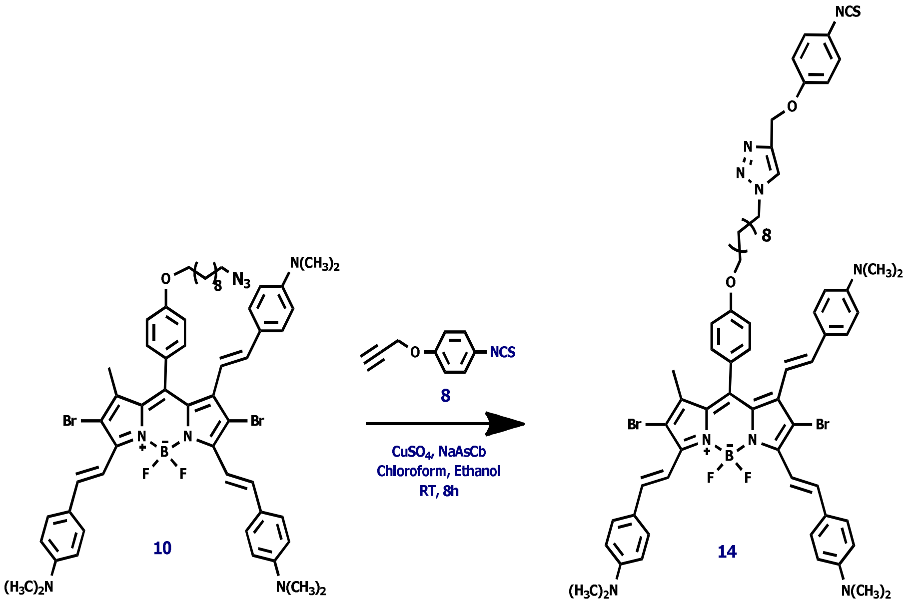

Figure 21: *Synthesis of Compound 14*

Both **compound 8** (0.094 mmol, 17 mg) and **compound 10** (0.047 mmol, 50 mg) were dissolved in a 10 mL round-bottomed flask containing 1.5 mL $CHCl_3$ and 0.5 mL EtOH. Saturated solution of Sodium ascorbate and $CuSO_4.5H_2O$ were prepared in 1 mL water, separately. Then, 0.75 mL of $CuSO_4$ and 0.75 mL of Sodium ascorbate solution were added to the flask, respectively. Catalytic amount of copper powder is added to the this reaction mixture. The reaction was allowed to stirred for 8 h. Copper powder was eliminated by using filtration paper. Then, It was extracted with $CHCl_3$ and water. Organic layer was dried with Na_2SO_4 and evaporated under reduced pressure. The product was purified by silica gel column chromatography using $CHCl_3$/methanol (99:1, v/v). Fraction containing **compound 14** was collected, then the solvent was removed under reduced pressure (35 mg, 59%). **Extinction coefficient (Ɛ)**; 57,888 $cm^{-1}mol^{-1}L$ in $CHCl_3$. **ʎ $_{\text{abs}}$:** 755 nm

^{1}H NMR (400 MHz, $CDCl_3$). δ 8.08 (d, *J* = 3.7 Hz, 1H), 8.04 (d, *J* = 3.8 Hz, 1H), 7.58 – 7.45 (m, 7H), 7.10 (ddd, *J* = 10.1, 8.1, 6.0 Hz, 4H), 6.96 (s, 1H), 6.89 (ddd, *J* = 12.4, 7.1, 3.0 Hz, 4H), 6.81 (d, *J* = 8.8 Hz, 2H), 6.68 (dd, *J* = 8.9, 4.1 Hz, 4H), 6.48 (d, *J* = 8.9 Hz, 2H), 5.50 (d, *J* = 16.5 Hz, 1H), 5.12 (s, 2H), 4.28 (t, *J* = 7.3 Hz, 2H), 3.98 – 3.79 (m, 2H), 2.98 (s, 11H), 2.89 (s, 6H), 1.84 (dd, *J* = 16.4, 9.5 Hz, 2H), 1.80 – 1.70 (m, 2H), 1.50 (s, 2H), 1.48 – 1.38 (m, 5H), 1.37 – 1.22 (m, 13H), 1.19 (d, *J* = 4.8 Hz, 4H).

^{13}C NMR (101 MHz, $CDCl_3$): δ 159.94, 156.56, 151.21, 151.14, 150.29, 139.99, 139.27, 134.84, 130.80, 129.39, 129.27, 127.90, 127.14, 127.01, 125.53, 125.44, 125.37 , 122.56 , 116.25, 115.75, 115.23, 113.62, 112.16, 112.13, 111.90, 68.17, 62.34 , 50.50 , 40.31, 30.27, 29.69, 29.43, 28.99, 26.49, 26.19, 14.11, 8.68. MS HRMS (TOF-APCI): m/z calculated for $[M]^+$ 1261.3781, found 1261.3803, Δ = 1.74 ppm

2.2.2.9 Synthesis of Compound 15

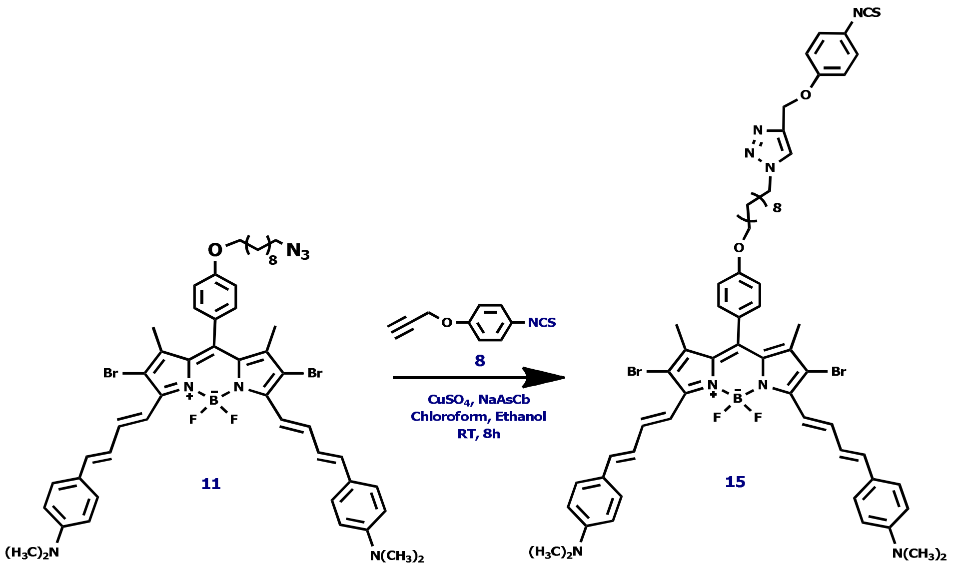

Figure 22: *Synthesis of Compound 15*

Both **compound 8** (0.065 mmol, 13 mg) and **compound 11** (0.050 mmol, 50 mg) were dissolved in a 10 mL round-bottomed flask containing 1.5 mL $CHCl_3$ and 0.5 mL EtOH. Saturated solution of Sodium ascorbate and $CuSO_4.5H_2O$ were prepared in 1 mL water, separately. Then, 0.5 mL of $CuSO_4$ and 0.5 mL of Sodium ascorbate solution were added to the flask, respectively. Catalytic amount of copper powder is added to this reaction mixture. The reaction was allowed to stirred for 8 h. Copper powder was eliminated by using filtration paper. Then, It was extracted with $CHCl_3$ and water. Organic layer was dried with Na_2SO_4 and evaporated under reduced pressure. The product was purified by silica gel column chromatography using $CHCl_3$. Fraction containing **compound 15** was collected, then the solvent was removed under reduced pressure (42 mg, 71%). **Extinction coefficient (Ɛ)**; 59,775 cm^{-1}mol^{-1}L in $CHCl_3$. **λ_{abs}:** 746 nm

^{1}H NMR (400 MHz, $CDCl_3$): δ 8.21 – 7.97 (m, 2H), 7.61 (dd, *J* = 12.3, 8.0 Hz, 4H), 7.43 (d, *J* = 7.1 Hz, 2H), 7.32 – 7.21 (m, 1H), 7.21 – 7.07 (m, 4H), 7.06 – 6.91 (m, 5H), 6.88 – 6.61 (m, 6H), 5.20 (s, 2H), 4.36 (t, *J* = 7.2 Hz, 2H), 4.04 (t, *J* = 6.2 Hz, 2H), 3.05 (dd, *J* = 11.9, 2.4 Hz, 12H), 1.96 – 1.74 (m, 4H), 1.47 (d, *J* = 5.0 Hz, 8H), 1.28 (dd, *J* = 19.9, 14.4 Hz, 13H).

^{13}C NMR (101 MHz, $CDCl_3$): δ 159.92, 151.24, 150.62, 140.10, 139.66, 139.20, 138.03, 136.77 , 134.30, 129.86, 129.43, 129.34, 128.54, 219.46, 76.91, 127.06, 126.31, 125.33, 122.62, 119.76, 115.76, 115.18, 113.85 , 112.17, 110.07, 68.19, 62.31, 50.49, 40.28 30.26, 29.41, 29.38, 29.32, 29.23, 28.98, 26.48, 26.04, 14.09, 13.49. MS HRMS (TOF-APCI): m/z calculated for [M]$^+$ 1182.3359, found 1182.3389, Δ = -2.53 ppm

2.2.2.10 Synthesis of Compound 16

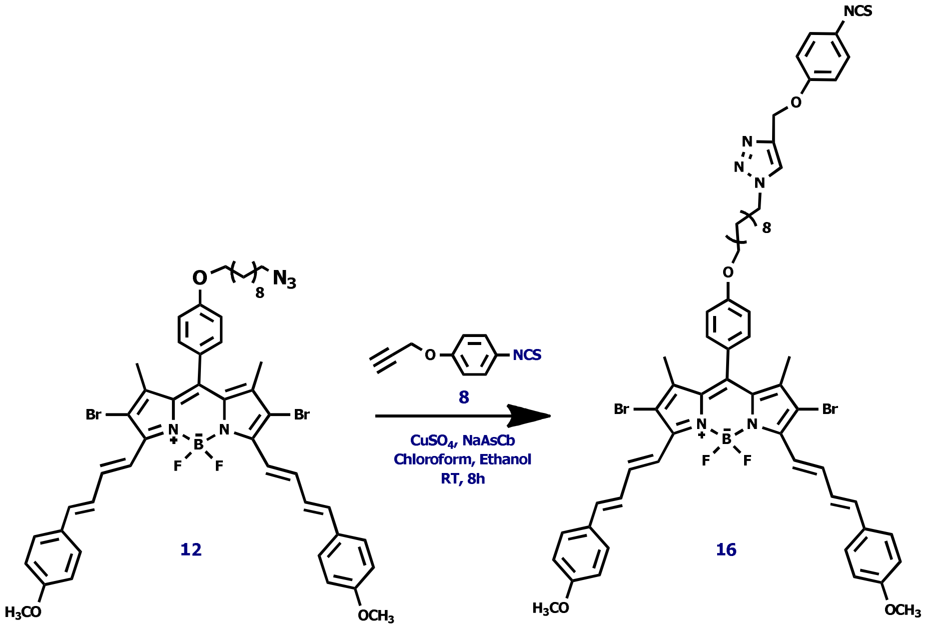

Figure 23: *Synthesis of Compound 16*

Both **compound 8** (0.107 mmol, 20 mg) and **compound 12** (0.083 mmol, 80 mg) were dissolved in a 10 mL round-bottomed flask containing 2 mL $CHCl_3$ and 1 mL EtOH. Saturated solution of Sodium ascorbate and $CuSO_4.5H_2O$ were prepared in 1 mL water, separately. Then, 0.5 mL of $CuSO_4$ and 0.5 mL of Sodium ascorbate solution were added to the flask, respectively. Catalytic amount of copper powder is added to this reaction mixture. The reaction was allowed to stirred for 8 h. Copper powder was eliminated by using filtration paper. Then, It was extracted with $CHCl_3$ and water. Organic layer was dried with Na_2SO_4 and evaporated under reduced pressure. The product was purified by silica gel column chromatography using $CHCl_3$. Fraction containing **compound 16** was collected, then the solvent was removed under reduced pressure (64 mg, 66%). **Extinction coefficient (Ɛ)**; 74,132 $cm^{-1}mol^{-1}L$ in $CHCl_3$. **λ_{abs}:** 689 nm

^{1}H NMR (400 MHz, $CDCl_3$): δ 8.13 (d, *J* = 16.6 Hz, 1H), 8.01 (dt, *J* = 24.6, 12.2 Hz, 1H), 7.69 – 7.57 (m, 3H), 7.46 (dt, *J* = 15.5, 7.7 Hz, 2H), 7.33 – 7.22 (m, 2H), 7.21 – 7.13 (m, 4H), 7.09 – 7.01 (m, 3H), 7.01 – 6.90 (m, 6H), 6.86 (dd, *J* = 15.4, 4.0 Hz, 1H), 5.21 (s, 2H), 4.37 (t, *J* = 7.2 Hz, 2H), 4.04 (t, *J* = 6.4 Hz, 2H), 3.87 (d, *J* = 9.3 Hz, 6H), 1.92 (dd, *J* = 16.2, 9.5 Hz, 2H), 1.84 (dd, *J* = 14.4, 6.9 Hz, 2H), 1.49 (dd, *J* = 10.3, 5.7 Hz, 8H), 1.35 (s, 11H).

^{13}C NMR (101 MHz, $CDCl_3$): δ 160.78, 160.08, 148.23, 147.88, 142.00, 140.55, 140.04, 138.68 , 137.40, 134.35, 132.64, 130.02, 129.37, 129.25, 128.40, 219.46, 76.86, 127.01, 126.66, 124.20, 122.56, 121.08, 116.01, 115.76, 115.29, 114.33, 110.46, 110.08, 68.22, 62.36, 55.39 , 50.48, 30.26, 29.39, 29.32, 29.23, 28.97, 26.47, 26.04, 13.90. MS HRMS (TOF-APCI): m/z calculated for $[M]^+$ 1156.2726, found 1156.2856, Δ = 11.24 ppm

2.3 Synthesis of Nanoparticles

2.3.1 Synthesis of Fe_3O_4 Nanoparticles

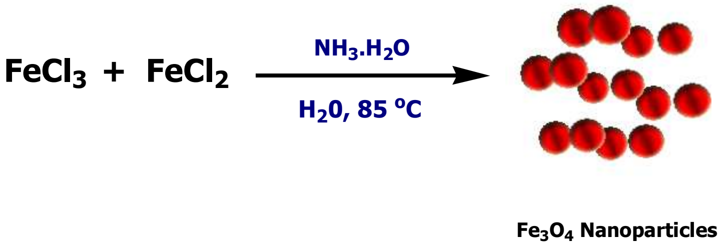

Figure 24: *Synthesis of* Fe_3O_4 *Nanoparticles*

Magnetic nanoparticles were prepared according to the method already described[117] with some modifications. 200 mL deionized water was bubbled with nitrogen gas at 85 °C for 10 minutes. Then, 3.225 g $FeCl_2.4H_2O$ and 8.96 g $FeCl_3.6H_2O$ were added to this reaction flask with vigorous stirring under nitrogen gas. 11.25 mL 25 % $NH_3.H_2O$ was then added quickly to the solution. The alkaline solution was stirred for 20 min and was subsequently cooled to ambient temperature. The sediment was separated by magnetic decantation method and washed twice with deionized water and ethanol. Then, the precipitates were dried at lyophilizer for 24 h and black powder is stored at room temperature.

2.3.2 Preparation of Water-Based Ferrofluid

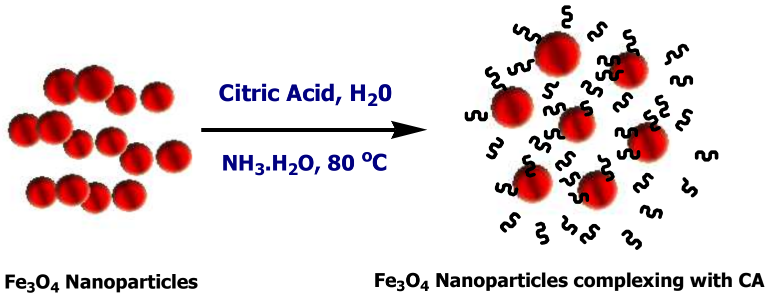

Figure 25: *Preparation of Water-Based Ferrofluid*

Stabilization of iron oxide nanoparticles with citrate groups were prepared[118] by mixing 2 g of powder Fe_3O_4 nanoparticles in 65 mL of aqueous solution of citric acid (containing 2.5 g of CA) under vigorous stirring. By adding concentrated ammonia solution, the pH value was adjusted to 5.2 and heated to 80 °C for 90 min. Then, the reaction was cooled to room temperature and pH value was increased to 10.1. To remove agglomerated nanoparticles, the suspension was centrifuged for 10 min at 6000 rpm.

2.3.3 Preparation of Fe_3O_4 @ SiO_2 Nanoparticles

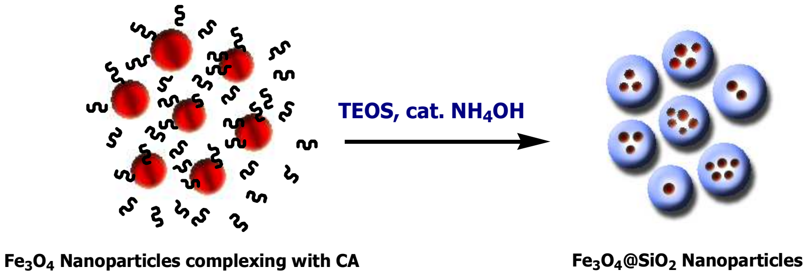

Figure 26: *Preparation of Fe_3O_4 @ SiO_2 Nanoparticles*

4 g of prepared water based magnetic ferrofluid was diluted with 120 mL water, and 480 mL ethanol. Then, 15 mL 25 % $NH_3.H_2O$ was added to this solution and this dispersion was homogenized by ultrasonic vibration in water bath for 30 min. Under mild mechanical stirring, 3 g tetraethyl orthosilicate was added slowly to the above dispersion. The reaction was allowed to proceed for 12 h. The $Fe_3O_4@SiO_2$ nanoparticles were separated from reaction medium by centrifuging at 6000 rpm for 10 min. The product was washed with ethanol and water, and then vacuum dried under lyophilizer for 24 h.

2.3.4 Preparation of Fe_3O_4 @ $SiO_2 – NH_2$ Nanoparticles

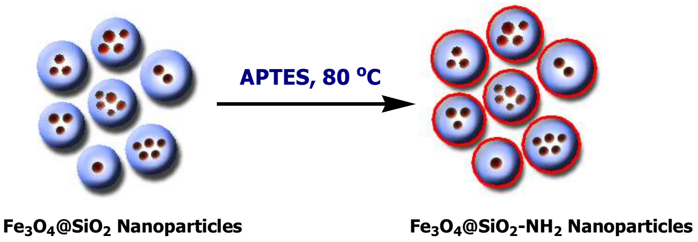

Figure 27: *Preparation of Fe_3O_4 @ $SiO_2 – NH_2$ Nanoparticles*

10 mg of $Fe_3O_4@SiO_2$ nanoparticles were dispersed in 20 mL ethanol for 20 min via ultrasonication, and then 100 μL (3-aminopropyl) triethoxysilane was added to the reaction mixture. The reaction was allowed to proceed at 80 ^{o}C for 5 h. The amino modified $Fe_3O_4@SiO_2$ nanoparticles were washed three times with ethanol, and then dried at lyophilizer for 24 h.

2.3.5 Preparation of Fe_3O_4 @ SiO_2 – Compound 13

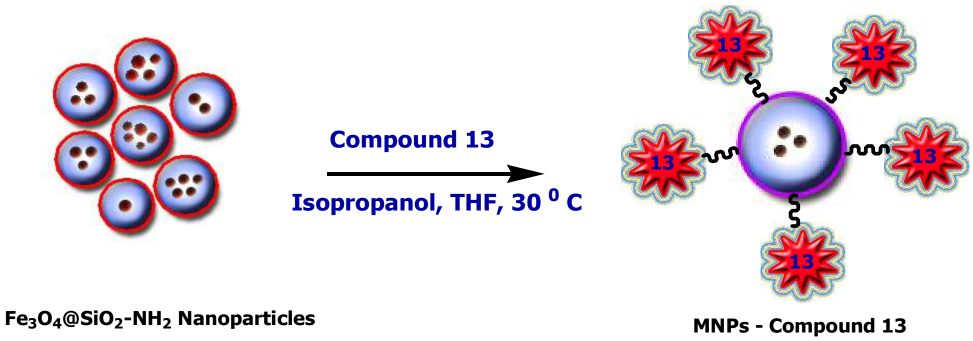

Figure 28: *Preparation of* Fe_3O_4 *@* SiO_2 *– Compound 13*

Tetrahydrofuran was distilled to obtain the solvent in anhydrous form, and then both THF and isopropyl alcohol was degassed with N_2 gas for 30 min. 25 mg of $Fe_3O_4@SiO_2\text{-}NH_2$ nanoparticles as a powder was added to 20 mL isopropanol and 1 mL THF solvent mixture, and sonicated for 15 min. 1.6 mg of compound 13 was added to this dispersion and continued sonication for 15 min. This reaction mixture was allowed to proceed at 30 ^{o}C under nitrogen at dark for 2 days. To separate MNPs – Compound 13 from reaction medium, it was centrifuged at 6000 rpm for 10 min. It was washed with chloroform three times to remove any non-binding compound 13. The solid was dried under lyophilizer for 24 h to give dark green solid. The content of compound 13 in MNPs was estimated to be about 0.064 mg **BODIPY**/mg **MNPs** from the absorbance spectra of nonbinding compound 13.

2.3.6 Preparation of Fe_3O_4 @ SiO_2 – Compound 14

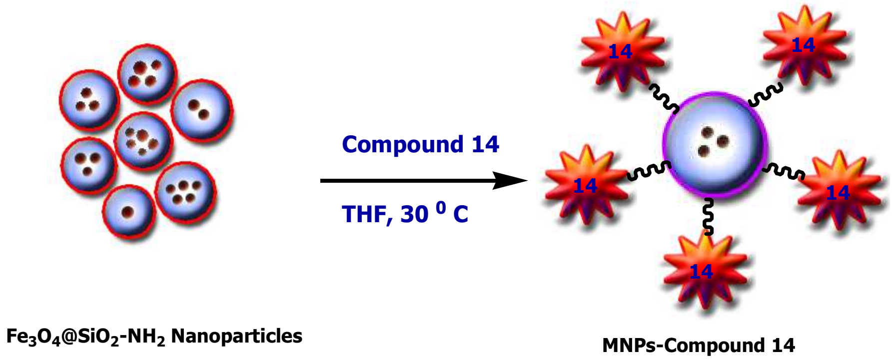

Figure 29: *Preparation of Fe_3O_4 @ SiO_2 – Compound 14*

Tetrahydrofuran was distilled to obtain the solvent in anhydrous form, and then THF was degassed with N_2 gas for 30 min. 20 mg of $Fe_3O_4@SiO_2-NH_2$ nanoparticles as a powder was added to 20 mL THF, and sonicated for 15 min. 1.5 mg of compound 14 was added to this dispersion and continued sonication for 15 min. This reaction mixture was allowed to proceed at 30 ^oC under nitrogen at dark for 2 days. To separate MNPs – Compound 14 from reaction medium, it was centrifuged at 6000 rpm for 10 min. It was washed with chloroform three times to remove any non-binding compound 14. The solid was dried under lyophilizer for 24 h to give black solid. The content of compound 14 in MNPs was estimated to be about 0.060 mg **BODIPY**/mg **MNPs** from the absorbance spectra of nonbinding compound 14.

2.3.7 Preparation of Fe_3O_4 @ SiO_2 – Compound 15

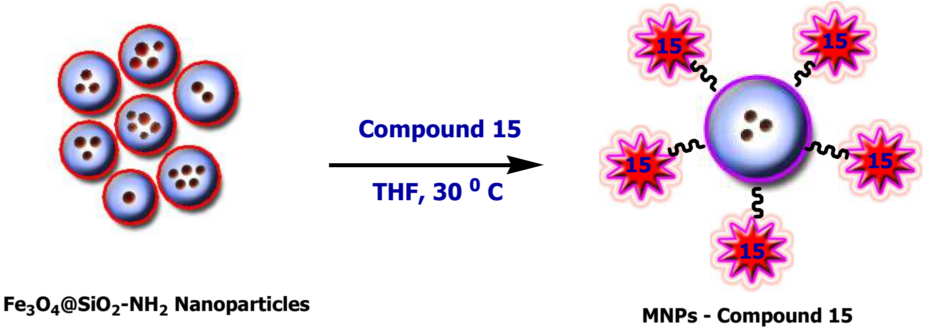

Figure 30: *Preparation of Fe_3O_4 @ SiO_2 – Compound 15*

Tetrahydrofuran was distilled to obtain the solvent in anhydrous form, and then THF was degassed with N_2 gas for 30 min. 20 mg of $Fe_3O_4@SiO_2$-NH_2 nanoparticles as a powder was added to 20 mL THF, and sonicated for 15 min. 1.1 mg of compound 15 was added to this dispersion and continued sonication for 15 min. This reaction mixture was allowed to proceed at 30 ^oC under nitrogen at dark for 2 days. To separate MNPs – Compound 15 from reaction medium, it was centrifuged at 6000 rpm for 10 min. It was washed with chloroform three times to remove any non-binding compound 15. The solid was dried under lyophilizer for 24 h to give black solid. The content of compound 15 in MNPs was estimated to be about 0.055 mg **BODIPY**/mg **MNPs** from the absorbance spectra of nonbinding compound 15.

2.3.8 Preparation of Fe_3O_4 @ SiO_2 – Compound 16

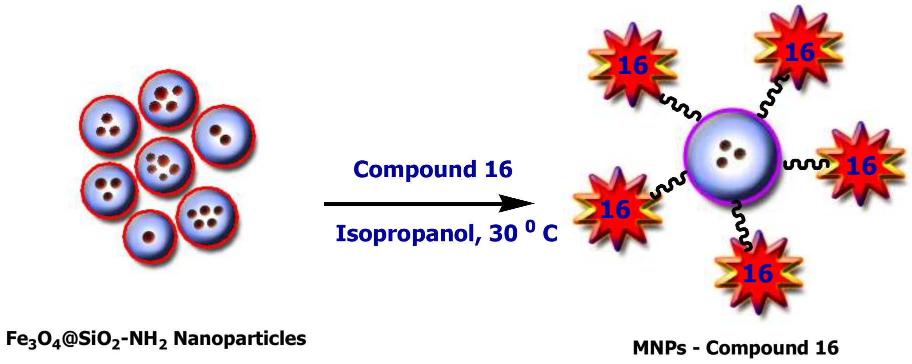

Figure 31: *Preparation of* Fe_3O_4 *@* SiO_2 *– Compound 16*

Isopropyl alcohol was degassed with N_2 gas for 30 min. 20 mg of Fe_3O_4@SiO_2-NH_2 nanoparticles as a powder was added to 20 mL isopropanol, and sonicated for 15 min. 1.0 mg of compound 16 was added to this dispersion and continued sonication for 15 min. This reaction mixture was allowed to proceed at 30 ^oC under nitrogen at dark for 2 days. To separate MNPs – Compound 16 from reaction medium, it was centrifuged at 6000 rpm for 10 min. It was washed with chloroform three times to remove any non-binding compound 16. The solid was dried under lyophilizer for 24 h to give light green solid. The content of compound 16 in MNPs was estimated to be about 0.050 mg **BODIPY**/mg **MNPs** from the absorbance spectra of nonbinding compound 16.

CHAPTER 3

RESULTS AND DISCUSSIONS

3.1 SPION Based Nanoplatforms for Imaging and Therapy

Colloidal MNPs have a wide range of interesting properties that make them practical for biological applications. They can be simply synthesized and functionalized, they are not expensive, they can be prepared colloidally stable, and they can be attached with biological molecules in a straightforward way. MNPs based on SPIONs offer lots of advantages for clinical purposes. Up to now, they have been utilized in humans for MRI imaging. In near future, they are likely to be also used for therapeutic issues[78]. Thus, in this study, SPIONs are synthesized as contrast agents. Then, they are coated with silica to provide colloidal and chemical stability. After coating the surface for silica, surface is functionalized with amine groups, which is needed for covalent modification of SPIONs with isothiocyanato terminated BODIPY derivatives.

Photodynamic therapy (PDT) has already been recognized as a noninvasive technique for cancer treatment and promising results are obtained in clinical applications. PDT gives minimal damage to healthy surrounding tissue, when compared to other therapies such as chemo or radiotherapies. One of the most important problems in clinical studies of PDT is related to penetration depth. Typical PSs are generally absorp lower wavelength of spectrum, where penetration is lower[9,10]. Therefore, we tried to synthesize four different BODIPY derivatives absorbing in near IR region. Singlet oxygen generation capabilities of these PSs are evaluated. In addition, since tracking of PSs in the body is very important in terms of clinics, we developed novel nanoplatforms that combine MRI imaging and PDT. Four this purpose, four different BODIPY based PSs are attached covalently to silica coated SPIONs. We did not use any targeting agent since even in the nonexistence of specific targeting group, PSs tend accumulate at tumor loci because of enhanced permeation and retention effect.

In this study, BODIPY is chosen because of its high extinction coefficient and high photostability. In addition, modification of core BODIPY is easy when compared to other PSs[46]. BODIPY core was synthesized through typical BODIPY reactions. In this research, 2,6 position of BODIPY core is decorated with bromines to increase spin-orbit coupling resulting efficacy in singlet oxygen production. Methyl groups in 3, 5 positions are acidic enough to participate in Knoevenagel condensation reactions. Via facile click reaction phenylic moiety possessing isothiocyanato group was linked to the BODIPY derivatives. Then, four different types synthesized PSs are attached to the amino modified SPIONs through the addition reaction between amino group and isothiocyanato.

All the PSs synthesized were characterized using ^{1}H, ^{13}C NMR spectra and Mass spectrometry analysis. NMR spectra were measured using $CDCl_3$ as solvent. All these data are given in appendices A and B.

3.2 Photophysical Measurements

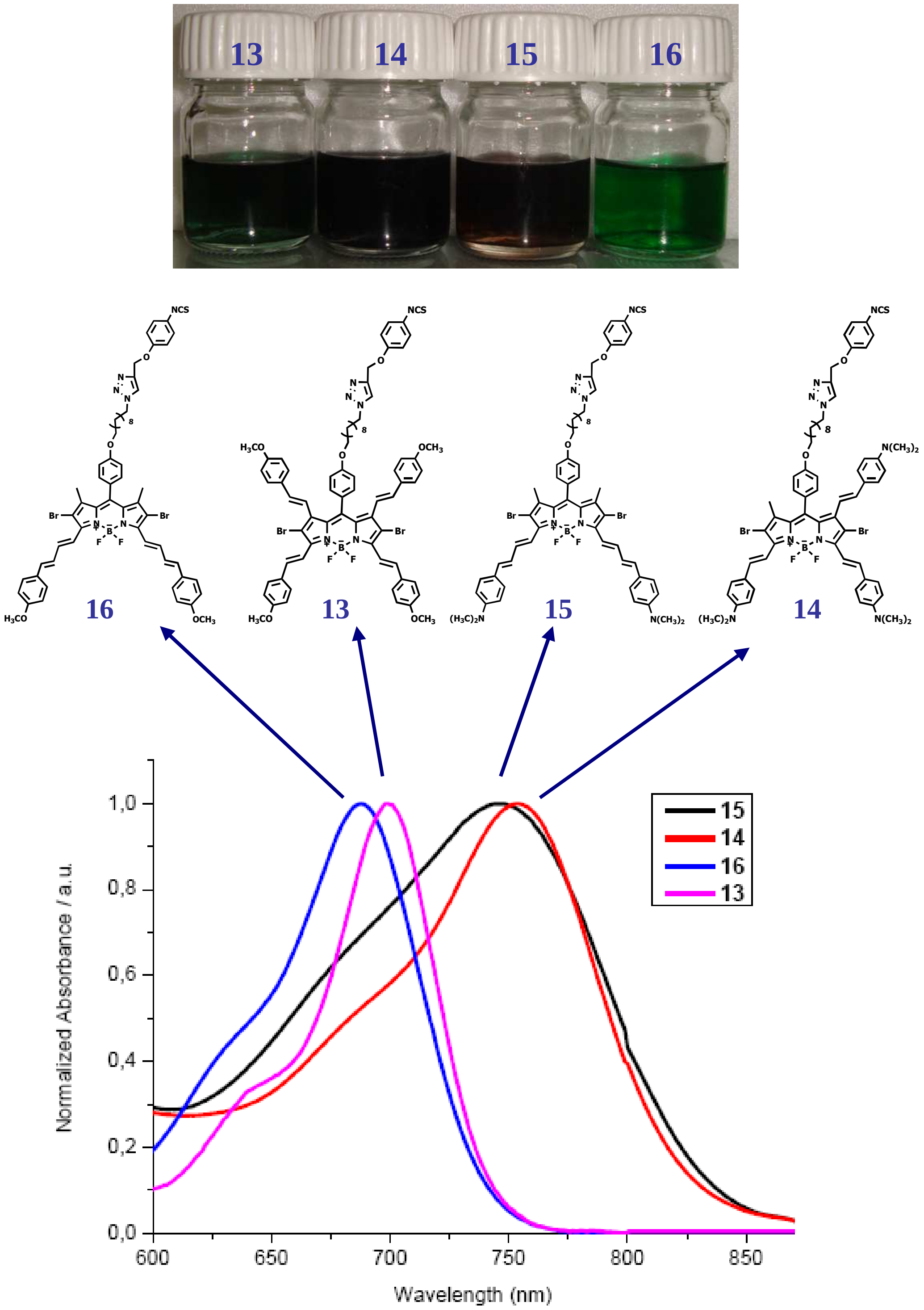

Figure 32. *Normalized absorbance spectra of the synthesized molecules* ***13, 14****,* ***15*** *and* ***16*** *in* $CHCl_3$.

Maximum absorbance wavelength of photosensitizers **13, 14, 15, and 16** is determined to be 698, 755, 746 and 689 nm, respectively (**Figure 32**). All wavelengths correspond to near IR region is very appropriate for PDT applications because penetration depth of light of this wavelength is considerably high.

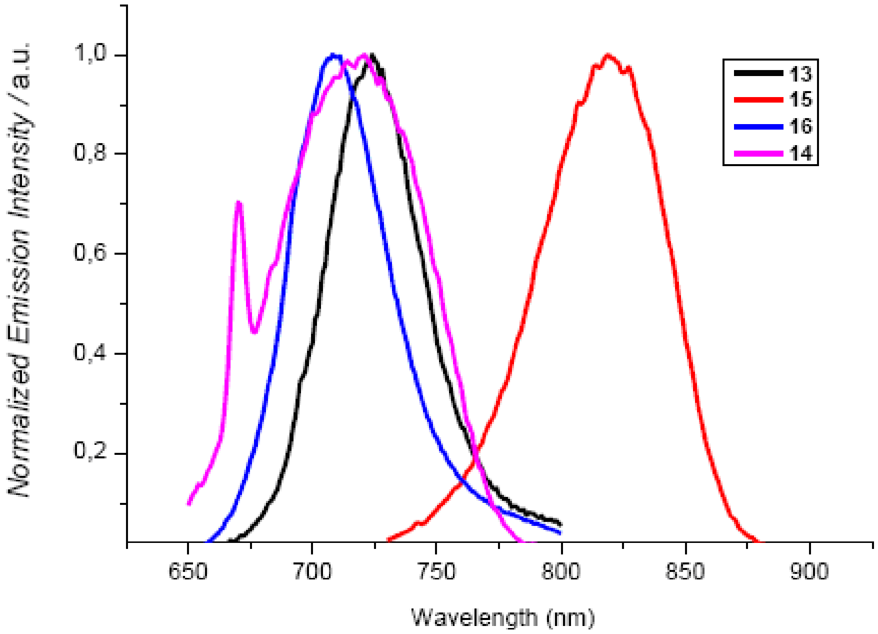

Figure 33. *Normalized emission spectra of the synthesized molecules* ***13***, ***14***, ***15*** *and* ***16*** *in* $CHCl_3$.

3.3 X-ray Diffraction (XRD) Analysis of Fe_3O_4 Nanoparticles

Spacing between adjacent lattice planes, d, was calculated by using Bragg's law. Experimental d spacing obtained from X-ray diffraction patterns are reported in Table 4 and was found similar to the ASTM data cards of the Fe_3O_4.[119] Based on the d spacing and the preparation method, it can be concluded that the iron oxide particles are mainly composed of the inverse cubic spinel structure of magnetite (Fe_3O_4).

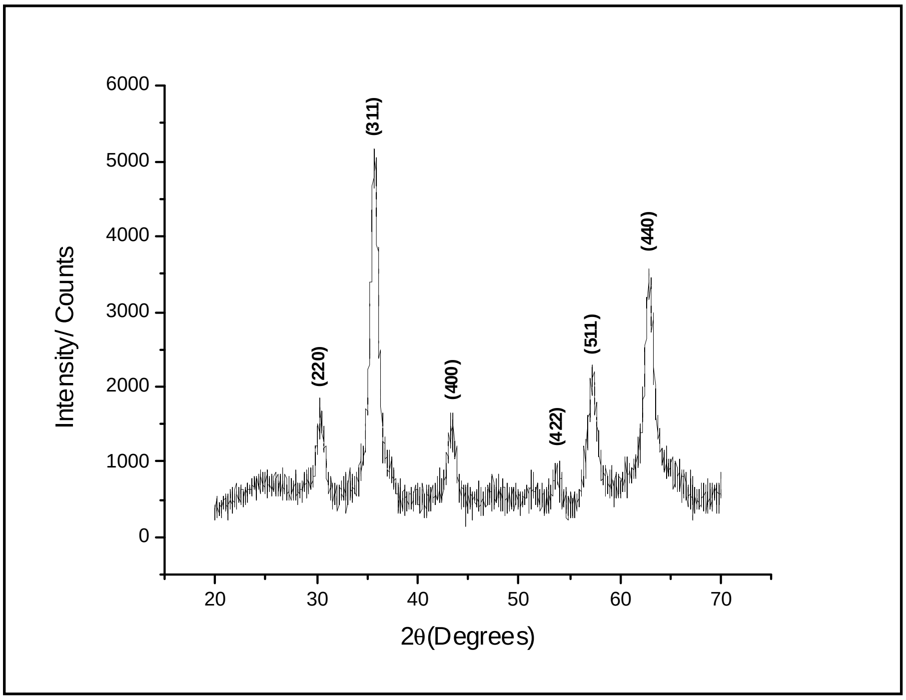

Figure 34. *XRD spectrum of the Fe_3O_4 nanoparticles, indicating the characteristic signals attributed to the crystal lattice of magnetite core.*

Table 4: *Summary data of experimental d (Å) spacings from X-ray patterns (d (exp.)) and from ASTM data cards for iron oxide (d (Fe_3O_4)*

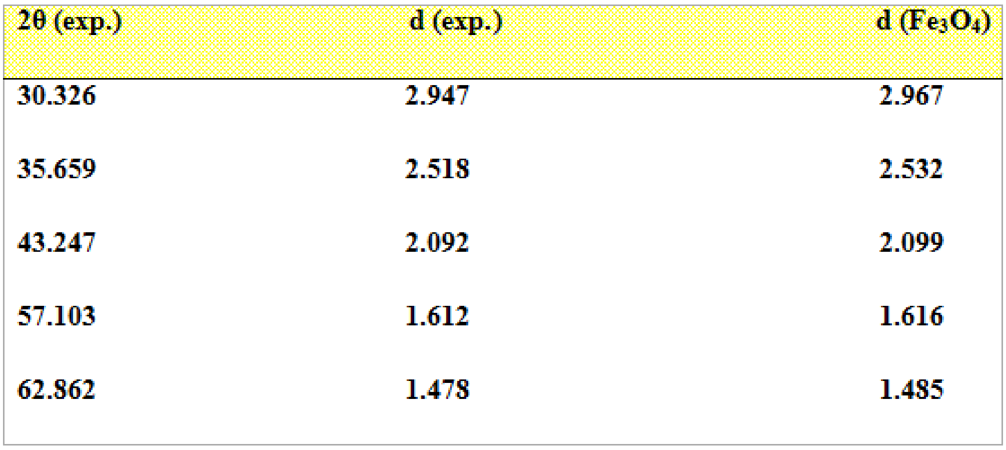

2θ (exp.)	d (exp.)	d (Fe_3O_4)
30.326	2.947	2.967
35.659	2.518	2.532
43.247	2.092	2.099
57.103	1.612	1.616
62.862	1.478	1.485

3.4 Transmission Electron Microscopy (TEM) Analysis

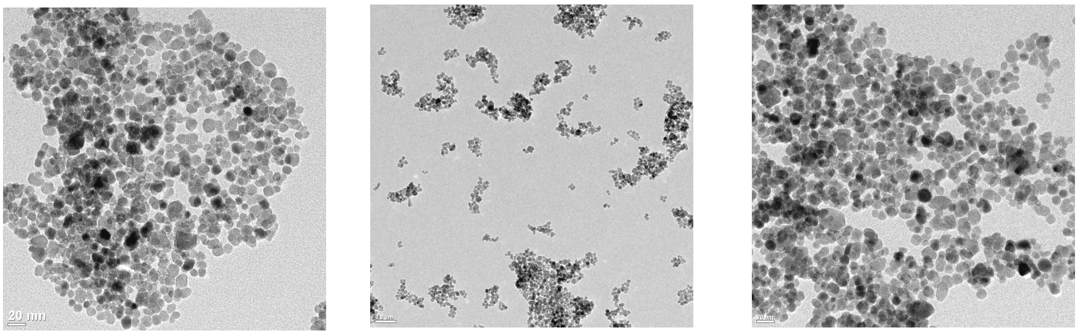

Figure 35. *TEM image of the synthesized* Fe_3O_4 *nanoparticles.*

The sample was prepared by mounting a drop of dilute magnetic dispersion on carbon coated copper grid and drying at room temperature. **Fig. 35** is TEM image of the synthesized Fe_3O_4 nanoparticles, which shows that most of the particles are quasi-spherical with a diameter ranging between of 5-10 nm. They have a tendency to aggregate because of magnetic dipole attractions.

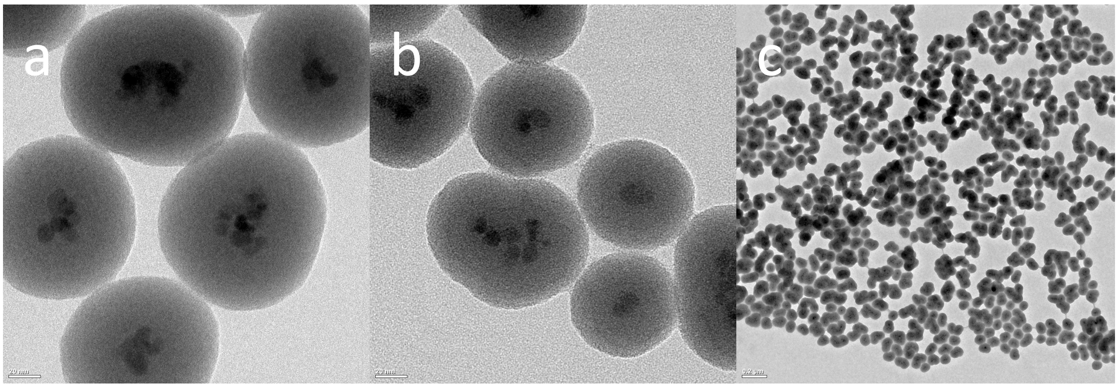

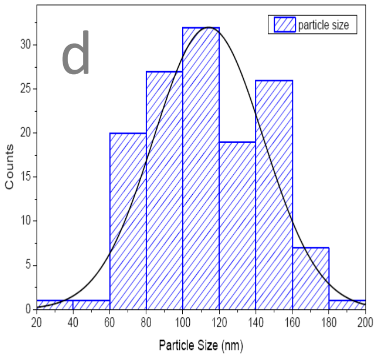

Figure 36. *TEM image of the synthesized* $Fe_3O_4@SiO_2$ *nanoparticles (a), (b), and (c). Histogram particle size distribution of* $Fe_3O_4@SiO_2$ *nanoparticles with an average diameter of 124.5± 40.1 nm (d). The TEM images confirm the spherical shape of the* $Fe_3O_4@SiO_2$ *(core/shell) structures of nanoparticles.*

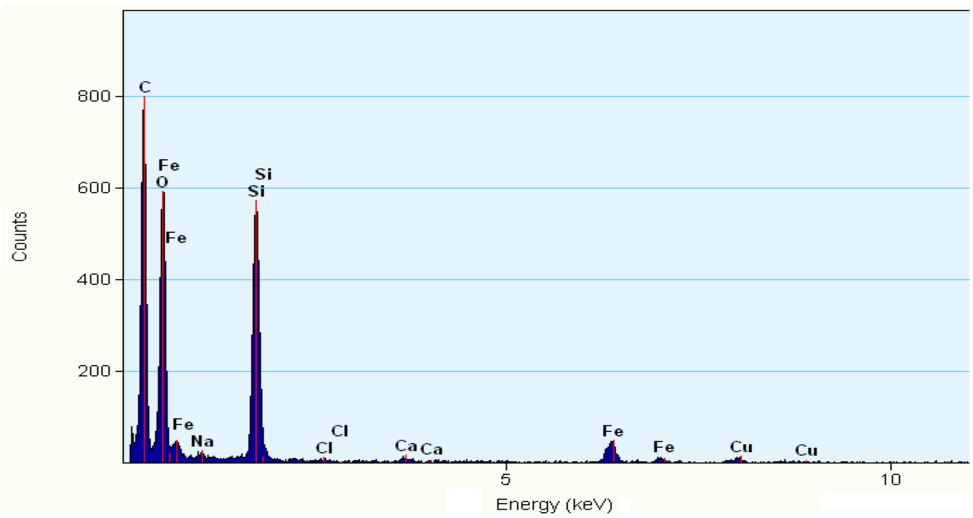

Figure 37. *Energy dispersive X-ray (EDX) emission spectra of Fe_3O_4@SiO_2 nanoparticles***.** *Strong Si peak and weak Fe peaks indicates the silica coating on magnetite nanoparticles.*

3.5 Vibrating Sample Magnetometer (VSM) Analysis of MNPs – Compound 13

Magnetic particles less than about 25 nm shows superparamagnetism.[120] Thus, the synthesized Fe_3O_4 nanoparticles are expected to exhibit superparamagnetism. To deduce the magnetic properties of magnetite nanoparticles after all modifications, the hysteresis loop of Fe_3O_4@SiO_2–Compound 13 nanoparticles was registered at room temperature and high field of 30 kOe using vibrating-sample magnetometer (**shown in Fig. 38**). The hysteresis loop demonstrated that there was no coercive force, thus featuring superparamagnetic behavior. The saturation magnetization of the Fe_3O_4@SiO_2–Compound 13 nanoparticles was determined to be 2.93 emu/g (2.68 emu/g at field of 10 kOe) which is reasonable when compared to other both citrate and silica coated superparamagnetic nanoparticles.[121]

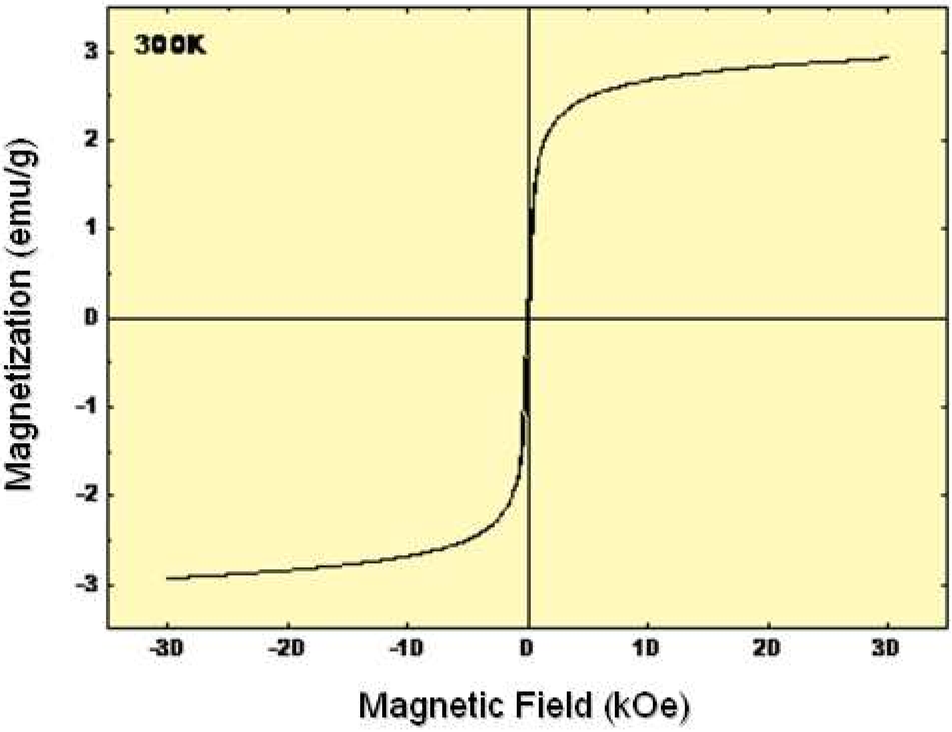

Figure 38. *VSM spectrum of the* $Fe_3O_4@SiO_2$*-Compound 13 nanoparticles at room temperature, revealing a superparamagnetic behaviour with no coercive force in the hysteresis loop.*

3.6 MNPs – Bodipy Dye 16 in Ethanol

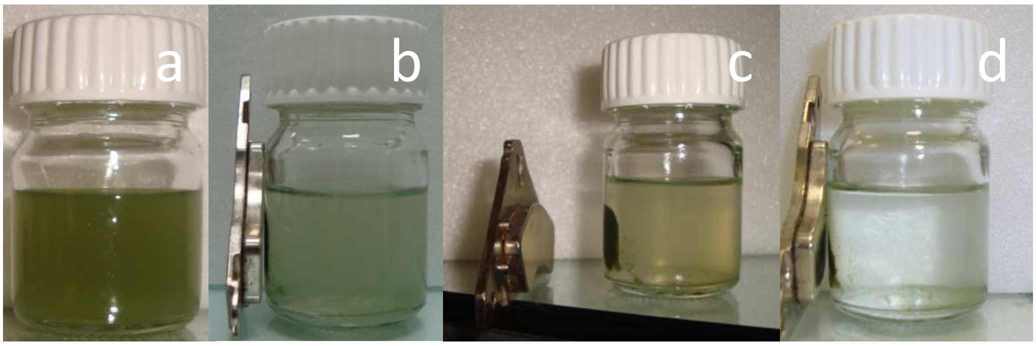

Figure 39. *(a) Dispersion of bodipy dye 16 attached magnetic nanoparticles in ethanol, (b) and (c) 3 min after dispersion under influence of magnetic field (by magnet), (d) 7 min after dispersion under influence of magnetic field, clearness in ethanol indicates the successful attachment of bodipy dye 16 to MNPs.*

3.7 X-ray Photoelectron Spectroscopy Surface Analysis for Amine Modification

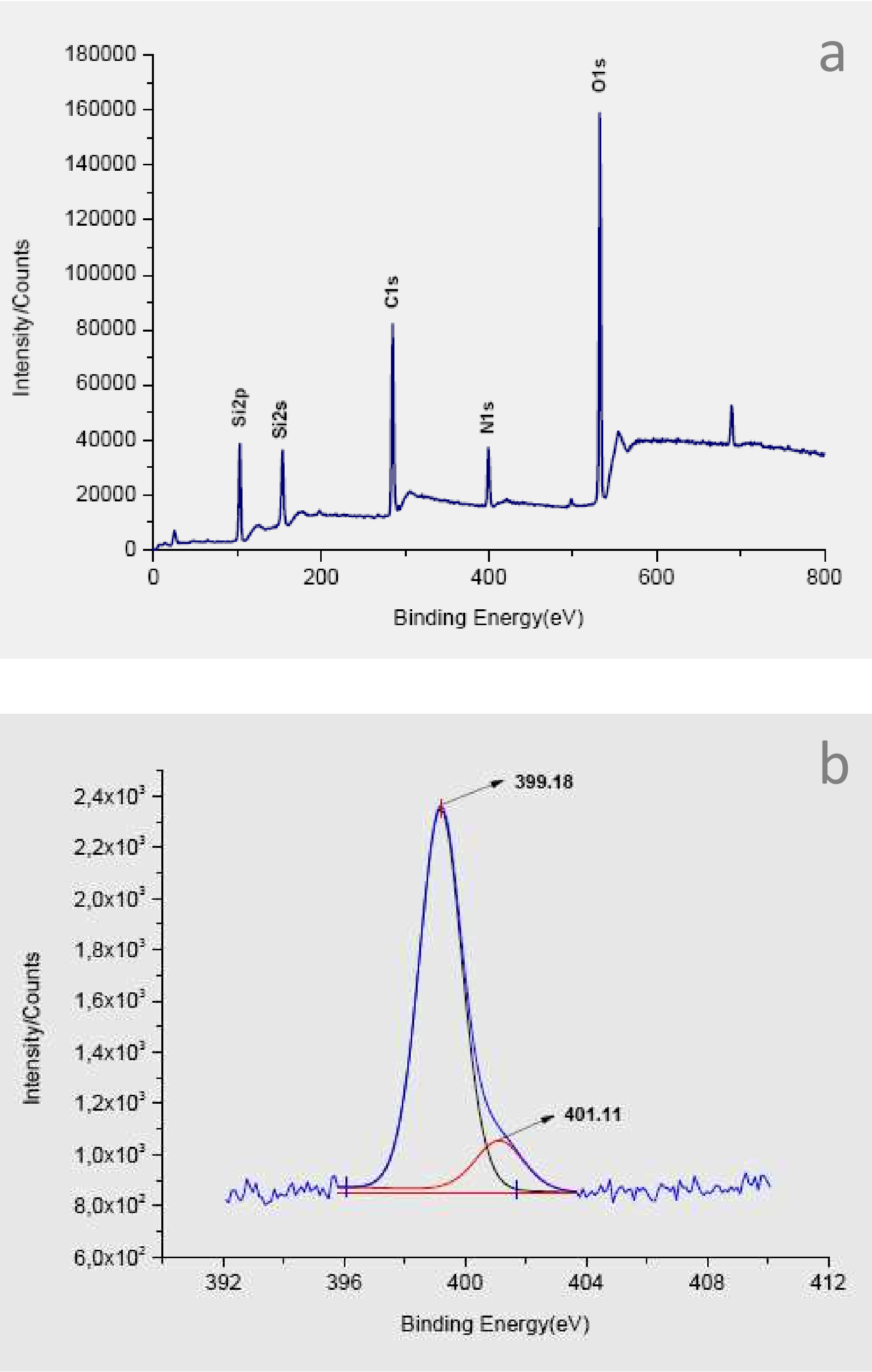

Figure 40. *X-ray photon spectroscopy (XPS) spectra of Fe_3O_4 @SiO_2–NH_2 nanoparticles presenting (a) a survey, and (b) N 1s spectra*

To prove the surface modification with APTES, X-ray photoelectron spectra was obtained. X- ray photoelectron spectroscopy (XPS) measurements were performed with Thermo Scientific, K-Alpha-Monochromated high-performance XPS spectrometer with monochromatic Al K Alpha source. Wide scan surveys and specific region (N 1s) were measured with a step size of 1.0 eV and 0.1 eV, respectively. XPS spectra were recorded in the CAE analyzer mode with a pass energy of 150 eV and 30 eV and an average of 2 and 30 scans, respectively. The typical survey spectrum of $Fe_3O_4@SiO_2–NH_2$ nanoparticles is presented in **Fig. 40a**. The peaks at binding energies 103.04 – 110.08, 285.18 – 290.58, 399.41 – 406.08, 532.34 – 538. 58 eV are ascribed to Si2p, C1s, N1s, O1s electrons. A penetration depth should be high enough[122] to detect iron in the underlying substrate; therefore, Fe2p3 and Fe3p electrons were not observed. The broad N1s peak which was deconvoluted into two spectral bands at 399.18, 401.11 eV in **Fig. 40b** is corresponding to the protonated and the unprotonated form present in APTES.[123]

3.8 Zeta Potential Measurements of MNPs

Characterization of ***$Fe_3O_4@SiO_2$-NH_2*** was conducted using zeta potential measurements at different pH values to determine the isoelectronic point (PI) of particles. The PI values can rise due to amine groups.[121] The high value of PI for the modified magnetic nanoparticles showed that amine functionalization was achived.

Zeta potential of **MNPs with compounds 13, 14, 15, and 16** was determined in PBS buffer at pH 7 as -15.7 mV, -11.6 mV, -25.4 mV, and -29.2 mV, respectively. Other information related with instrument is given in the experimental details.

**MNP: $Fe_3O_4@SiO_2$ Nanoparticle*

**AMNP: $Fe_3O_4@SiO_2$-NH_2 Nanoparticle*

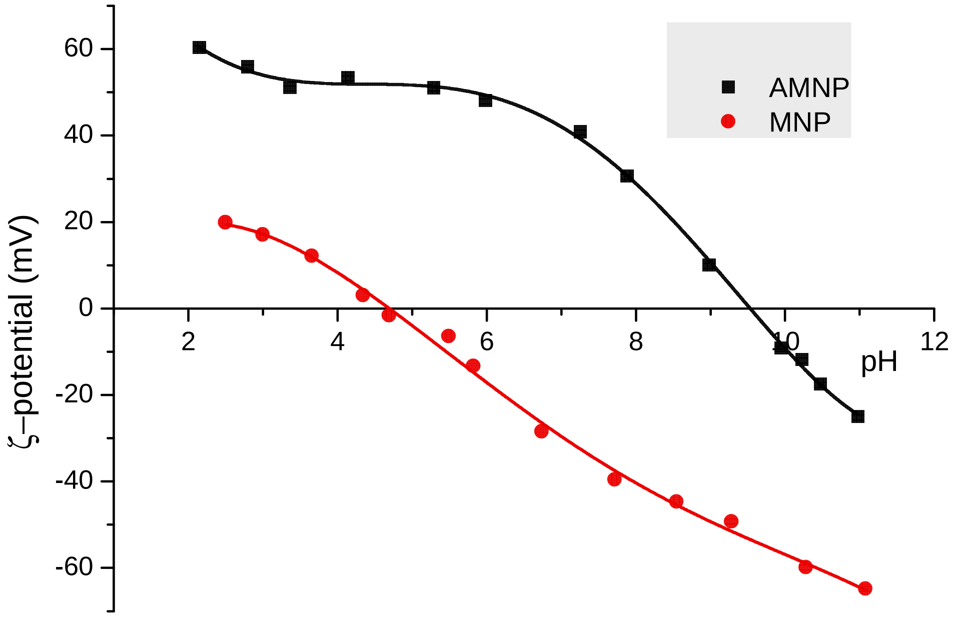

Figure 41. *Zeta potential of $Fe_3O_4@SiO_2$ and $Fe_3O_4@SiO_2$-NH_2 nanoparticles as a function of pH.*

3.9 Energy-Filtered Transmission Electron Microscopy (EFTEM) Images of MNPs – Compound 13

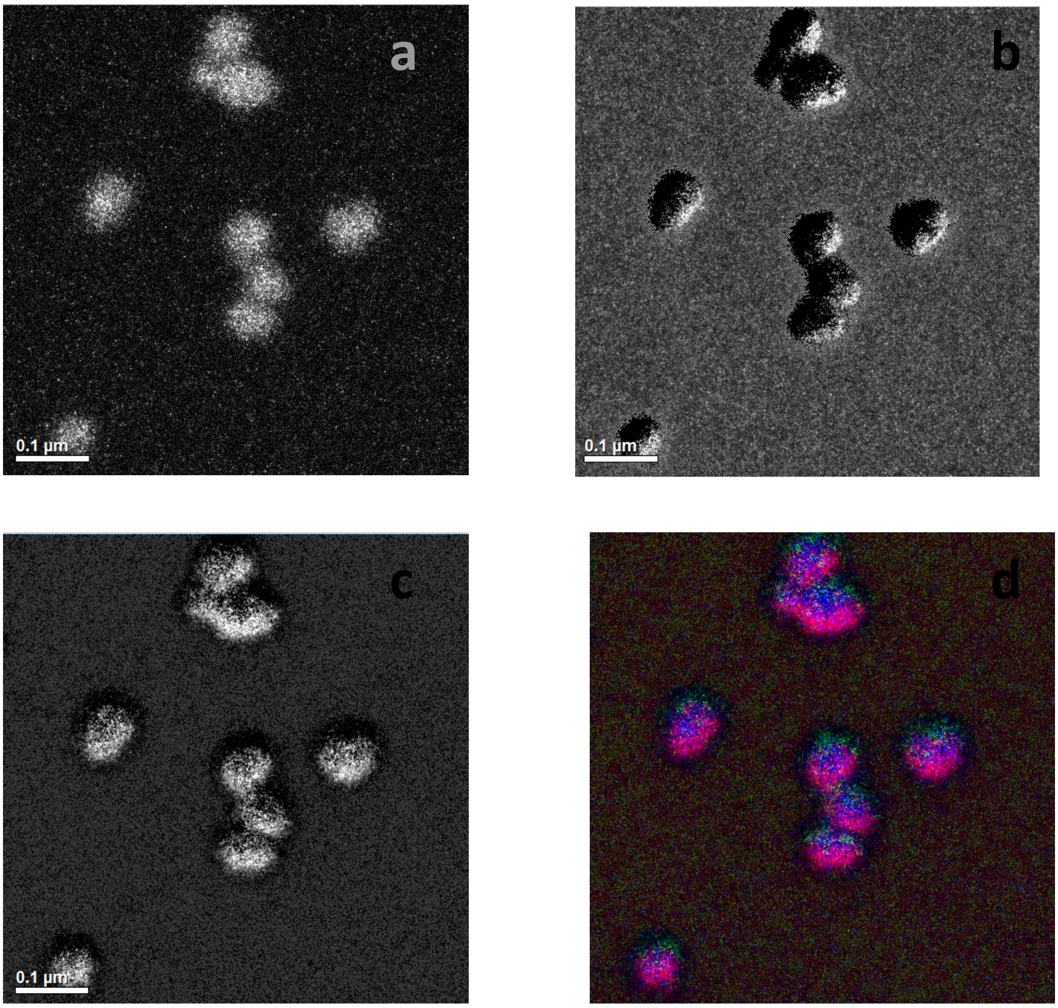

Figure 42. *Elemental maps in Fe_3O_4 @ SiO_2 – Compound 13 nanoparticles from EFTEM images: (a) Boron map, (b) Bromine map, (c) Silicon map, (d) The RGB image created by superimposing the elemental EFTEM maps of B (green), Br (blue), and Si (pink).*

3.10 Singlet Oxygen Generation Experiments

Singlet oxygen generating capability of compound 13, 14, 15, and 16 was done using singlet oxygen trap molecule 1,3-diphenylisobenzofuran (DPBF) in dichloromethane. Singlet oxygen generating experiments for Fe3O4@SiO2 – Compound 13, 14, 15, 16 was conducted using singlet oxygen trap (DPBF) in isopropyl alcohol. Air saturated DCM and isopropanol was obtained by bubbling air for 15 minutes. Singlet oxygen can be monitored using photobleaching and subsequent decrease in absorbance of DPBF as shown in Figure 43.

The absorbance of DPBF was adjusted around 1.0 in air saturated dichloromethane and isopropanol. Then, the photosensitizer was added to cuvette and photosentizer's absorbance was adjusted around 0.2-0.3. After, taking some measurements in dark, we exposed the cuvette to 725 nm emitting 3000 mCd lead light source for different time intervals for each solution. 725 nm light was exposed from 12 cm cell distance for each solution containing compound 13, 14, 15, 16 and 4 cm cell distance for each solution containing Fe_3O_4@SiO_2 – Compound 13, 14, 15, 16 and bare magnetic nanoparticles.

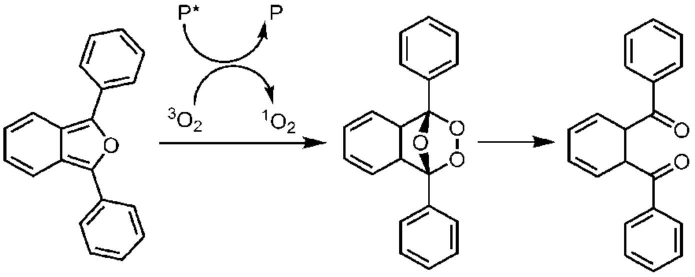

Figure 43. *Photobleaching of DPBF*

Control solution was prepared with bare nanoparticles (Fe_3O_4@SiO_2 nanoparticles without any attached bodipy derivatives). Absorbance was measured for several times after each irradiation. The graphics recorded are shown below; Figures 44 to 52. Compound 13 is the best singlet oxygen generator among the compounds 14, 15, and 16.

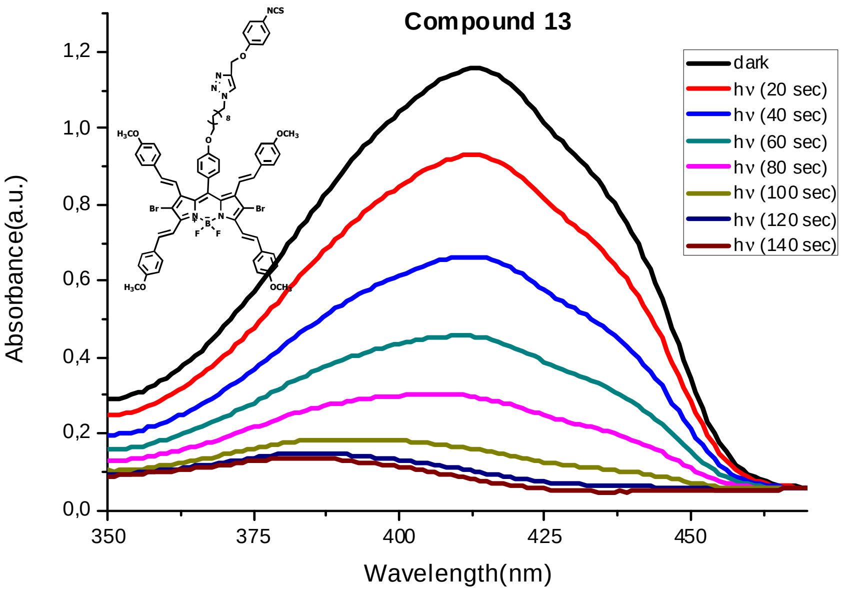

Figure 44. *Decrease in absorbance spectrum of trap molecule DBPF in the presence of 3.87 µM compound 13 in dichloromethane. Details are given in singlet oxygen measurements part.*

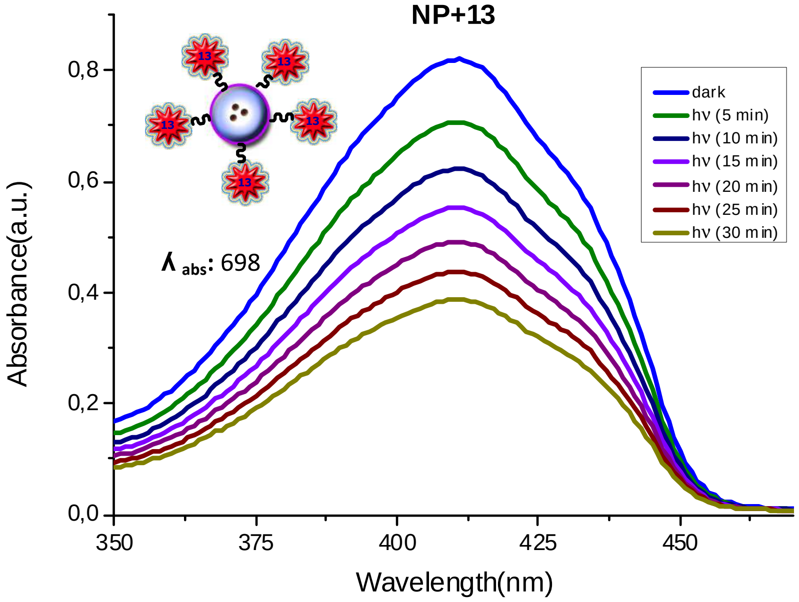

Figure 45. *Decrease in absorbance spectrum of trap molecule DBPF in the presence of 7.46 µM compound 13 attached to* $Fe_3O_4@SiO_2$ *in isopropyl alcohol. Details are given in singlet oxygen measurements part.*

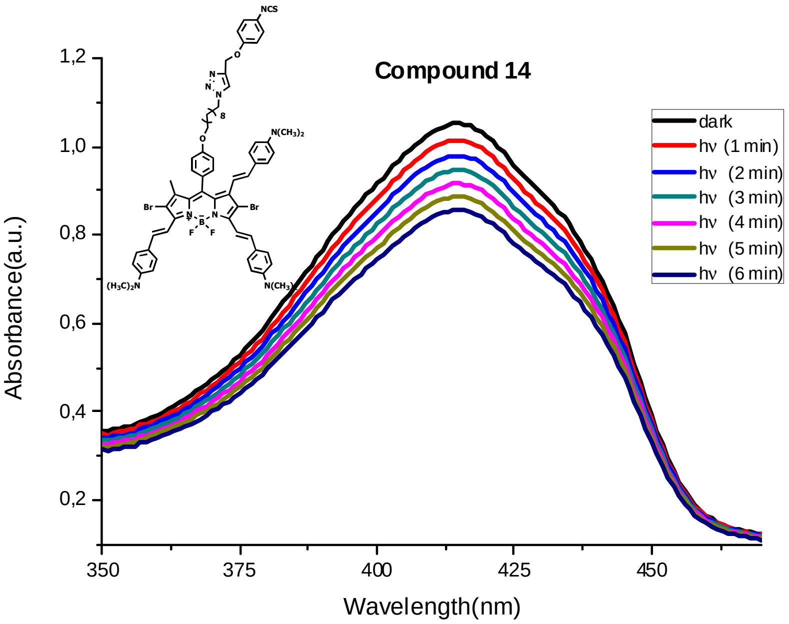

Figure 46. *Decrease in absorbance spectrum of trap molecule DBPF in the presence of 4.59 µM compound 14 in dichloromethane. Details are given in singlet oxygen measurements part.*

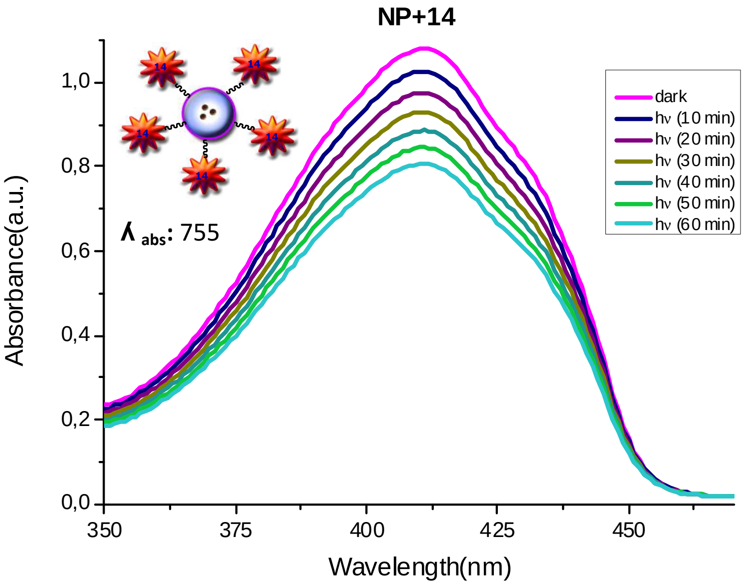

Figure 47. *Decrease in absorbance spectrum of trap molecule DBPF in the presence of 8.71 µM compound 14 attached to $Fe_3O_4@SiO_2$ in isopropyl alcohol. Details are given in singlet oxygen measurements part.*

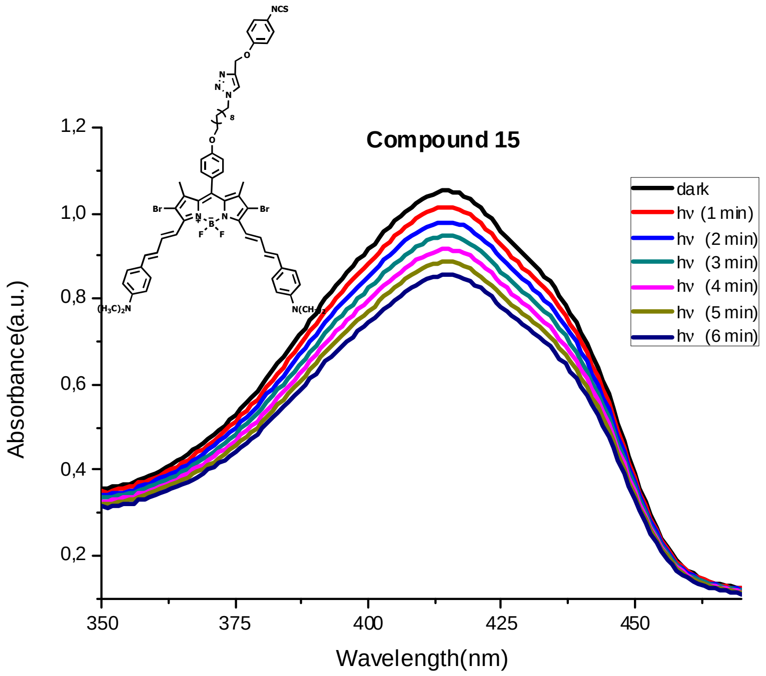

Figure 48. *Decrease in absorbance spectrum of trap molecule DBPF in the presence of 4.81 µM compound 15 in dichloromethane. Details are given in singlet oxygen measurements part.*

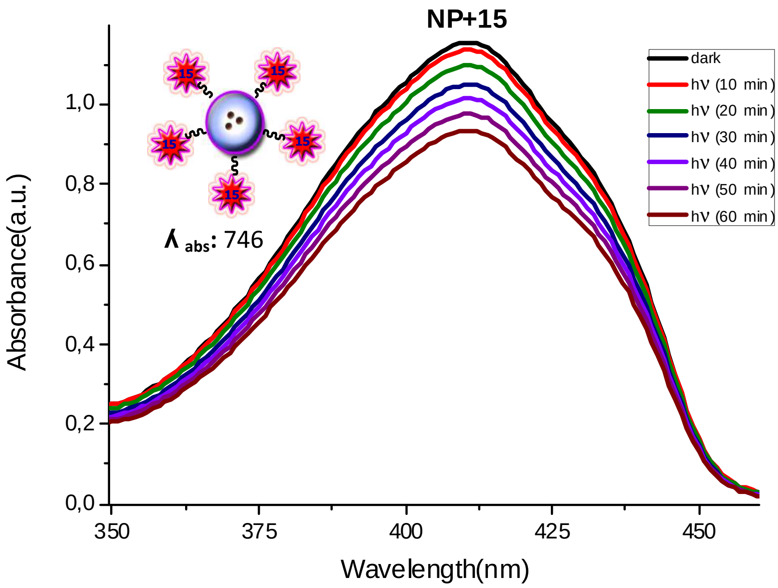

Figure 49. *Decrease in absorbance spectrum of trap molecule DBPF in the presence of 12.6 µM compound 15 attached to Fe_3O_4@SiO_2 in isopropyl alcohol. Details are given in singlet oxygen measurements part.*

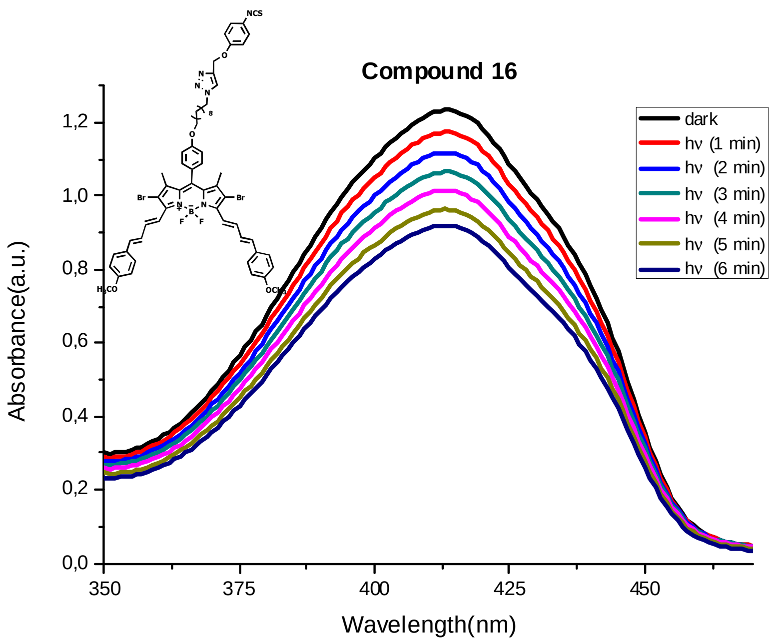

Figure 50. *Decrease in absorbance spectrum of trap molecule DBPF in the presence of 3.37 µM compound 16 in dichloromethane. Details are given in singlet oxygen measurements part.*

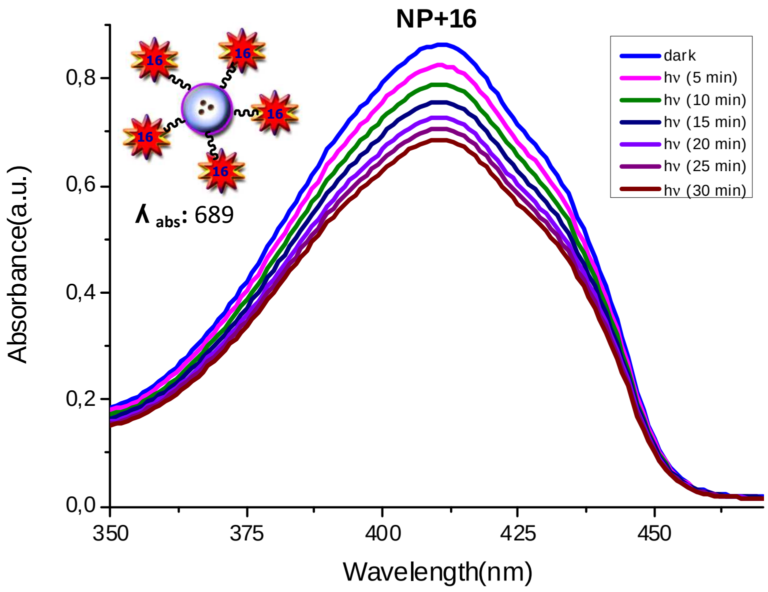

Figure 51. *Decrease in absorbance spectrum of trap molecule DBPF in the presence of 8.66 µM compound 16 attached to* Fe_3O_4*@*SiO_2 *in isopropyl alcohol. Details are given in singlet oxygen measurements part.*

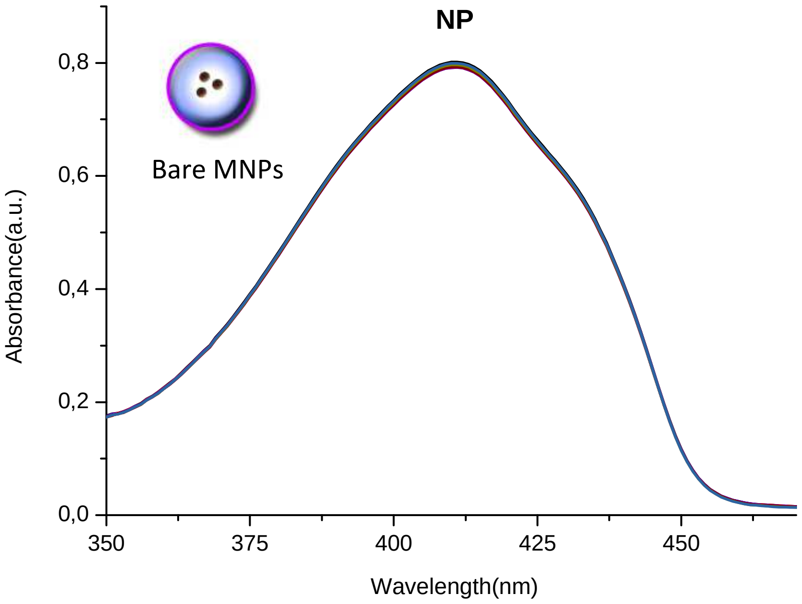

Figure 52. *Control singlet oxygen generation experiment. There is no decrease in absorbance spectrum of trap molecule DBPF in the presence of 0.03 mg* $Fe_3O_4@SiO_2$ *nanoparticle in 1.3 ml isopropyl alcohol after six times light irradiation with 1 min interval. Details are given in singlet oxygen measurements part.*

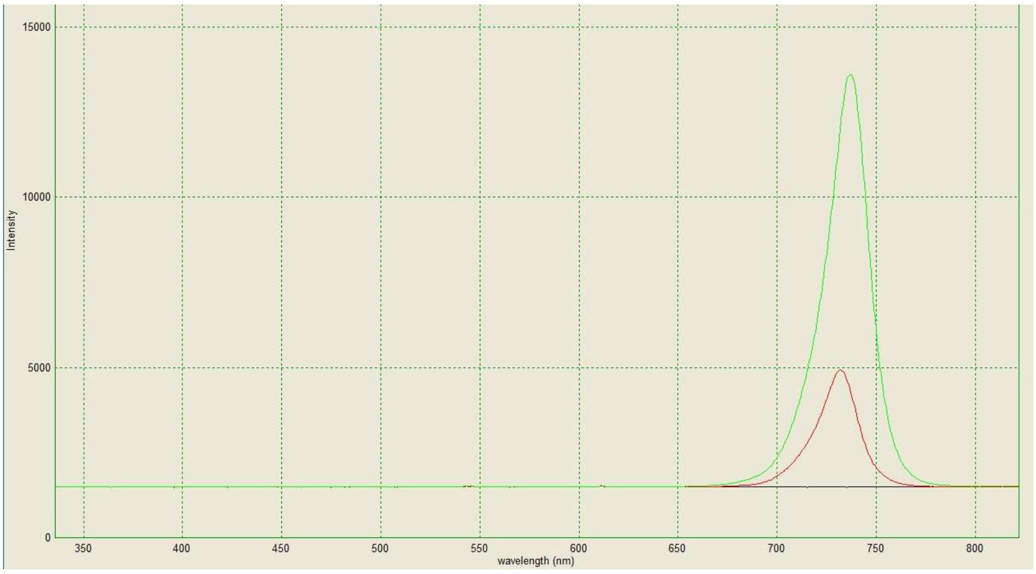

Figure 53. *Snapshot of 725 nm emitting 3000 mCd lead light source taken Overture software by Ocean Optics.*

CHAPTER 4

CONCLUSION

In this research, four different types of BODIPY-based photodynamic therapy agents synthesized and characterized by various characterization techniques. These PSs were then covalently attached to MRI active, biocompatible and nontoxic silica coated SPIONs. By this way, a multidisciplinary approach was followed to create novel theranostic nanoparticles for both MRI imaging and photodynamic therapy. Although we did not conduct in *vivo* studies for SPIONs, it is well known that iron oxide nanoparticles show great potential for clinical applications due to their high biocompatibility. In addition, besides being a MRI contrast reagent, iron oxide NPs show therapeutic termal effect (hyperthermia) under influence of magnetic field. Moreover, by the application of an external magnetic field gradient, these novel drug carrier nano platforms can be targeted directly to tumor loci. Therefore, further research is needed to improve these therapeutic nanoplatforms for clinical applications.

Physical properties of nanoparticles are characterized well using TEM, EDAX, XRD, XPS, Zeta sizer, and magnetometry. Generation of singlet oxygen capabilities are followed by absorbance spectrum. Singlet oxygen generation experiments show that all the compounds 13, 14, 15, 16 are an effective singlet oxygen generator in micro molar concentrations upon irradiation with LED. Moreover, they still preserve their ability to generate singlet oxygen after attachment to the nanoparticles. Therefore, it is shown that these modified core-shell nanoparticles shows potential as a delivery vehicles of PSs for the use in diagnosis and therapy.

REFERENCES

1. Hopper, C. Lancet Oncol. , 2000, 1, 212.

2. Konan, Y.N.; Gurny, R.; Alle´mann, E. Photochem. Photobiol. B: Biology 66, 2002, 89

3. Levy, G.; Obochi, M. Photochem. Photobiol., 1996, 64, 737

4. Kubler, A.C. Med. Laser Appl., 2005, 20, 37.

5. Mitra, A.; Stables, G.I. Photodiag. Photodyn. Ther., 2006, 3, 116

6. Schuitmaker, ; Bass, P.; Van Leengoed, H.L.L.M.; Van Der Meulen, F.W.; Star, W.M.; Zandwijk, N. Photochem. Photobiol.: B. Biol., 1996, 34, 3.

7. Castano, A.P.; Demidova, T.N.; Hamblin, M.R. Photodiag. Photodyn. Ther., 2005, 2, 1.

8. Agostinis, P.; Berg, K.; Cengel, K.A.; Foster, T.H.; Girotti, A.W., Gollnick, S.O.; Hahn, S.M.; Hamblin, M.R.; Juzeniene, A.; Kessel, D.; Korbelik, M.; Moan, ; Mroz, P.; Nowis, D.; Piette, ; Wilson, B.C.; Golab, CA Cancer J Clin., 2011, 61, 250.

9. Lovell, F.; Liu.B, T.W.; Chen, ; Zheng, G. Chem. Rev. 2010, 110, 2839.

10. Castano, A.P.; Demidova, T.N.; Hamblin. Photodiag. Photodyn. Ther., 2004, 1, 279.

11. Juzeniene, A.; Moan, Photodiag. Photodyn. Ther., 2007, 4, 3.

12. Robertson, C.A.; Evans, D.H.; Abrahamse, H. Photochem. Photobiol. B: Biology, 2009, 96, 1.

13. Ochsner, M. Photochem. Photobiol.: B. Biol., 1996, 32, 3.

14. Bilski, P.; Motten, A. G.; Bilska, M.; Chignell, C.F. Photochem Photobiol. 1993, 58, 8.

15. Ma J, Jiang L. Free Radic Res, 2001, 35, 767.

16. Foote CS. Science, 1968, 162, 963.

17. Plaetzer, K.; Krammer, B.; Berlanda, ; Berr, F.; Kiesslich, T. Laser. Med. Sci. 2008, 1, 1.

18. Detty, M.R.; Gibson, S.L.; Wagner, S. Journal of Medicinal Chemistry, 2004, 47, 16.

19. Allison R.R.; Downie G.H.; Cuenca, R.; Hu, X.H.; Childs, C.; Sibata, C.H. Photodiag. Photodynam.Ther. 2004, 1, 27.

20. Sharman, W. M.; Allen, C. M.; Van Lier, E. Drug Discovery Today 1999, 4, 507.

21. Juzeniene, A.; Nielsen, K.P.; Moan, Environ Pathol Toxicol Oncol., 2006, 25, 7.

22. Gorman, A.; Killoran, ; O'Shea, C.; Kenna, T.; Gallagher, M. W.; O'Shea, D. F. J. Am. Chem. Soc., 2004, 126, 10619.

23. Turro, N. In Modern Molecular Photochemistry; University Science Books: Sausalito, CA, 1991, 191.

24. Lower, S.K.; El-Sayed, M.A. Chem. Rev., 1966, 66, 199.

25. Svaasand, LO. Prog Clin Biol Res 1984, 170, 91.

26. Wilson, B.C.; Jeeves, W.P.; Lowe, D.M. Photochem Photobiol, 1985, 42, 153.

27. Henderson, B.W.; Busch, T.M.; Snyder, W. Lasers Surg Med., 2006, 38, 489.

28. Brancaleon, L.; Moseley, H. Lasers Med Sci., 2002, 17, 173.,

29. Szeimies, R.M.; Morton, C.A.; Sidoroff, A.; Braathen, L.R. Acta Derm Venereol, 2005, 85, 483.

30. Wilson, B.C.; Patterson, M.S. Phys Med Biol., 2008, 53, R61.

31. Lukšienė, Ž.MEDICINA, 2003, 39 tomas, Nr. 12.

32. Kalka, K.; Merk, H.; Mukhtar, H. J Am Acad Dermatol, 2000, 42(3), 389.

33. Roland, C.L.; Harken, A.H.; Sarr, M.G.; Barnett, C.C. Surg., 2007, 141, 705.

34. Buytaert, E.; Dewaele, M.; Agostinis, P. Biochem. Biophys. Acta, 2007, 1776, 86.

35. Davids, L.M.; Kleemann, B.; Kacerovska, D.; Pizinger, K.; Kidson, S.H. Photochem. Photobiol.: B. Biol., 2008, 91, 67.

36. Pazos, M:D:C.; Nader, H.B. Braz. Med. Biol. Res., 2007, 40, 1025.

37. Nowis, D.; Stoklosa, T.; Legat, M.; Issat, T.; Jakobisiak, M.; Golab, Photodiag. Photodyn. Ther., 2005, 2, 283.

38. Wieman T.; Fingar, V.H. SPIE Conf Proc, 1989, 106, 11.

39. M.P. Zhen-hui Peng, M.P.; Xiao, S.; Ren, ; Liu, Y.; Li, X.; Li, Z., Nanjing Med. Univ., 2008, 22, 18.

40. Berg, K.; Bommer, C.; Moan, Cancer Letters, 1989, 44, 7.

41. Jori, G.; Beltramini, M.; Reddi, E.; Salvato, B.; Pagnan, A.; Ziron, L. Cancer Letters, 1984, 26, 291.

42. Kessel, D.; Thompson, P.; Saatio, K.; Nanturi, K.D.Photochem Photobiol, 1987, 45, 787.

43. Huang, Z. Technol Cancer Res Treat., 2005, 4(3), 283.

44. Moser, JG. Definitions and General Properties of 2nd & 3rd Generation Photosensitizers. In: Moser, JG., editor. Photodynamic Tumor Therapy-2nd & 3rd Generation Photosensitizers. Harwood Academic Publishers; London: 1997. p. 3-8.

45. Berenbaum, M.C., Chevretton, E.B. Lasers Med Sci, 1993, 8, 235.

46. Loudet, A.; Burgess, K. Chem. Rev., 2007, 107, 4891.

47. Atilgan, S.; Ekmekci, Z.; Dogan, A. L.; Guc, D.; Akkaya, E. U. Chem. Commun., 2006, 4398.

48. Kral, V.; Davis, ; Andrievsky, A. J Med Chem. 2002, 45, 1073.

49. Szeimies, R.M.; Karrer, S.; Abels, C. J Photochem Photobiol B, 1996, 34, 67.

50. Bellnier, D. A.; Greco, W. R.; Loewen, G. M.; Nava, H.; Oseroff, A. R.; Pandey, R. K.; Tsuchida, T.; Dougherty, T. Cancer Res., 2003, 63, 1806.

51. Kato, Photochem. Photobiol., B. 1998, 42, 96.

52. Jichlinski, P.; Leisinger, H.- Urol. Res. 2001, 29, 396.

53. Moesta, K. T.; Schlag, P.; Douglas, H. O., Jr.; Mang, T. S. Lasers Surg. Med., 1995, 16, 84.

54. Nathan, T. R.; Whitelaw, D. E.; Chang, S. C.; Lees, W. R.; Ripley, P. M.; Payne, H.; Jones, L.; Parkinson, M. C.; Emberton, M.; Gilliam, A. R.; Mundy, A. R.; Bown, S. G. Urol., 2002, 168, 1427.

55. Baas, P.; Saarnak, A.; Oppelaar, H.; Neering, H.; Stewart, F. A. Br. Dermatol., 2001, 145, 75.

56. Loman, A.; Morton, C. A. Expert Opin. Biol. Ther. 2002, 2, 45.

57. Rechtman, E.; Ciulla, T. A.; Criswell, M. H.; Pollack, A.; Harris, A. Expert Opin. Pharmacother. 2002, 3, 931.

58. Wainwright, M. Antimicrob. Agents, 2003, 21, 510.

59. Wilson BC. Photonic and non-photonic based nanoparticles in cancer imaging and therapeutics. In: Dubowski J, Tanev S, eds. Photon-Based Nanoscience and Nanobiotechnology. Dordrecht, the Netherlands: Springer; 2006, 121.

60. Richter A.M.; Waterfield, E.; Jain, A.K.; Canaan, A.; Allison, B.A.; Levy, G. Photochem Photobiol., 1993, 57, 1000.

61. Chatterjee, D.K.; Fong, L.S.; Zhang, Y. Adv Drug Deliv Rev. 2008, 60, 1627.

62. Rai, P.; Chang, S.K.; Mai, Z.; Neuman, D.; Hasan, T. Proc SPIE., 2009, 7380, 73801.

63. Chen, ; Stefflova, K.; Niedre, M.J Am Chem Soc., 2004, 126, 11450.

64. Zheng, G.; Chen, ; Stefflova, K.; Jarvi, M.; Li, H.; Wilson, B.C. Proc Natl Acad Sci U S A. 2007, 104, 8989.

65. Ozlem S.; Akkaya E. U. J. Am. Chem. Soc., 2009, 131, 48.

66. Starkey, R.; Rebane, A.K.; Drobizhev, M.A. Clin Cancer Res., 2008, 14, 6564.

67. Collins, H.A.; Khurana, M.; Moriyama, E.H. Nature Photonics., 2008, 2, 420.

68. Brown, S.B.; Brown, E.A.; Walker, I. Lancet Oncol., 2004, 5, 497.

69. Koo, Y. E.; Reddy, G. R.; Bhojani, M.; Schneider, R.; Philbert, M. A.; Rehemtulla, A.; Ross, B. D.; Kopelman, R. Adv. Drug Delivery Rev., 2006, 58 (14), 1556.

70. Bhojani, M. S.; Reddy, G. R.; Koo, Y.; Philbert, M.; Kopelman, R.; Rehemtulla, A.; Ross, B. D. Multifunctional nanoparticles for targeted imaging and therapy. In Cancer Nanotechnology; Nalwa, H. S., Wester, T. , Eds., American Scientific Publishers., 2007, 81.

71. Moghimi, S. M.; Hunter, A. C.; Murray, C. FASEB J,. 2005, 19 (3), 311.

72. Gao, X.; Cui, Y.; Levenson, R.M.; Chung, L.W.K.; Nie, S. Nat. Biotechnol., 2004, 22, 969.

73. Lodhia, Biomed Imaging Interv J, 2010, 6(2), e12

74. Ferrari, M. Nat. Rev. Cancer, 2005, 5, 161.

75. De, M.; Ghosh, P.S.; Rotello, V.M. Adv. Mater., 2008, 20, 4225.

76. Kelkar, S.S.; Reineke, T.M. Bioconjugate Chem., 2011, 22, 1879.

77. Bhojani, M.S.; Van Dort, M.; Rehemtulla, A.; Ross, B.D. Moleculer Pharmaceutics., 2010, 7 (6), 1921.

78. Sonvico, F.; Mornet, S.; Vasseur, S.; Dubernet, C.; Jaillard, D.; Degrouard, ; Hoebeke, ; Duguet, E.; Colombo, P.; Couvreur, P. Bioconjugate Chem., 2005, 16 (5), 1181.

79. Liong, M.; Lu, ; Kovochich, M.; Xia, T.; Ruehm, S. G.; Nel, A. E.; Tamanoi, F.; Zink, I. ACS Nano, 2008, 2 (5), 889.

80. Medarova, Z.; Kumar, M.; Ng, S. W.; Yang, ; Barteneva, N.; Evgenov, N. V.; Petkova, V.; Moore, A. Transplantation, 2008, 86 (9), 1170.

81. Kumar, A.; Jena, P. K.; Behera, S.; Lockey, R. F.; Mohapatra, S.; Mohapatra, S. Nanomedicine, 2010, 6 (1), 64.

82. McCarthy, R.; Weissleder, R. Adv Drug Delivery Rev 2008, 60 (11), 1241.

83. Blanco, E.; Kessinger, C. W.; Sumer, B. D.; Gao, Exp. Biol. Med. (Maywood) 2009, 234 (2), 123.

84. Guo, R.; Zhang, L.; Qian, H.; Li, R.; Jiang, X.; Liu, B. Langmuir , 26 (8), 5428.

85. Bhaskar, S.; Tian, F.; Stoeger, T.; Kreyling, W.; de la Fuente, M.; Grazu, V.; Borm, P.; Estrada, G.; Ntziachristos, V.; Razansky, D. Part. Fibre Toxicol., 2010, 7, 3.

86. Gindy, M. E.; Prud’homme, R. K. Expert Opin. Drug Delivery 2009, 6 (8), 865.

87. Masotti, A. Recent Pat. Nanotechnol., 2010, 4 (1), 53.

88. O'Brien, M. E.; Wigler, N.; Inbar, M.; Rosso, R.; Grischke, E.; Santoro, A.; Catane, R.; Kieback, D. G.; Tomczak, P.; Ackland, S. P.; Orlandi, F.; Mellars, L.; Alland, L.; Tendler, C. Ann Oncol., 2004, 15 (3), 440.

89. Chen, W.; Bardhan, R.; Bartels, M.; Perez-Torres, C.; Pautler, R. G.; Halas, N. ; Joshi, A. Mol. Cancer Ther., 2010, 9 (4), 1028.

90. Lu, A.H.; Salabas, E.L.; Schüth F. Angew. Chem. Int. Ed., 2007, 46, 1222.

91. Morales, M.P.; Verdaguer, S.V.; Montero, M.I.; Serna, C.; Roig, A.; Casas, L.I.; Martinez, B.; Sandiumenge, F. Chem.Mater., 1999, 11, 3058.

92. H. Martin, Magnetism in solids, The M.I.T press, Cambridge, Massachussets, 1967.

93. D. Jiles, Introduction to magnetism and magnetic materials, Chapman & Hall, 1991.

94. Colombo, M.; Romero, S.C.; Casula, M.F.; Gutie´rrez, L.; Morales, M.; Böhm, I.B.; Heverhagen, T.; Prosperi, D.; Parak, W. Chem. Soc. Rev., 2012, 41, 4306.

95. Jun, Y.W.; Seo, W.; Cheon, Acc. Chem. Res., 2008, 41,179.

96. Koseoglu, Y. Magn. Magn. Mater., 2006, 300, 327.

97. Jun, Y.W.; Lee, H.; Cheon, Angew. Chem. Int. Ed., 2008, 47, 5122.

98. Bellin, M.F. Eur. Radiol., 2006, 60, 314.

99. Harisinghani, M.G.; Jhaveri, K.S.; Weissleder, R.; Schima, W.; Saini, S.; Hahn, P.F.; Mueller, P.R. Clin. Radiol., 2001, 56, 714.

100. Sandhu, A.; Handa, H.; Abe, B. Nanotechnology, 2010, 21, 442001.

101. Jun, Y.W.; Huh, Y.M.; Choi, S. J Am Chem Soc., 2005, 127(16), 5732.

102. Gupta, A.K.; Gupta, M. Biomaterials, 2005, 26 (18), 3995.

103. Jun, Y.W.; Lee, H.; Cheon, Nanoparticle Contrast Agents for Molecular Magnetic Resonance Imaging. in: Mirkin, C.A. Niemeyer MC eds. Nanobiotechnology II: More Concepts and Applications. Weinheim: Wiley-VCH, 2007.

104. Laurent, S.; Forge, D.; Port, M. Chem Rev., 2008, 108(6), 2064.

105. Lawaczeck, R.D.; Menzel, M.; Pietsch, H. Appl Organomet Chem, 2004, 18, 506.

106. Bee, A.; Massart, R.; Neveu, S. J Magn and Magn Mat, 1995, 149, 6.

107. Burda, C.; Chen, X.; Narayanan, R. Chem Rev., 2005,105(4), 1025.

108. Pedro T, P MM, Sabino VV et al. Synthesis, Properties and Biomedical Applications of Magnetic Nanoparticles. in: Buschow KHJ ed. Handbook of Magnetic Materials. The Netherlands: Elsevier B V, 2006.

109. Sun, S.; Zeng, H. J Am Chem Soc., 2002, 124 (28), 8204.

110. Hyeon, T.; Lee, S.S.; Park, J Am Chem Soc., 2001, 123 (51), 12798.

111. Lopez-Perez A.; Lopez-Quintela M.A.; Mira, IEEE Trans Magn, 1997, 33 (5), 4359.

112. Degiorgio V. Physics of amphiphiles: micelles, vesicles and microemulsions. Amsterdam: 1985.

113. Wan, S.; Huang, ; Guo, M. J Biomed Mater Res A, 2007, 80 (4), 946.

114. Stöber, W.; Fink, A.; Bohn, E. J Colloid and Interface Sci., 1968, 26 (1), 62.

115. Li, H.; Cheng, F.;Duft, A.M.; Adronov, A. J. Am. Chem. Soc., 2005, 127 (41), 14518.

116. Chaskar, A.C.; Bandgar, B.P.; Modhave, R.K.; Patil A.B. Synthetic Communications: An International Journal for Rapid Communication of Synthetic Organic Chemistry, 39, 6, 992.

117. Xu, H.; Wan, X.; Shen, Y.Y.; Xu, S.; Feng, Y.S. Org. Lett., 2012, 14 (5), 1210.

118. Kralj, S.; Drofenik, M.; Makovec, D. Nanopart Res., 2011, 13, 2829.

119. Deng, Y.H.; Wang, C.C.; Hu, H.; Yang, W.L.; Fu, S.K. Colloids and Surfaces A: Physicochem. Eng. Aspects, 262, 2005, 87.

120. Lee, ; Isobe, T.; Senna, M. Colloid Interface Sci. 177, 1996, 490.

121. Mohammad-Beigi, H.; Yaghmaei, S.; Roostaazad, R.; Bardania, H.; Arpanaei, A. Physica, 2011, E44, 618.

122. Liu, Q.; Xu, Z.; Finch, A.; Egerton, R. Chem. Mater., 1998, 10 (12), 3936.

123. Koh, I.; Wang, X.; Varughese, B.; Isaacs,L.; Ehrman S.H.; English, D.S. Phys. Chem. B, 2006, 110, 1553.

APPENDIX A

MASS SPECTRA

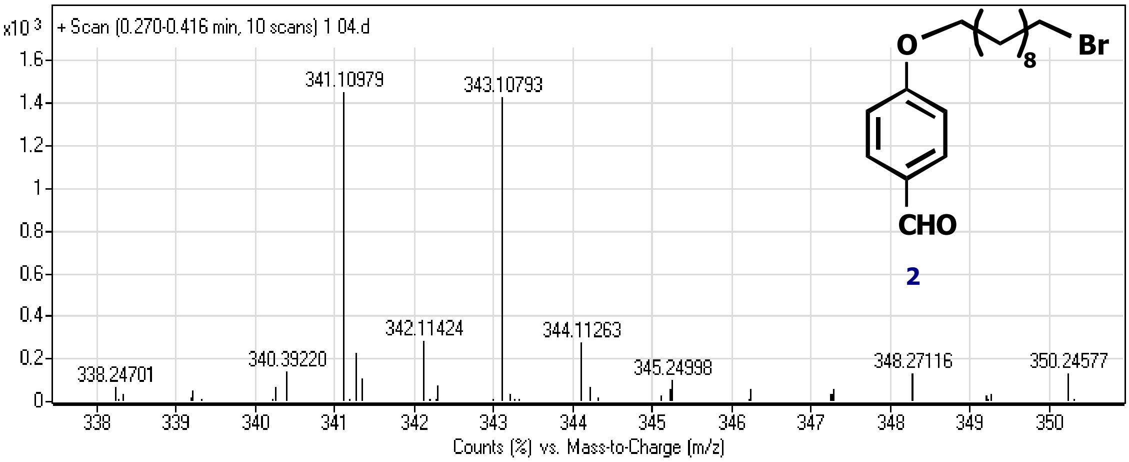

Figure 54. *APCI – HRMS of Compound 2*

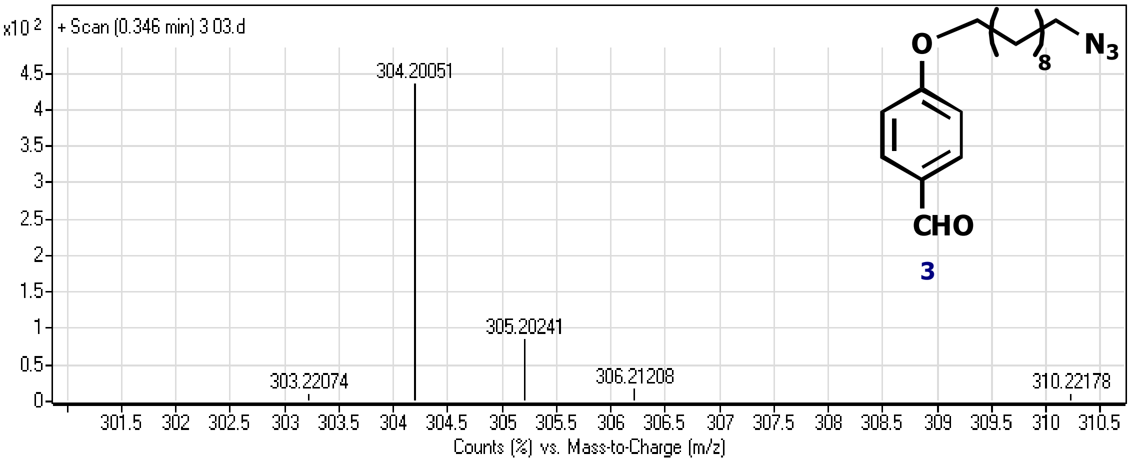

Figure 55. *APCI – HRMS of Compound 3*

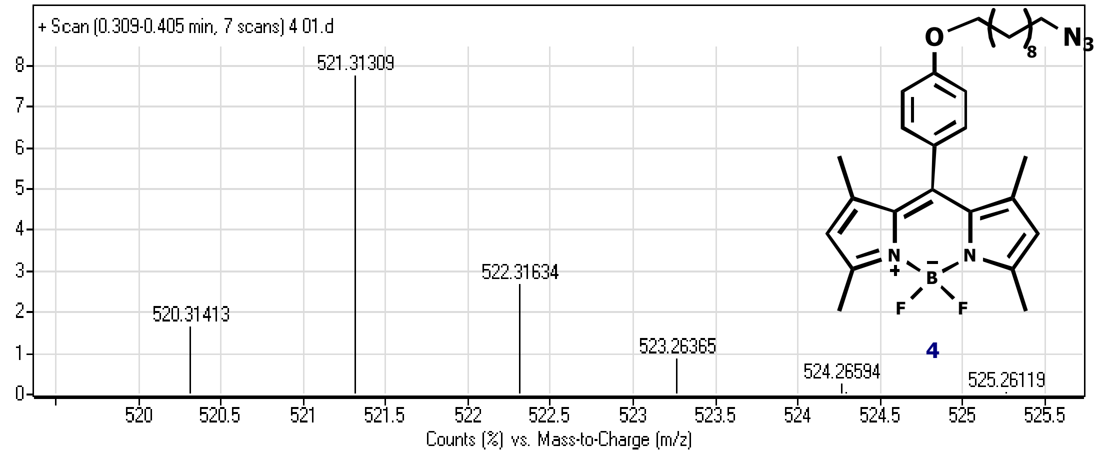

Figure 56. *APCI – HRMS of Compound 4*

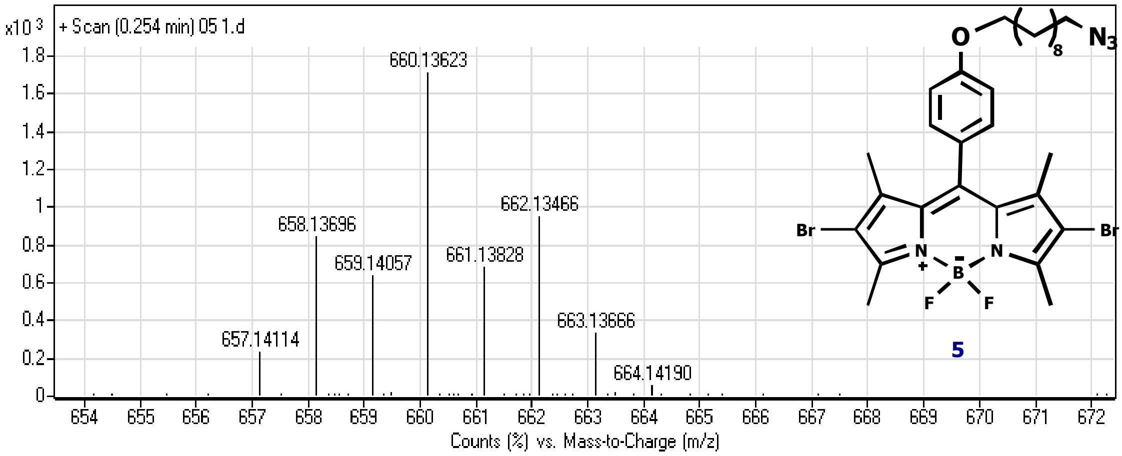

Figure 57. *APCI – HRMS of Compound 5*

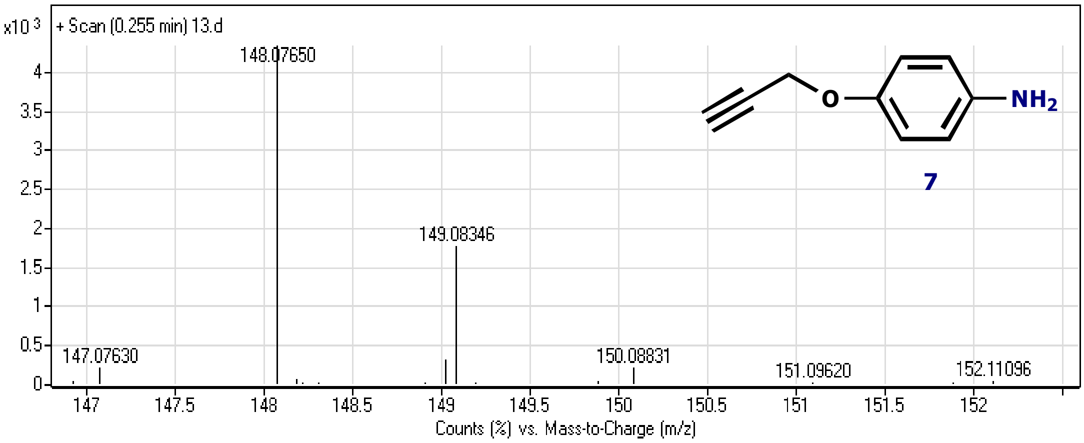

Figure 58. *APCI – HRMS of Compound 7*

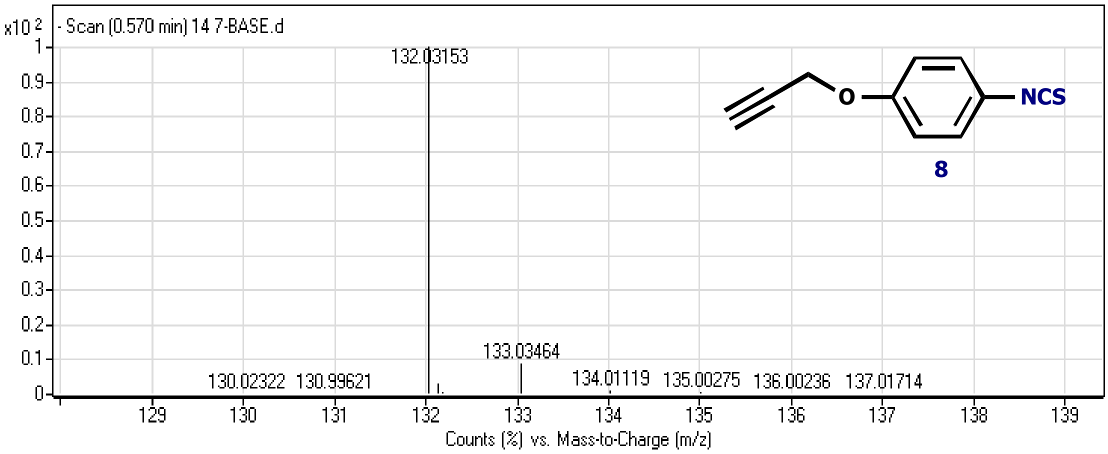

Figure 59. *APCI – HRMS of Compound 8*

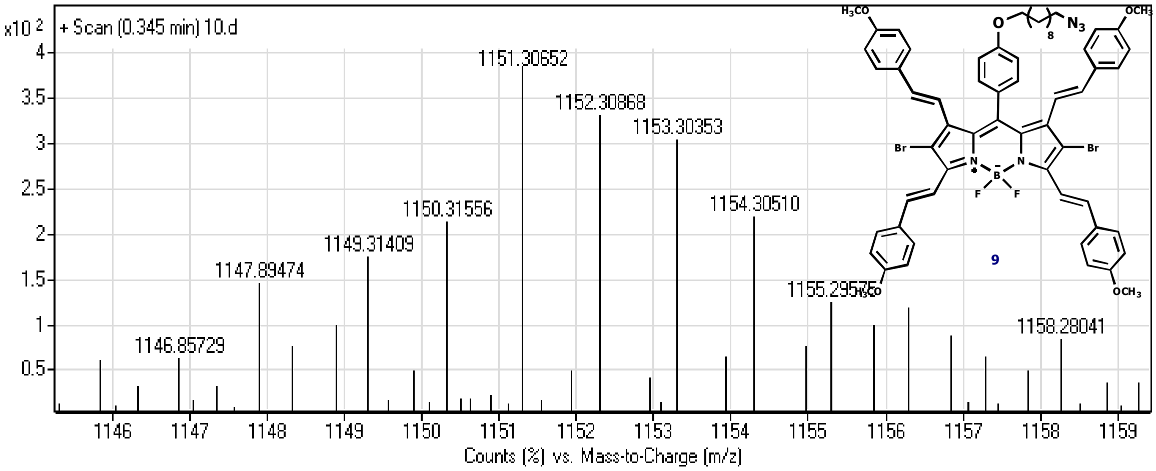

Figure 60. *APCI – HRMS of Compound 9*

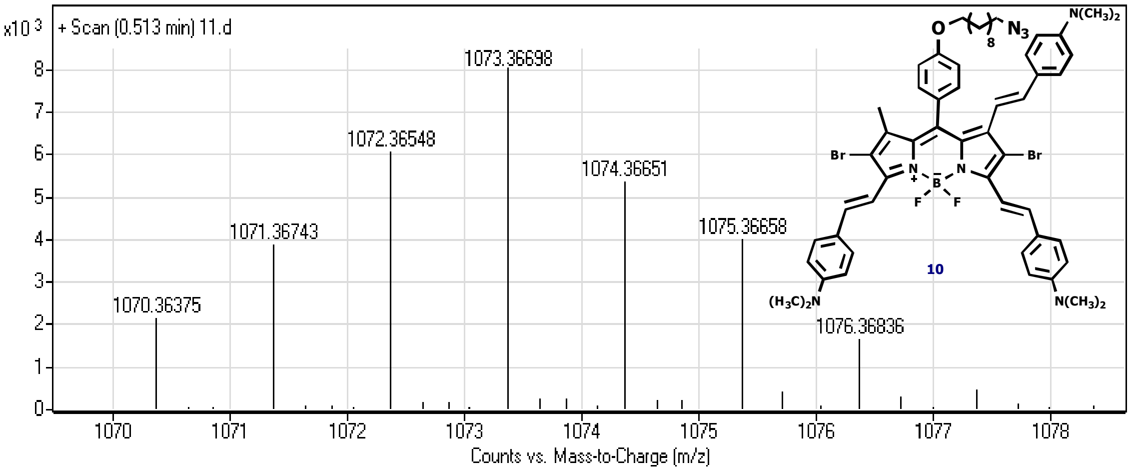

Figure 61. *APCI – HRMS of Compound 10*

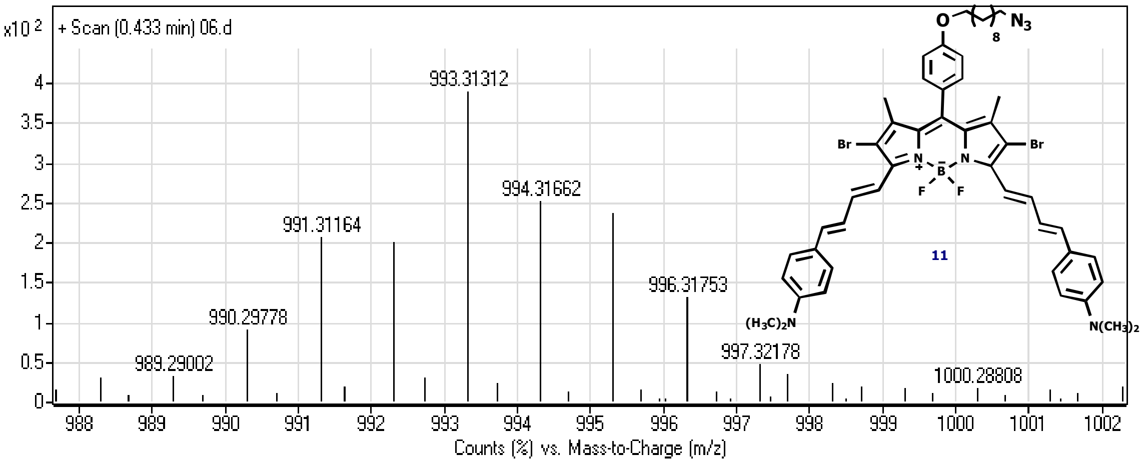

Figure 62. *APCI – HRMS of Compound 11*

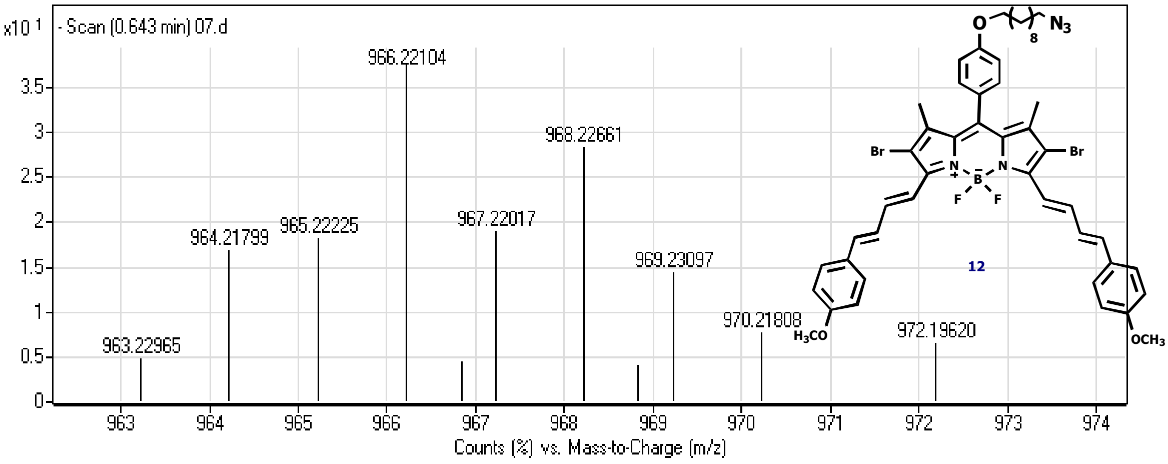

Figure 63. *APCI – HRMS of Compound 12*

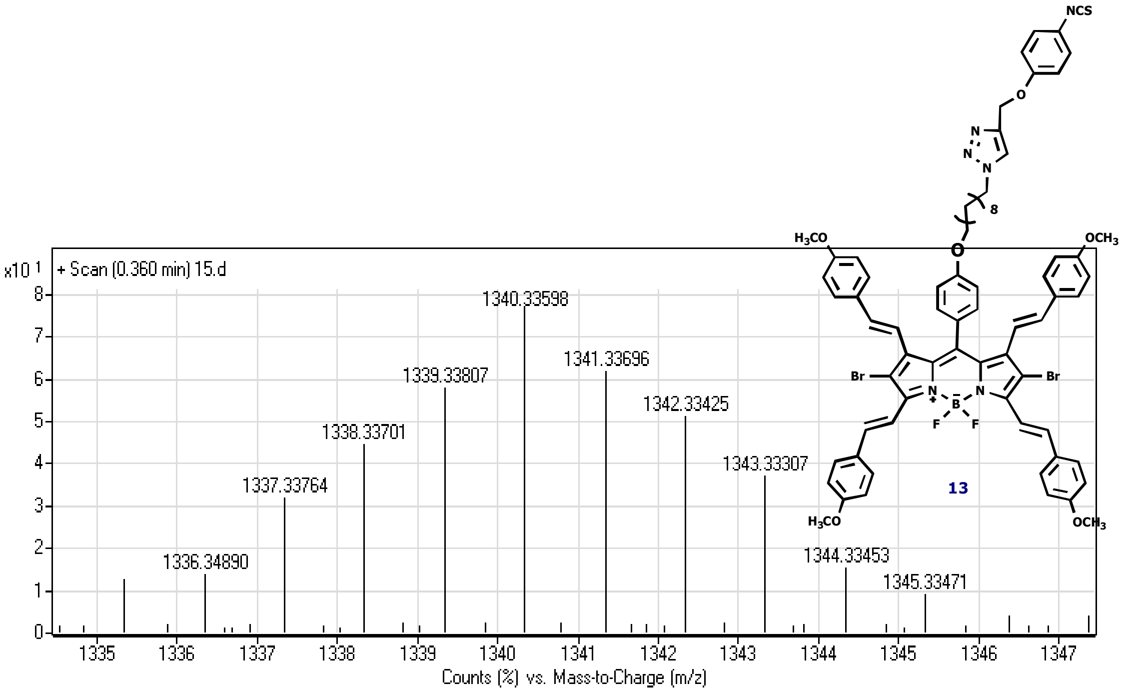

Figure 64. *APCI – HRMS of Compound 13*

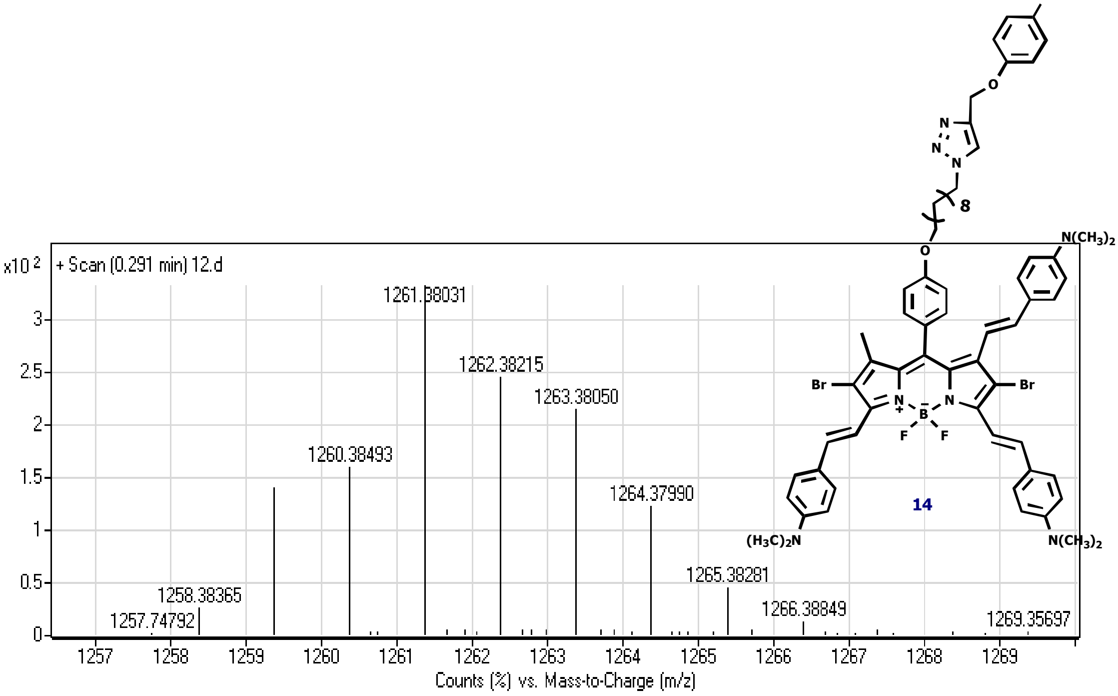

Figure 65. *APCI – HRMS of Compound 14*

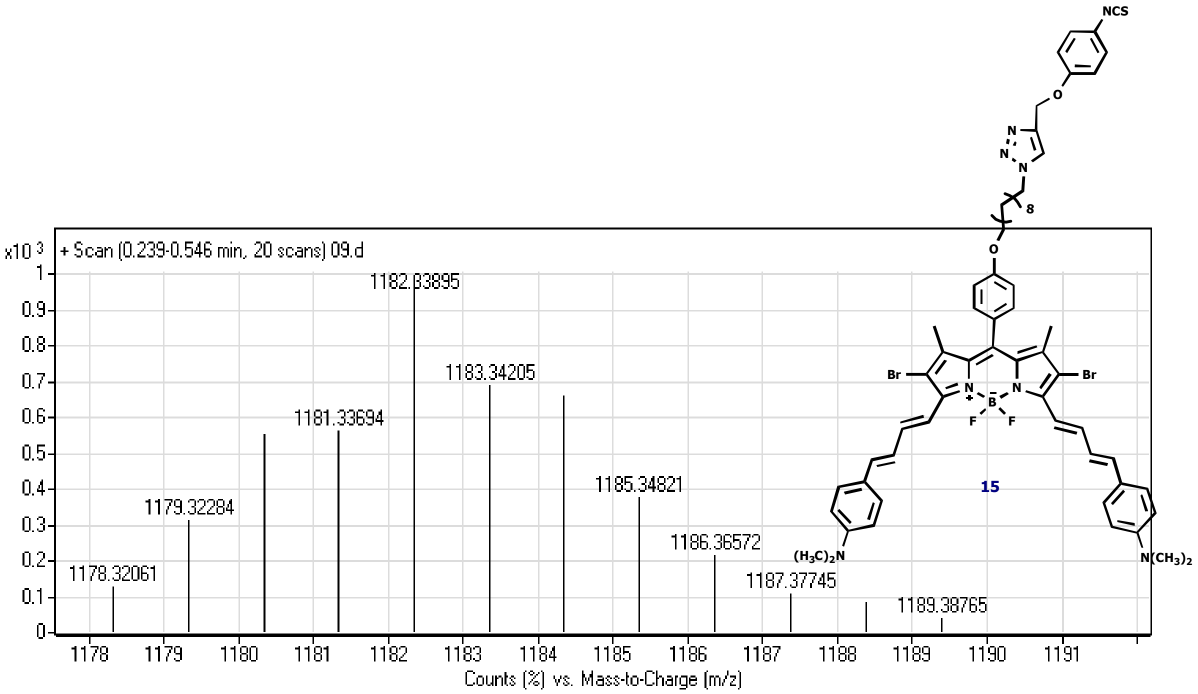

Figure 66. *APCI – HRMS of Compound 15*

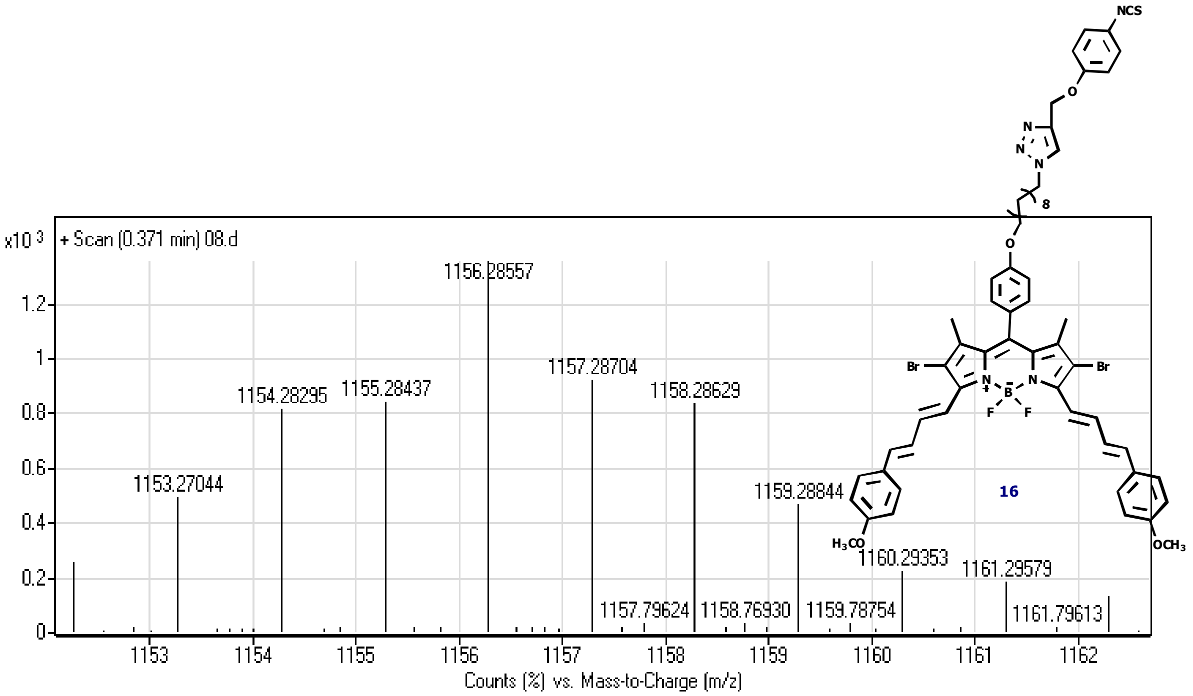

Figure 67. *APCI – HRMS of Compound 16*

APPENDIX B – NMR SPECTRA

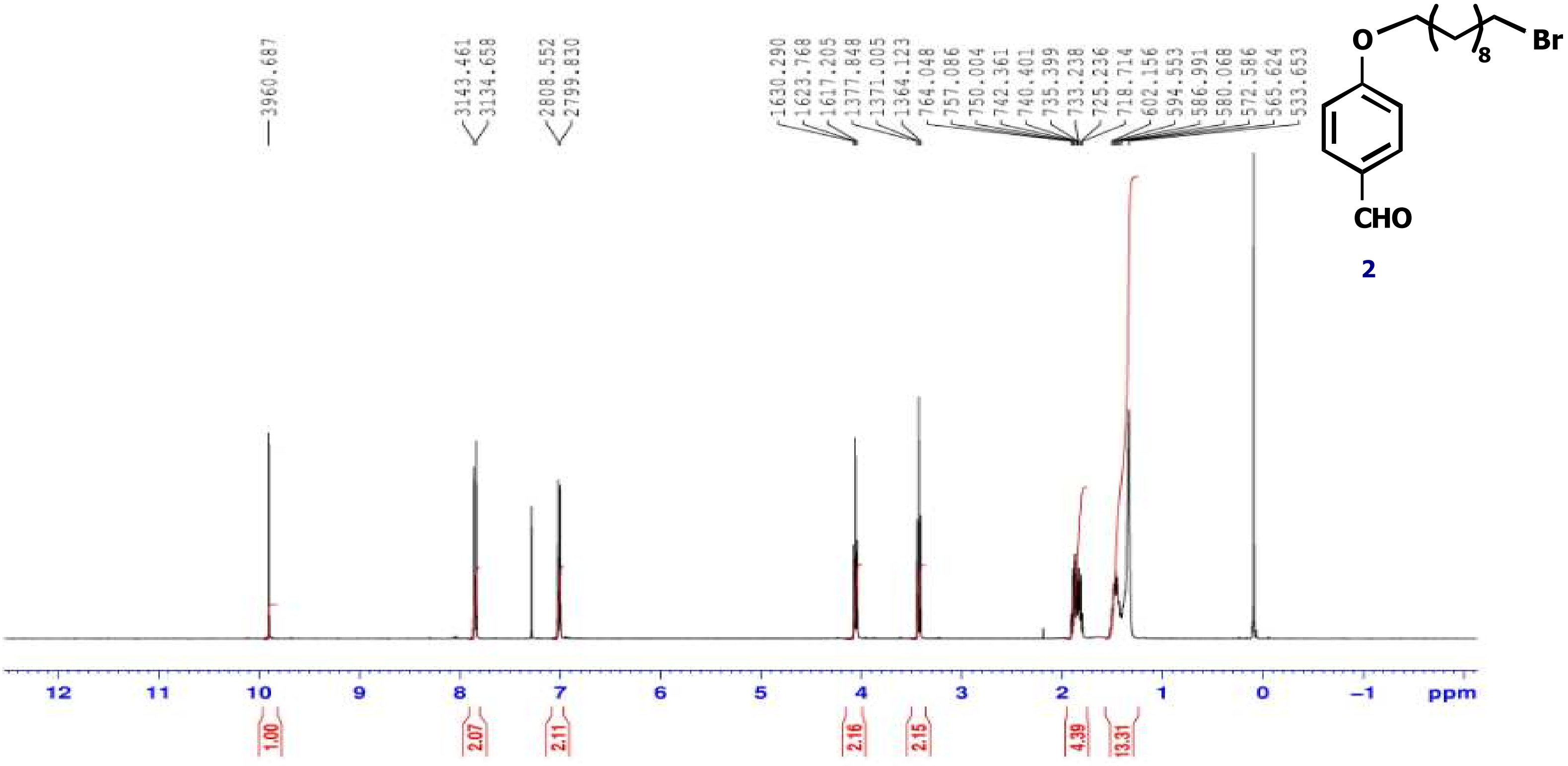

Figure 68: ^{1}H NMR Spectrum of Compound 2

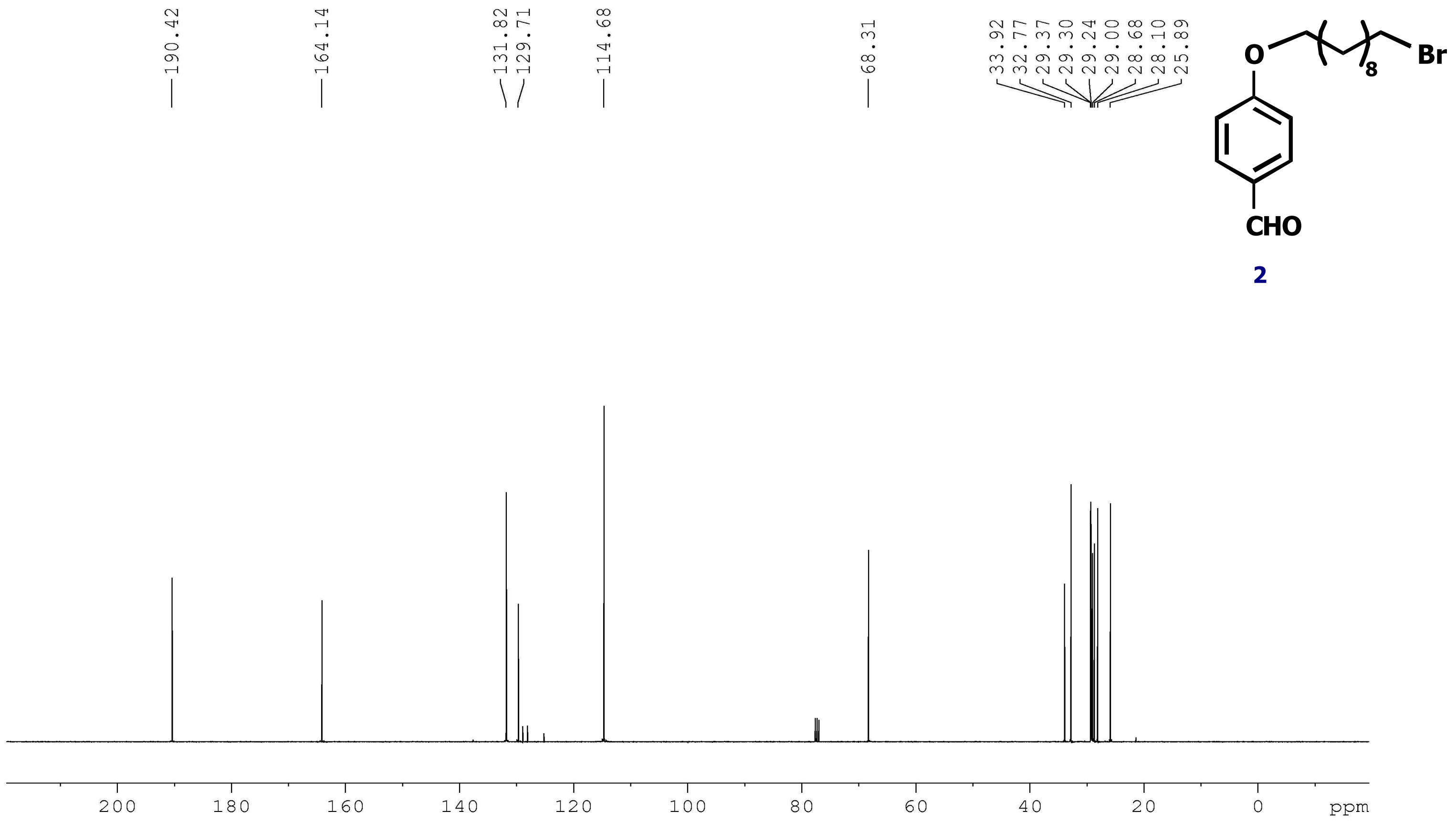

Figure 69: ^{13}C NMR Spectrum of Compound 2

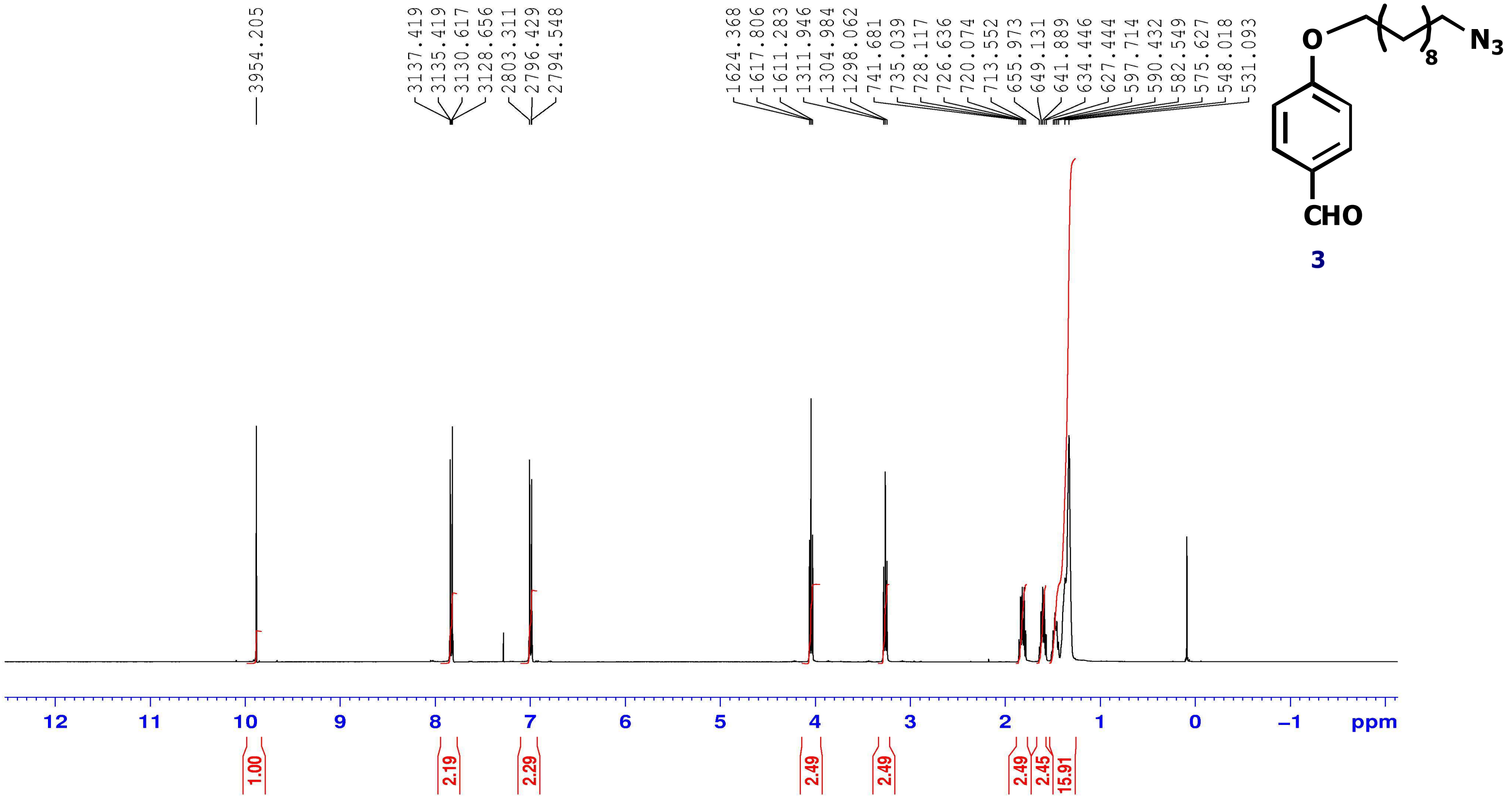

Figure 70: ^{1}H NMR Spectum of Compound 3

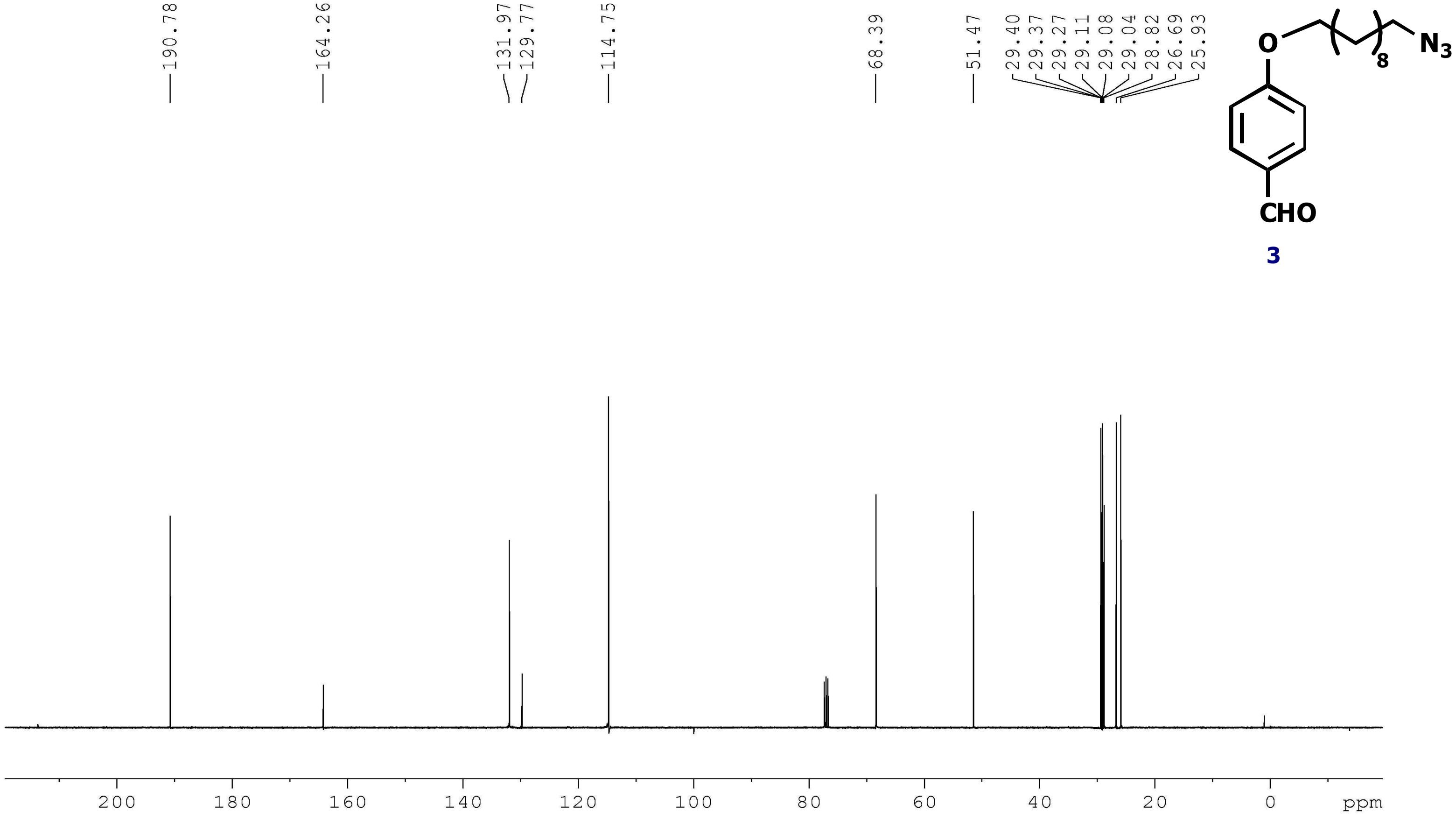

Figure 71: ^{13}C NMR Spectrum of Compound 3

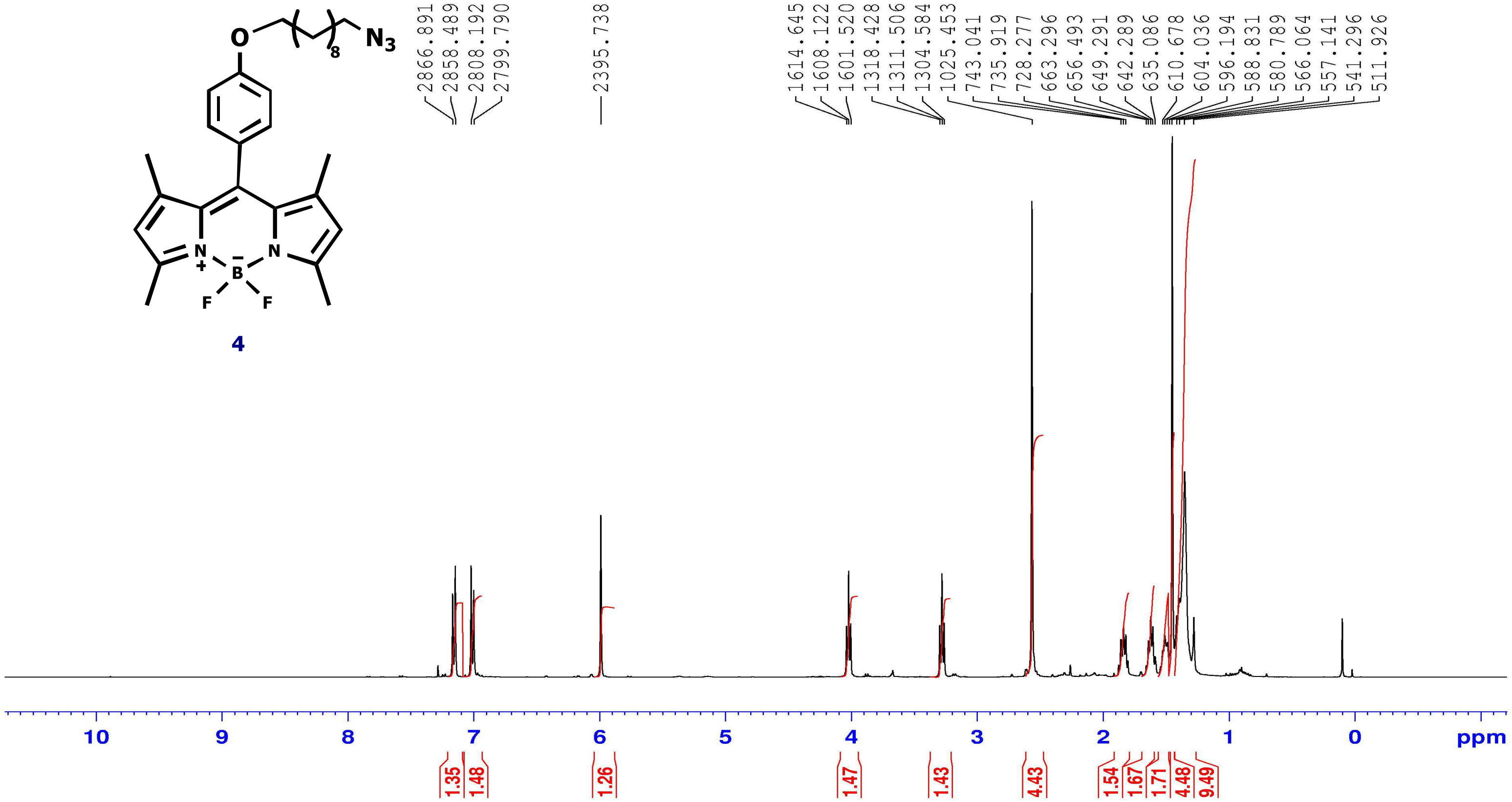

Figure 72: ^{1}H NMR Spectrum of Compound 4

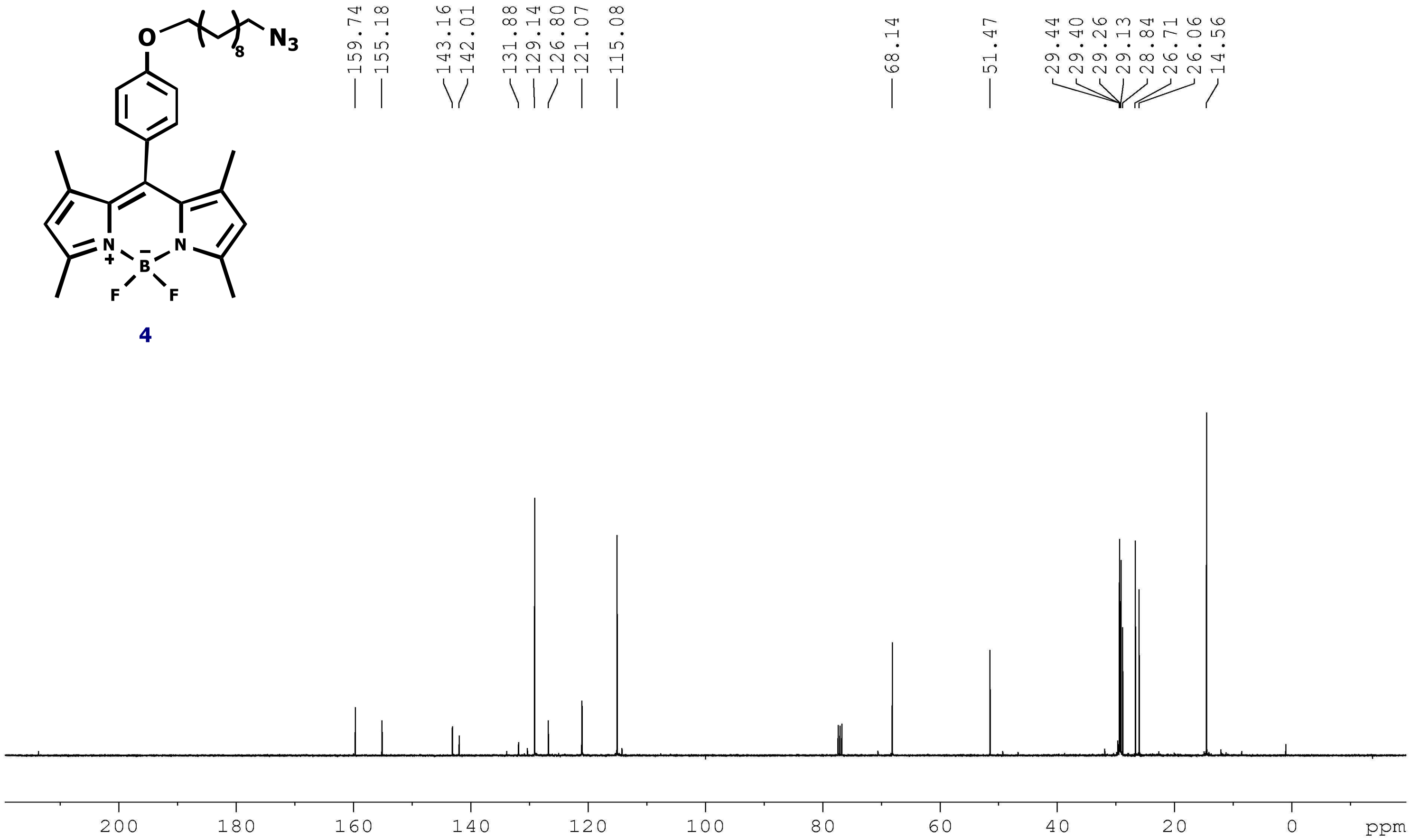

Figure 73: ^{13}C NMR Spectrum of Compound 4

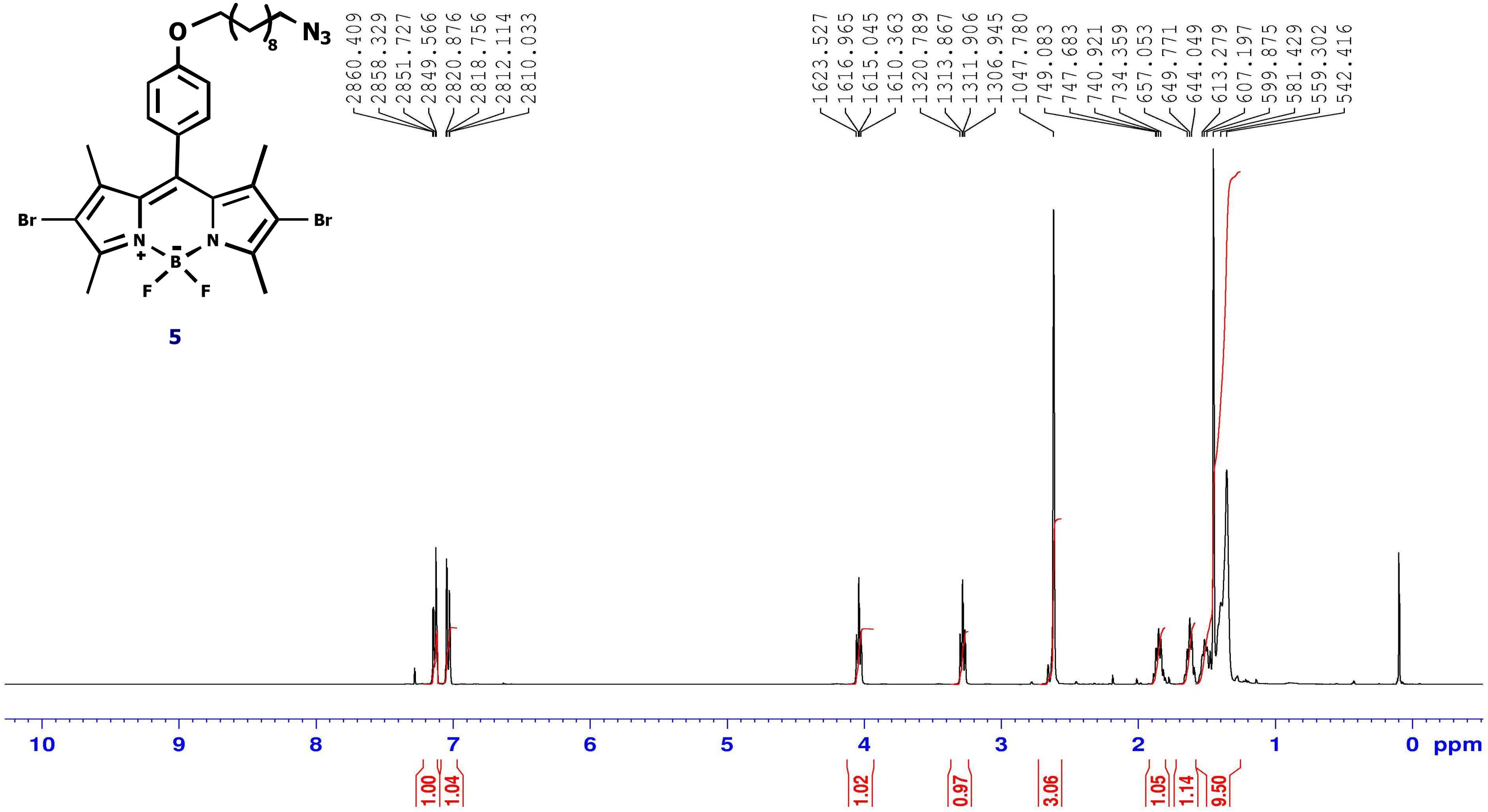

Figure 74: ^{1}H NMR Spectrum of Compound 5

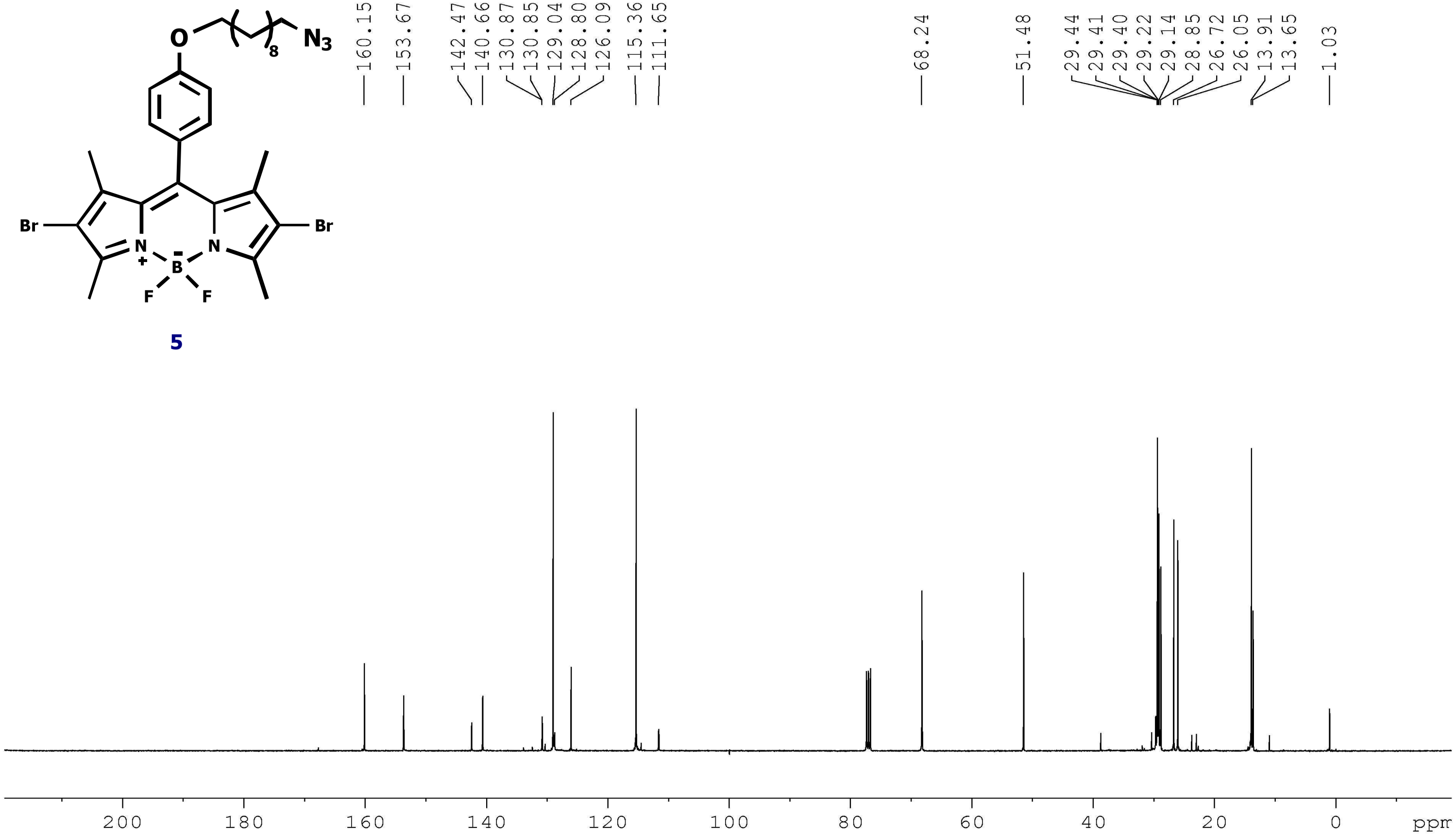

Figure 75: ^{13}C NMR Spectrum of Compound 5

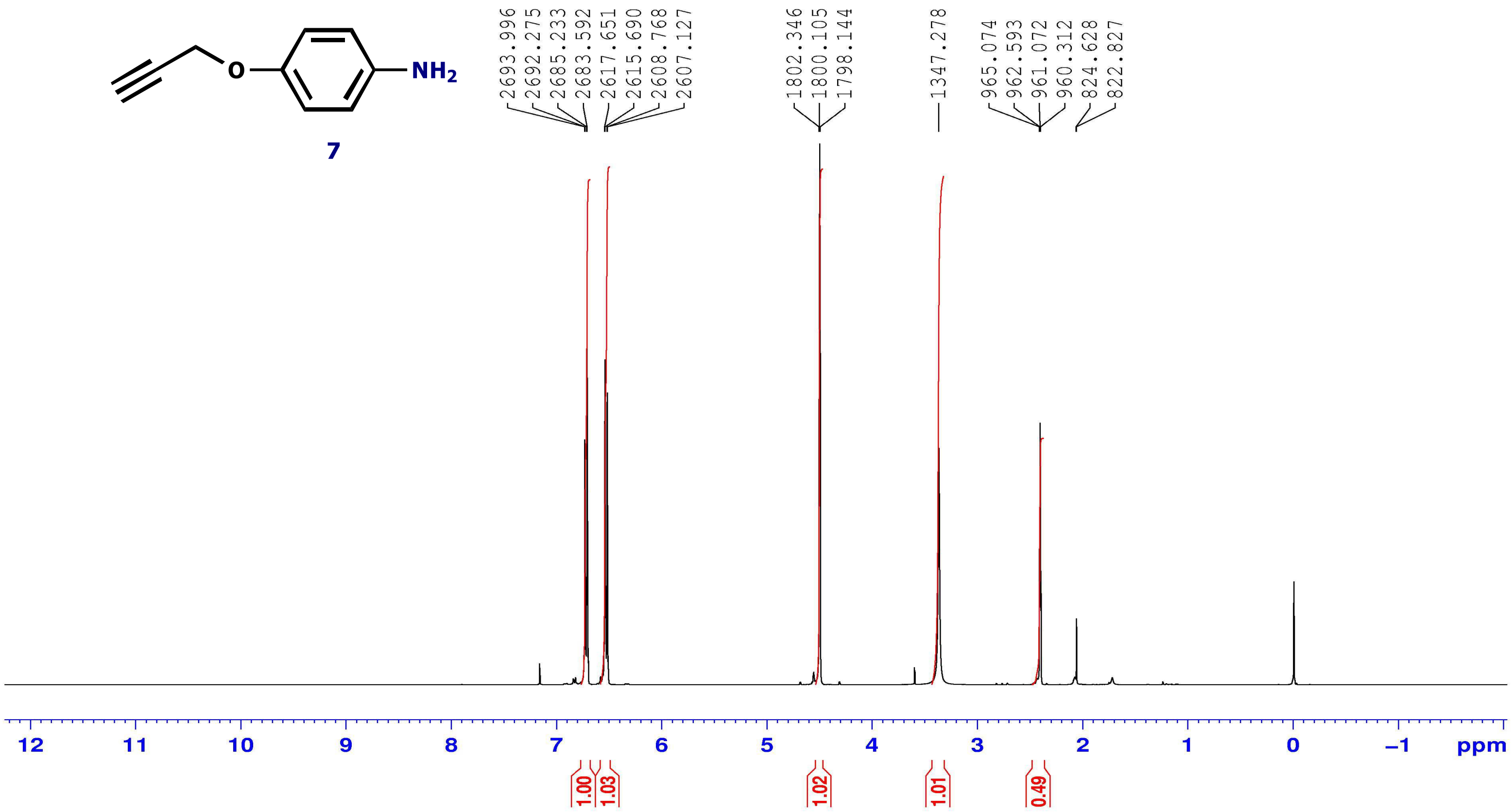

Figure 76: ^{1}H NMR Spectrum of Compound 7

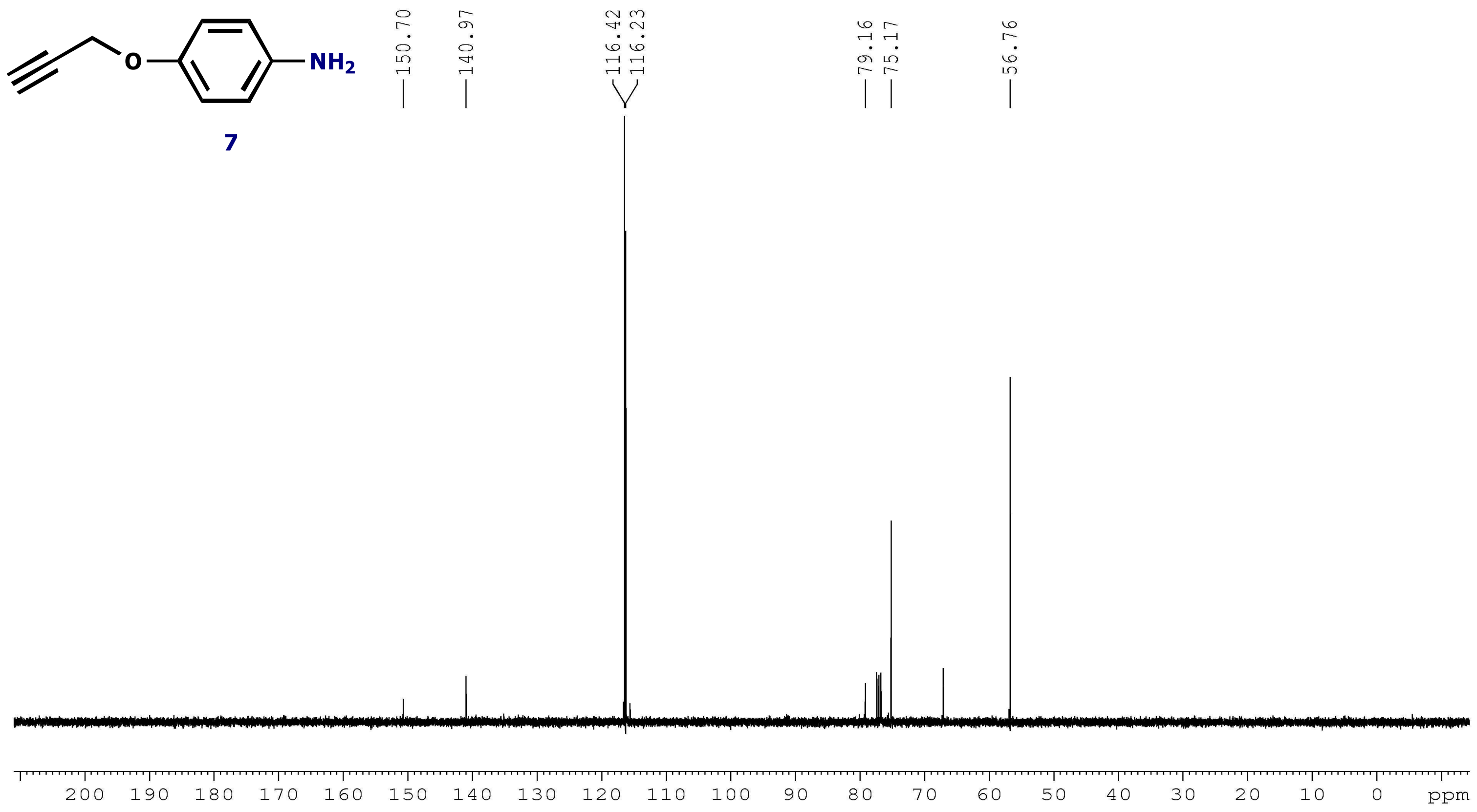

Figure 77: ^{13}C NMR Spectrum of Compound 7

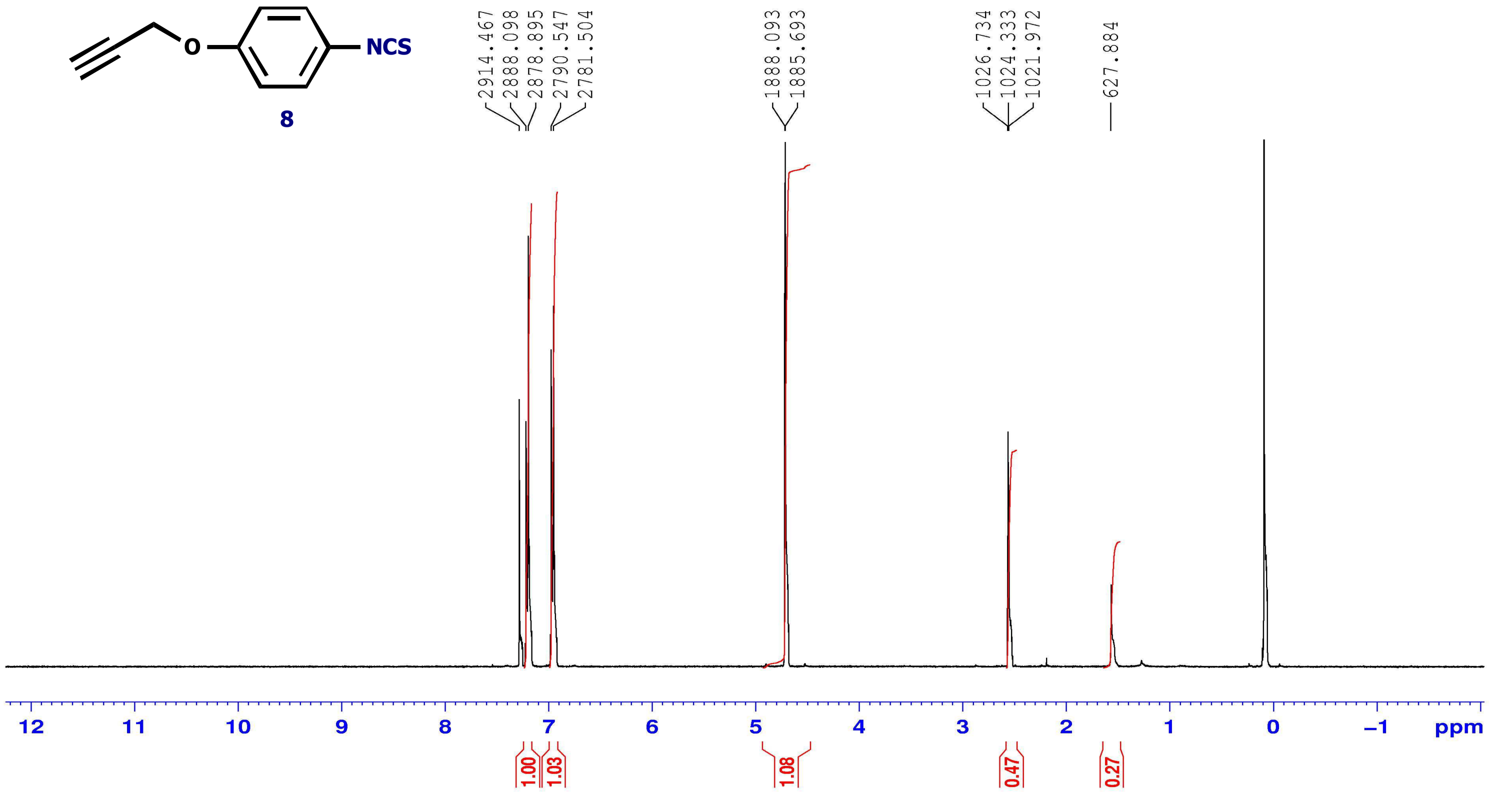

Figure 78: ^{1}H NMR Spectrum of Compound 8

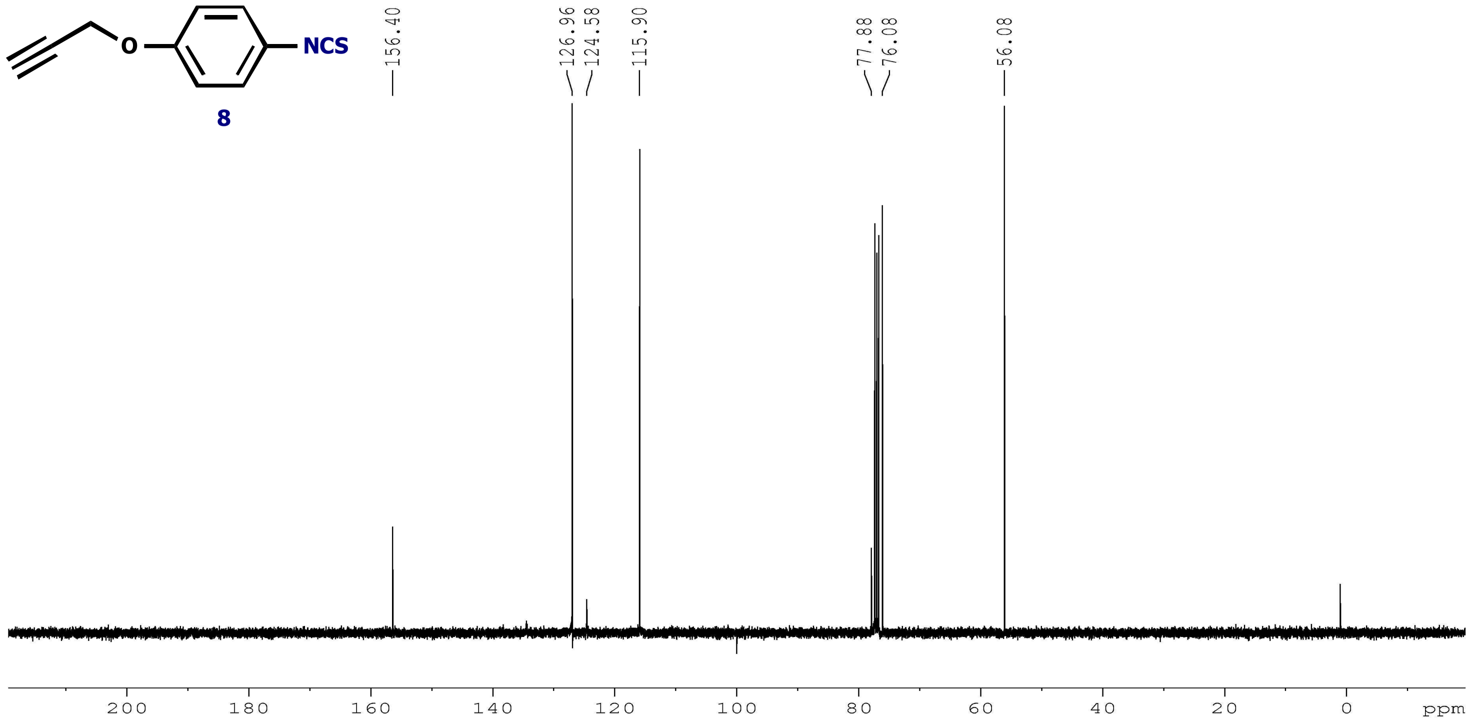

Figure 79: ^{13}C NMR Spectrum of Compound 8

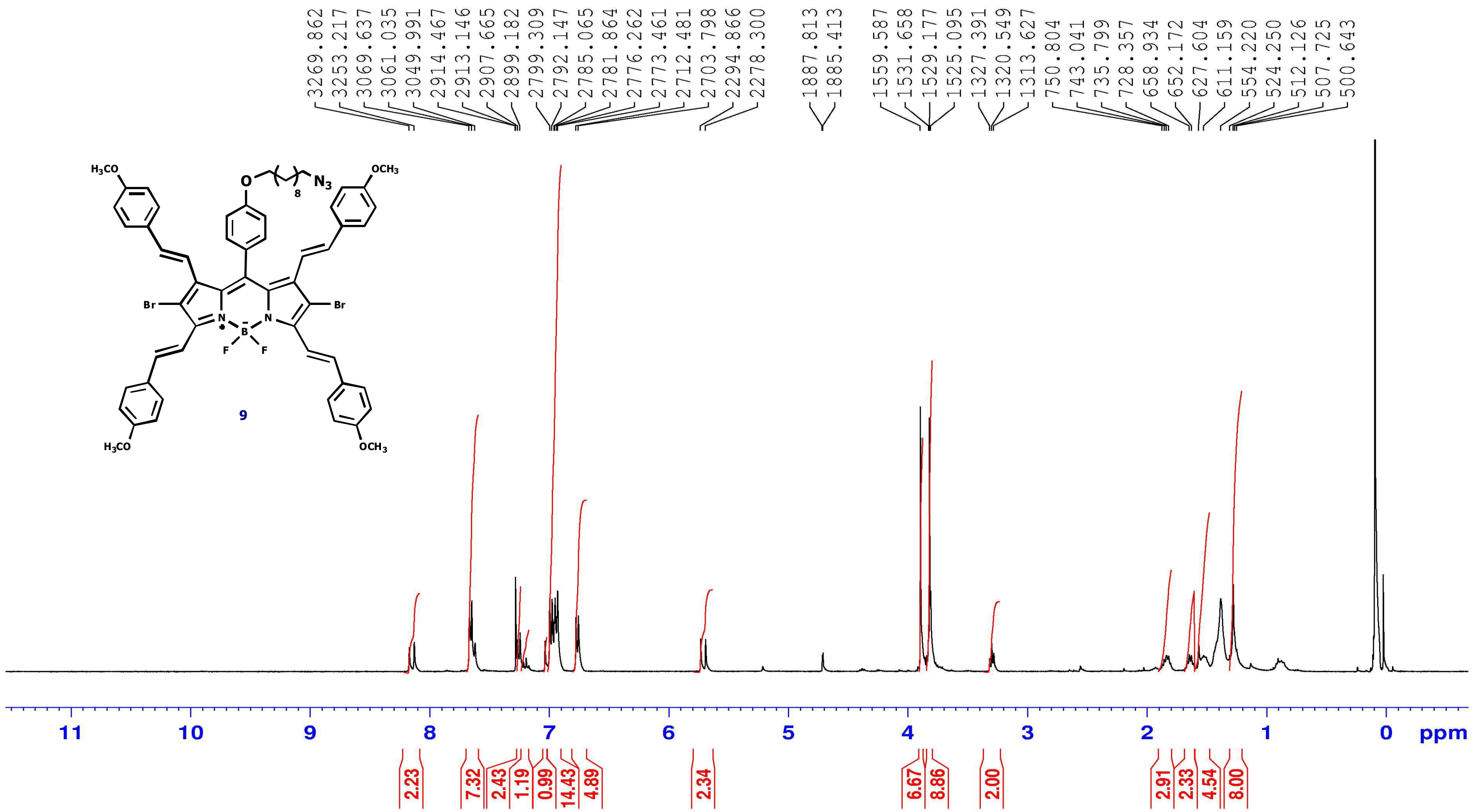

Figure 80: ^{1}H NMR Spectrum of Compound 9

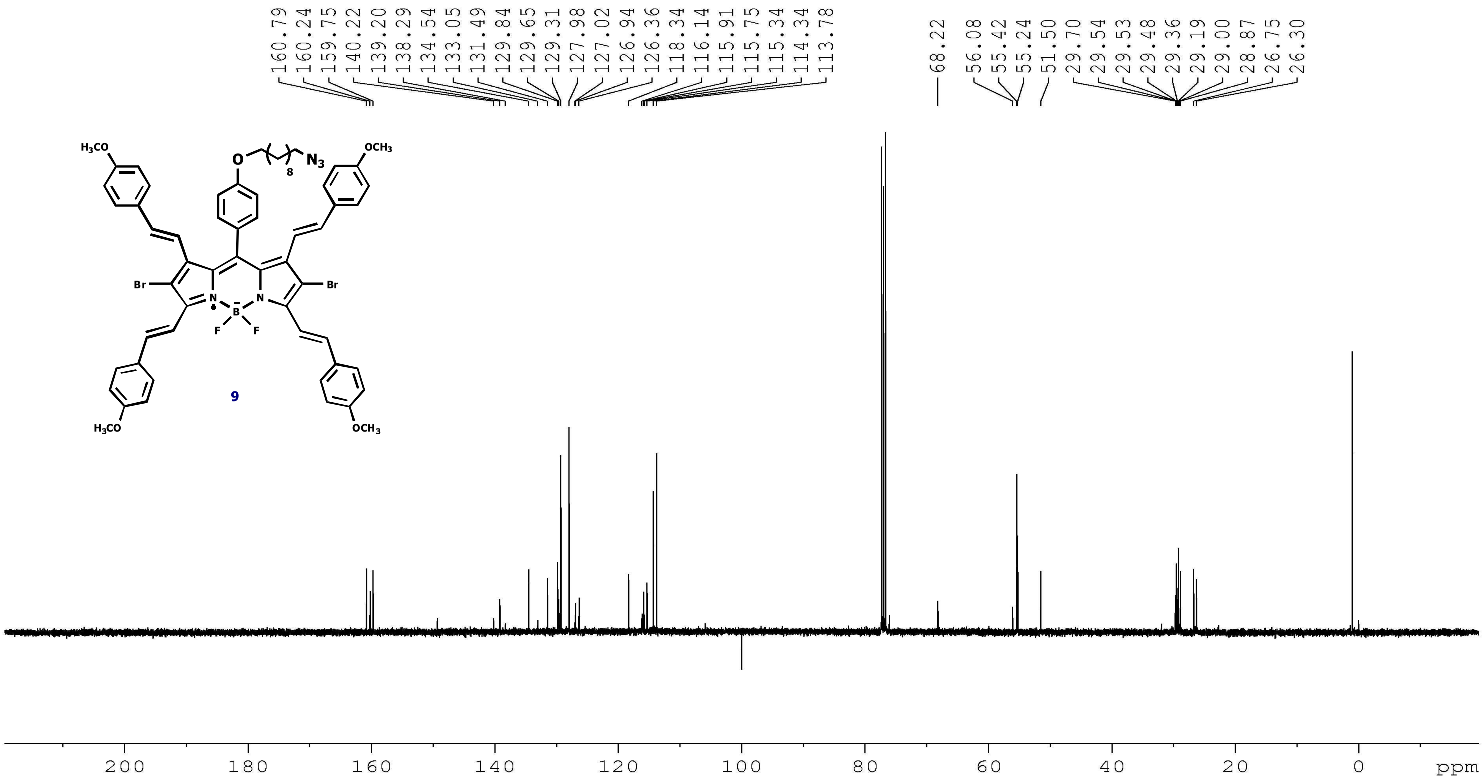

Figure 81: ^{13}C NMR Spectrum of Compound 9

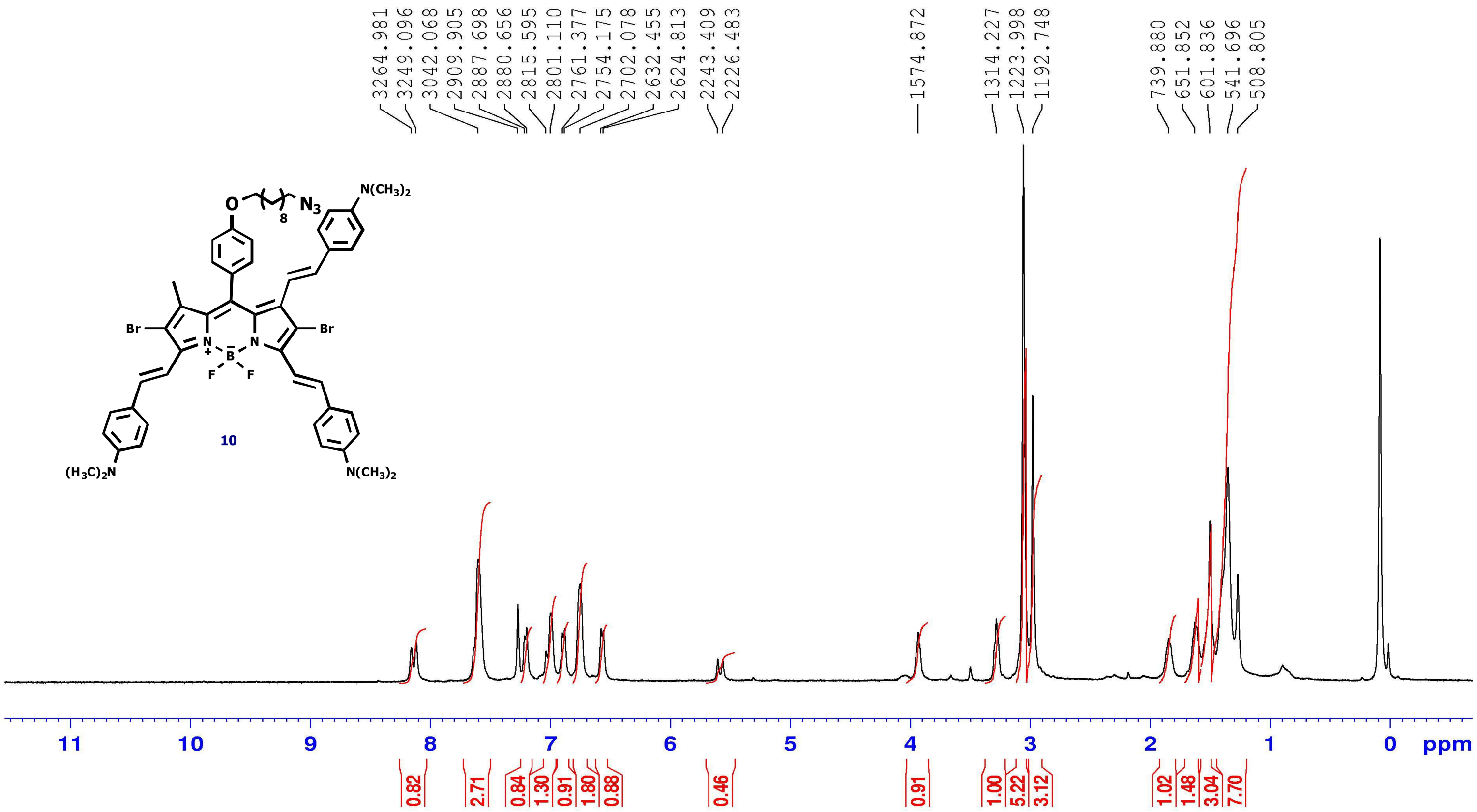

Figure 82: ^{1}H NMR Spectrum of Compound 10

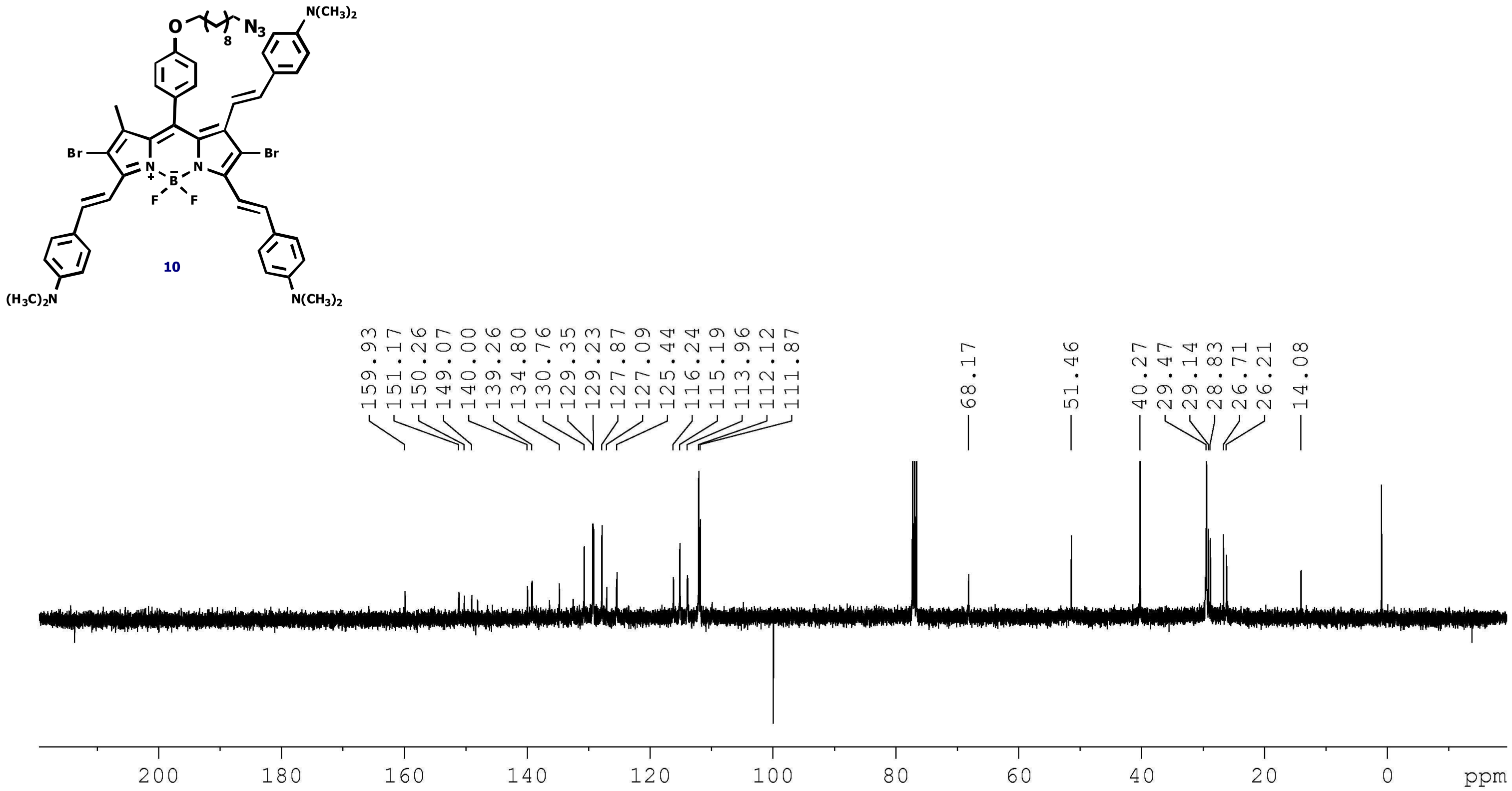

Figure 83: ^{13}C NMR Spectrum of Compound 10

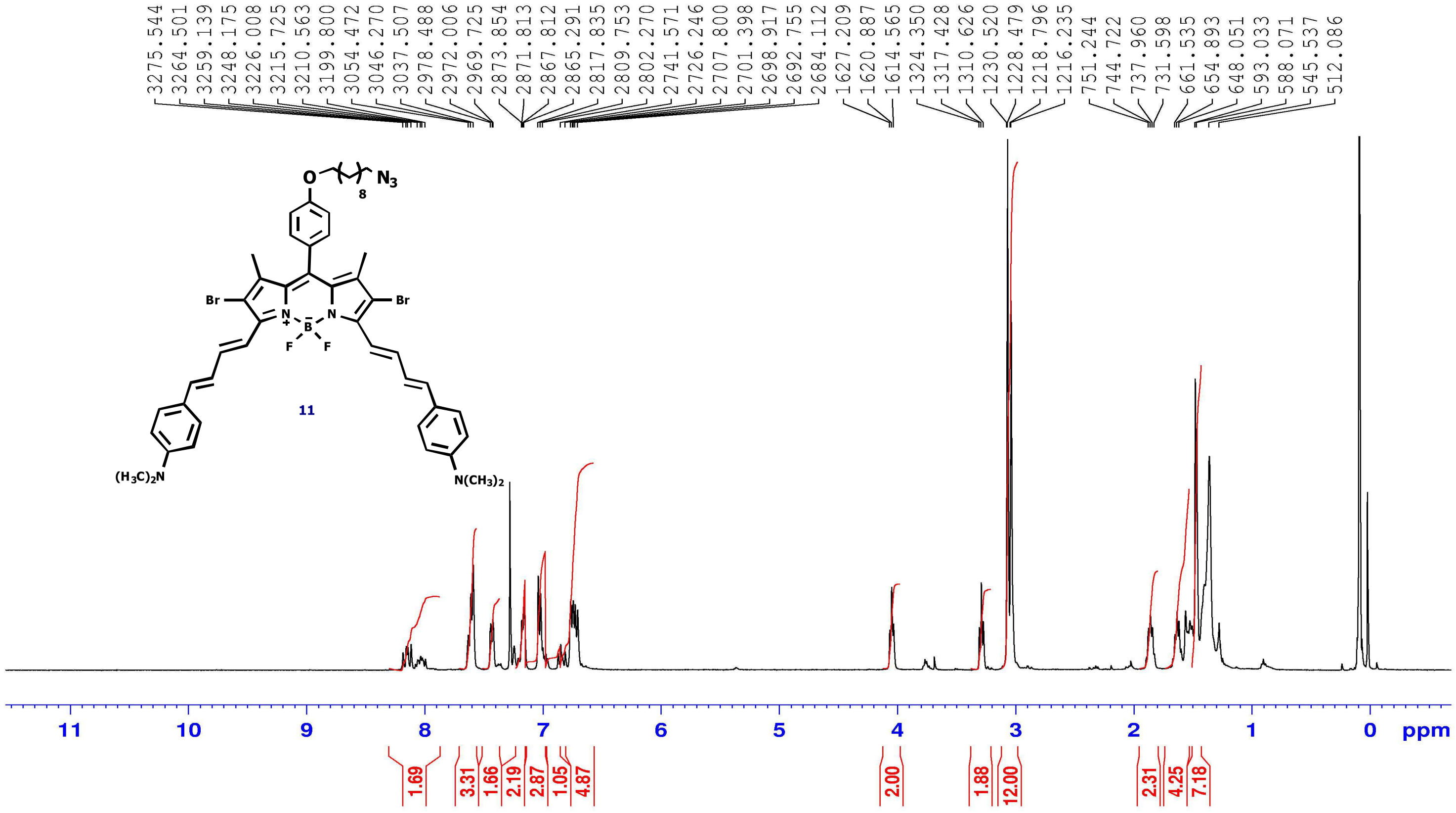

Figure 84: ^{1}H NMR Spectrum of Compound 11

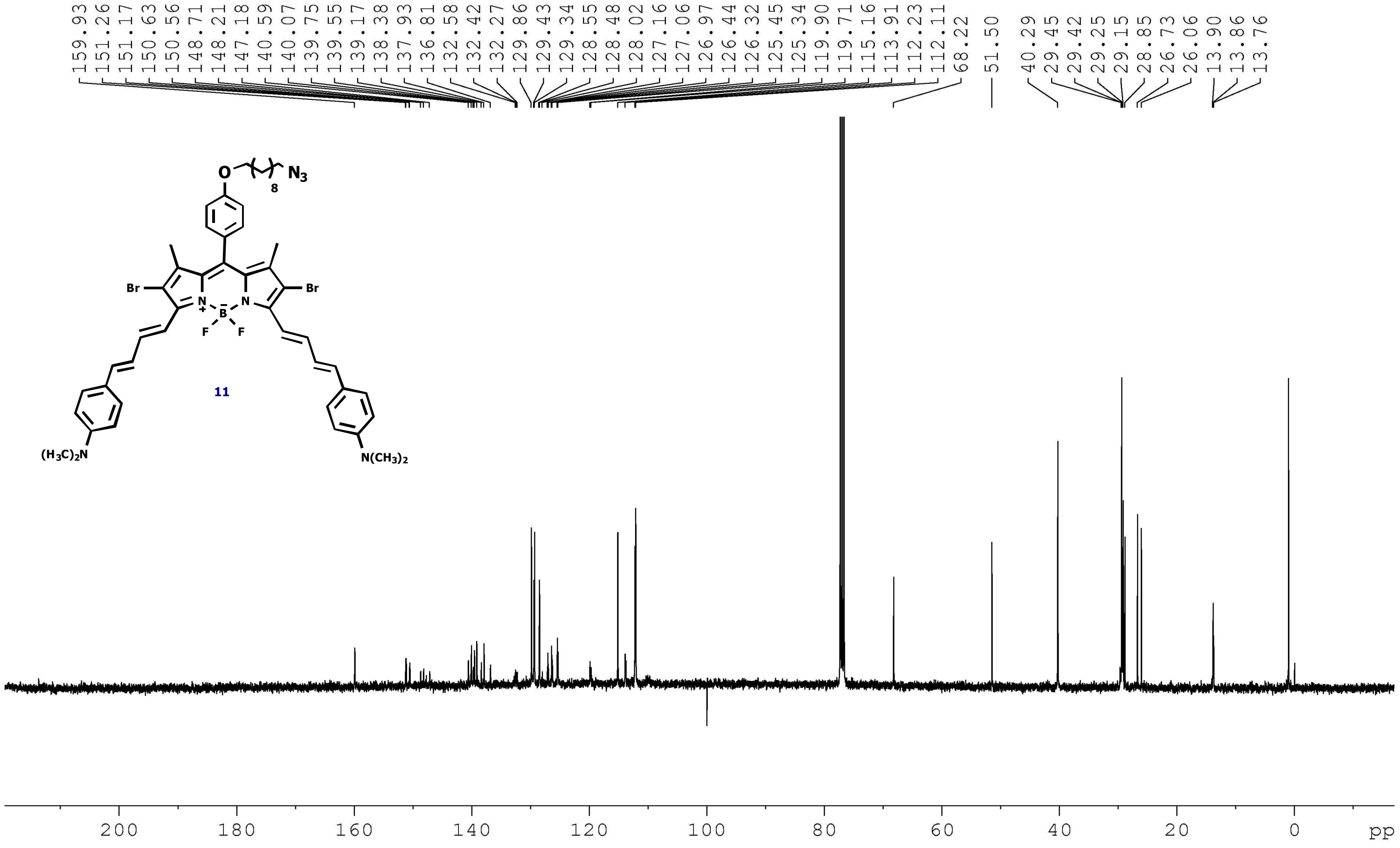

Figure 85: ^{13}C NMR Spectrum of Compound 11

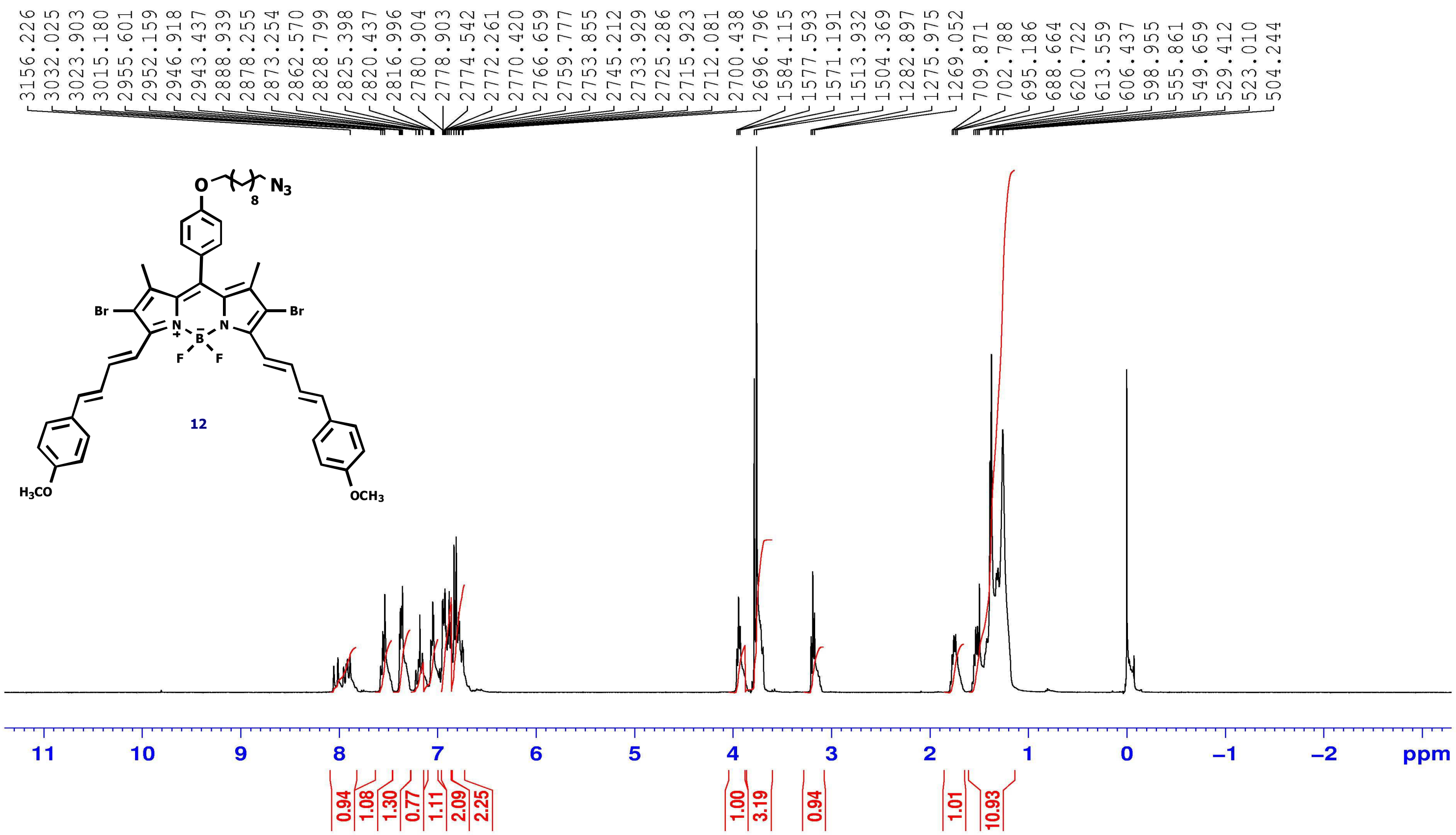

Figure 86: ^{1}H NMR Spectrum of Compound 12

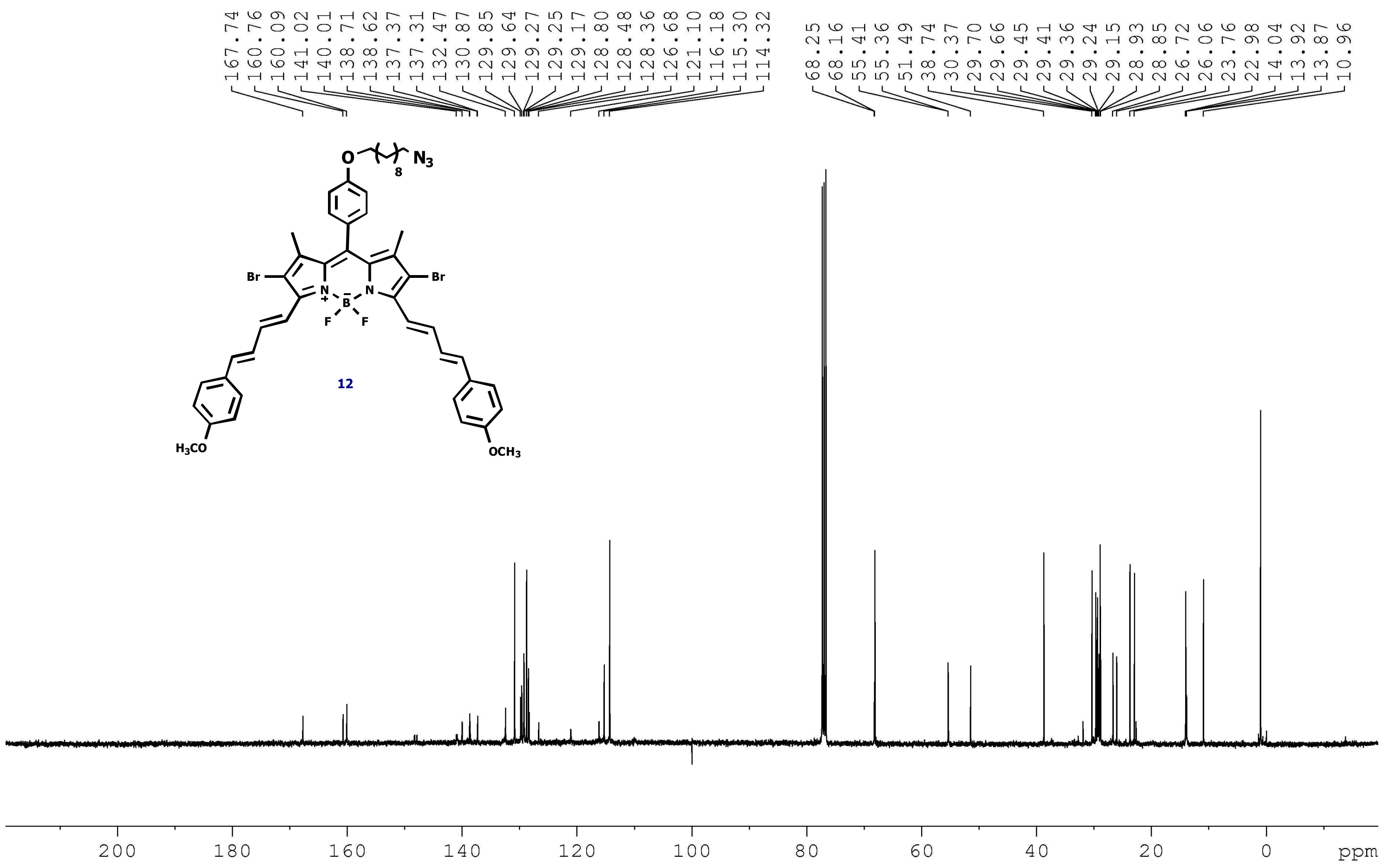

Figure 87: ^{13}C NMR Spectrum of Compound 12

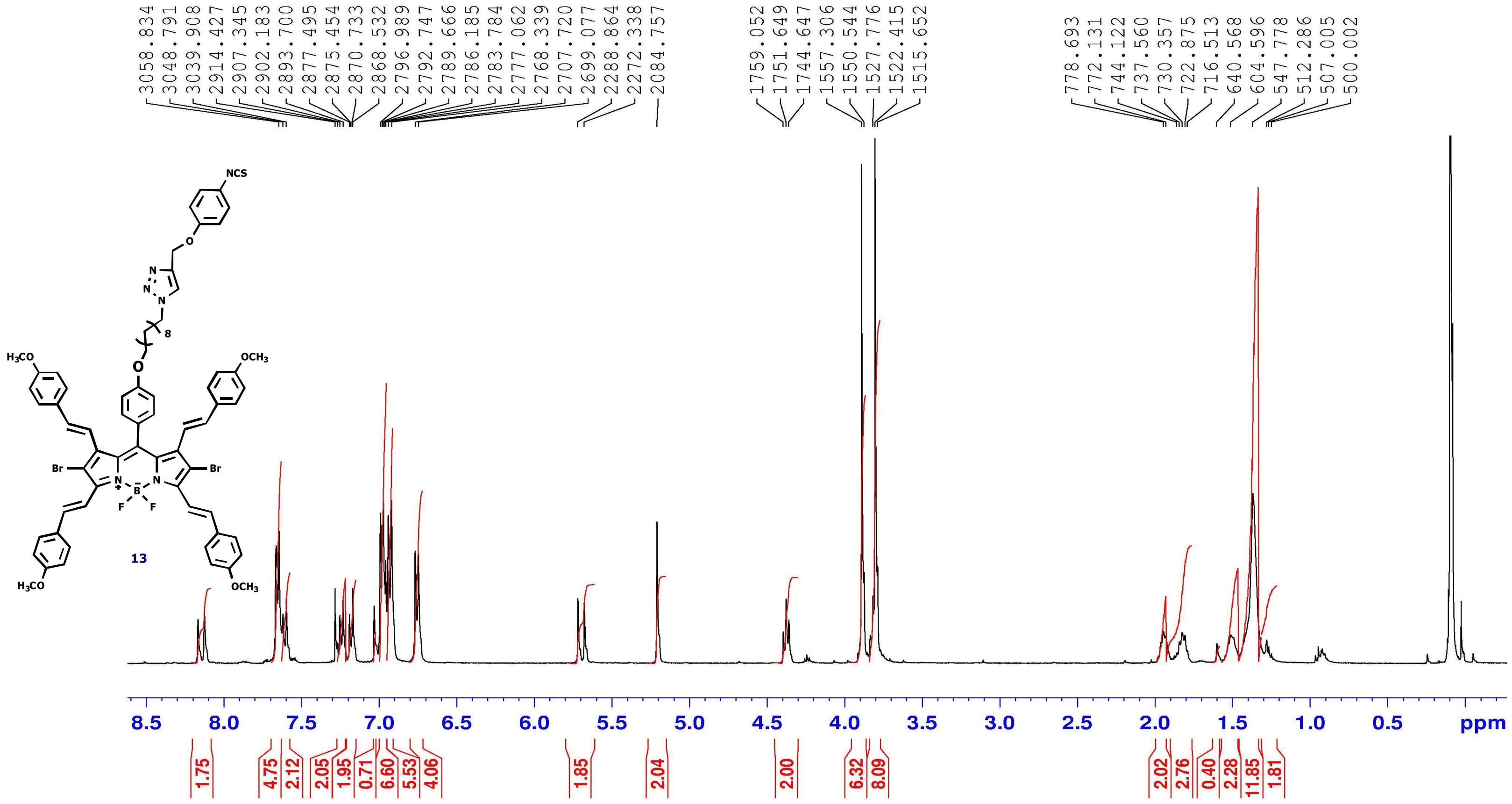

Figure 88: ^{1}H NMR Spectrum of Compound 13

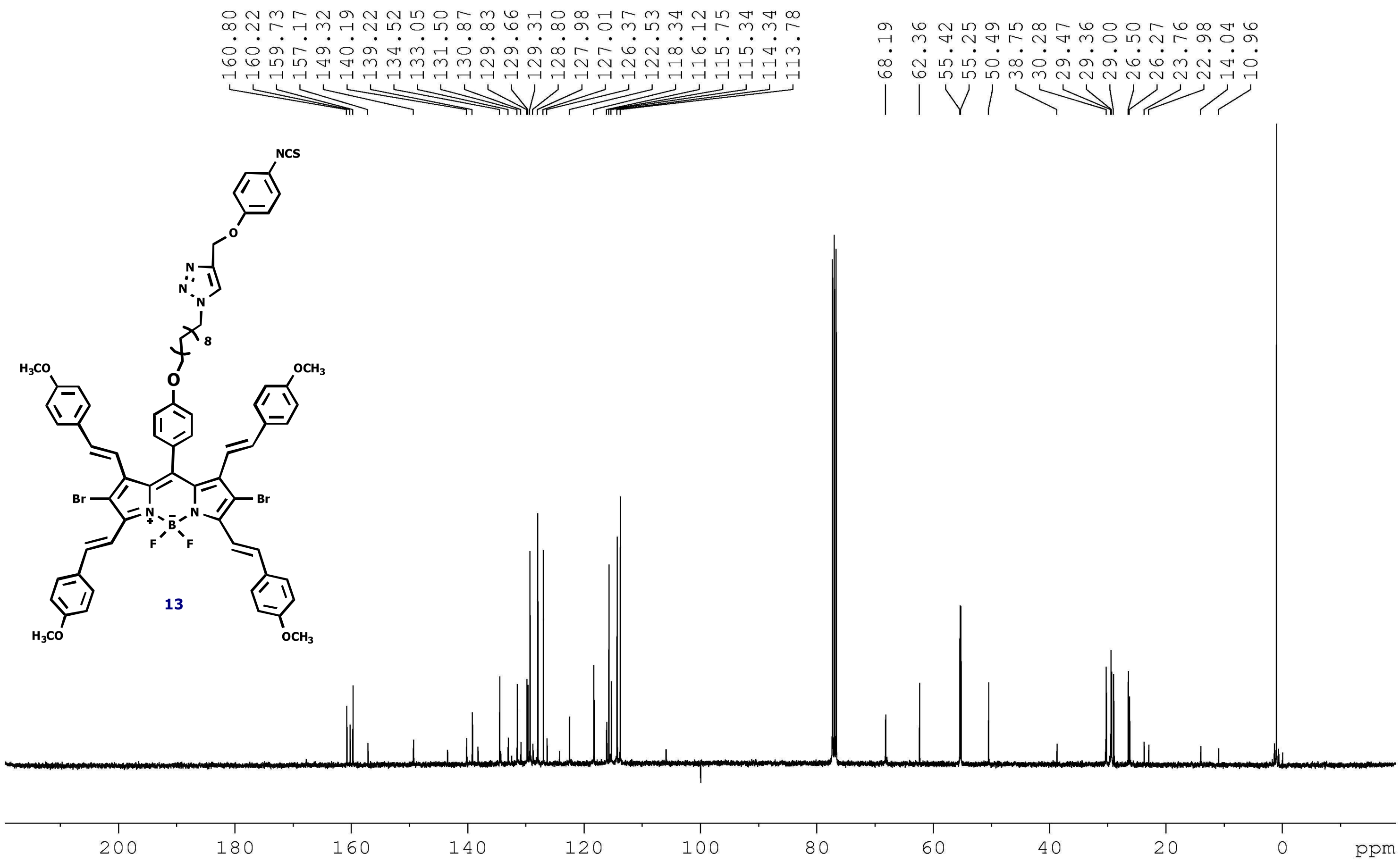

Figure 89: ^{13}C NMR Spectrum of Compound 13

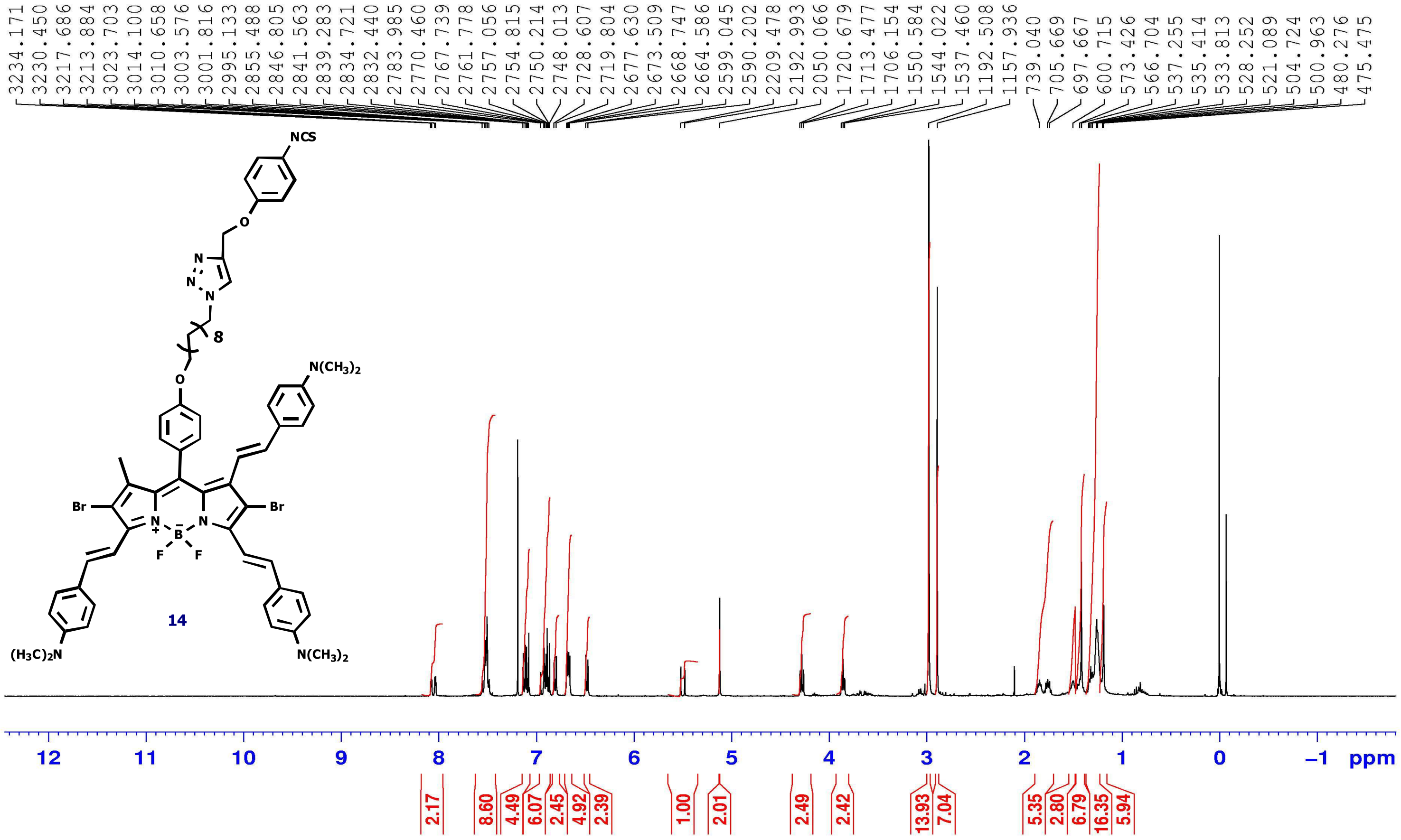

Figure 90: ^{1}H NMR Spectrum of Compound 14

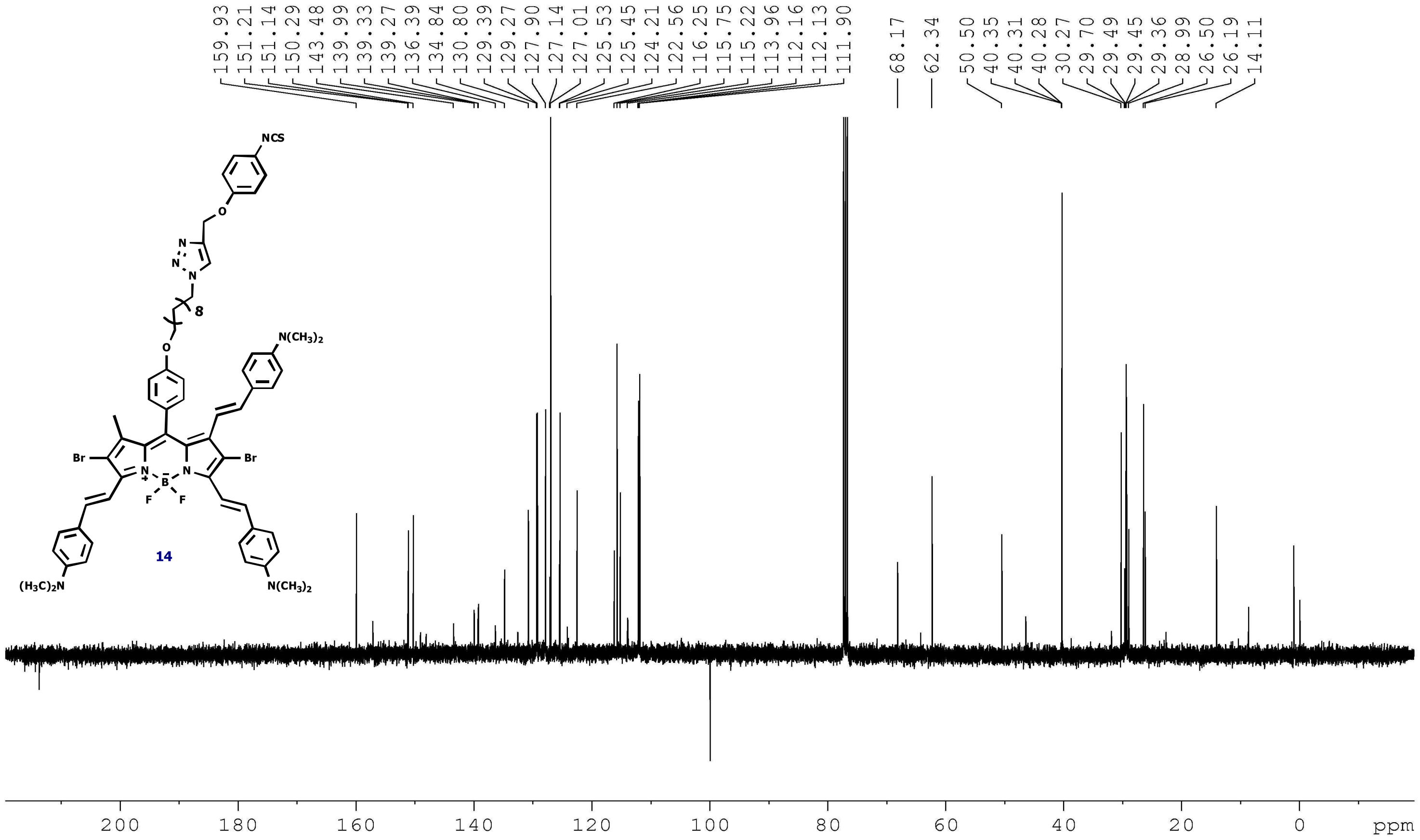

Figure 91: ^{13}C NMR Spectrum of Compound 14

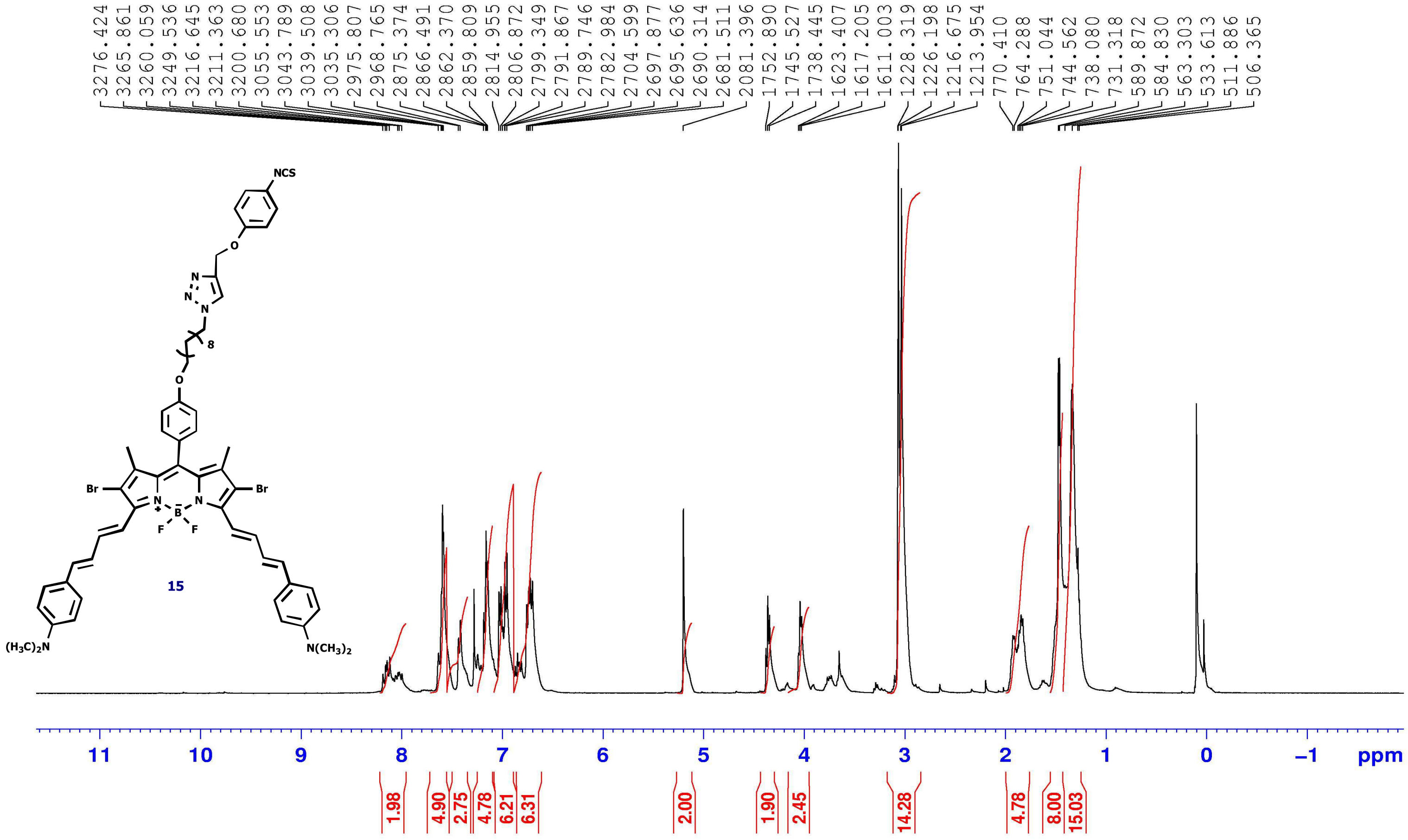

Figure 92: ^{1}H NMR Spectrum of Compound 15

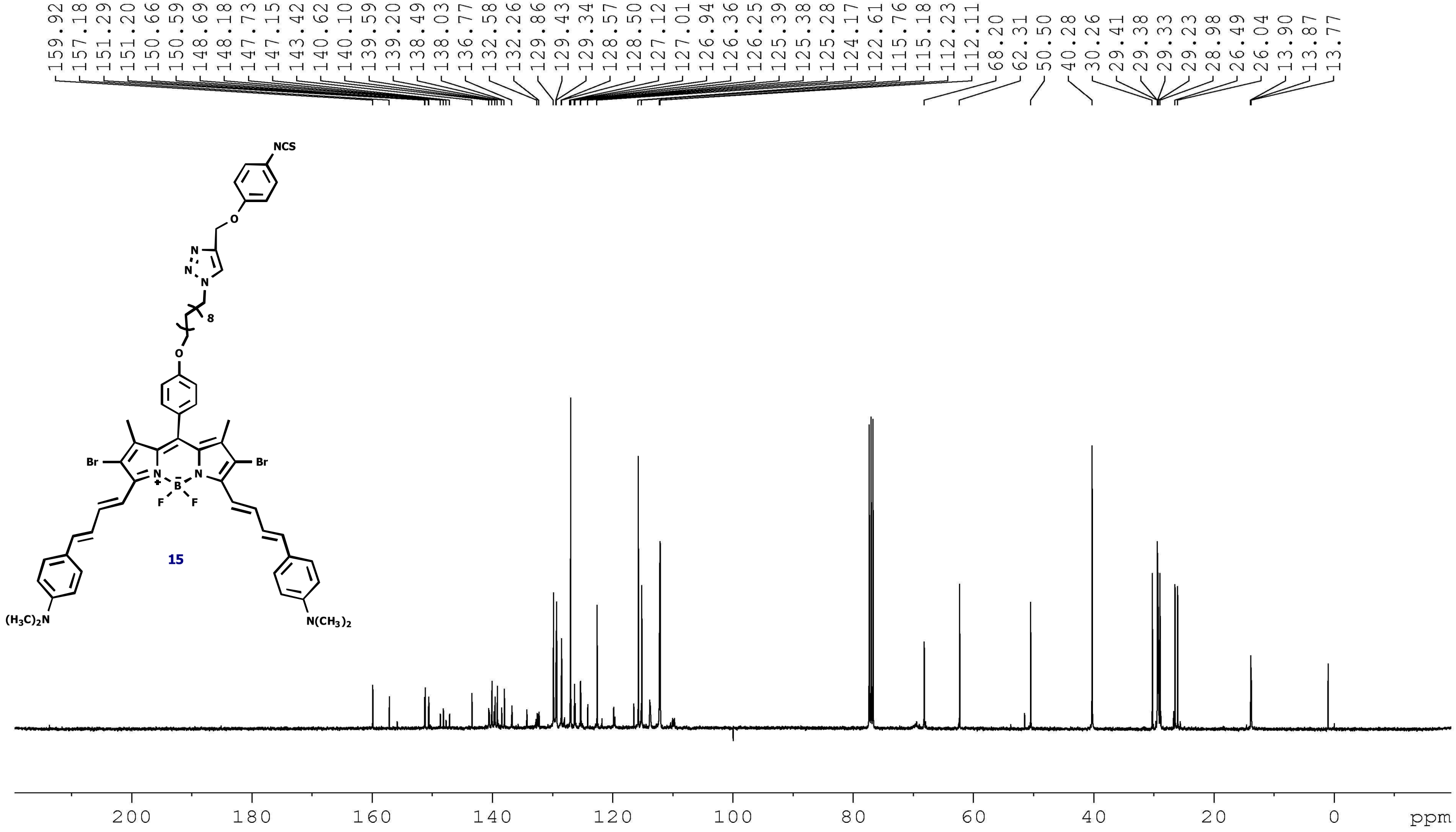

Figure 93: ^{13}C NMR Spectrum of Compound 15

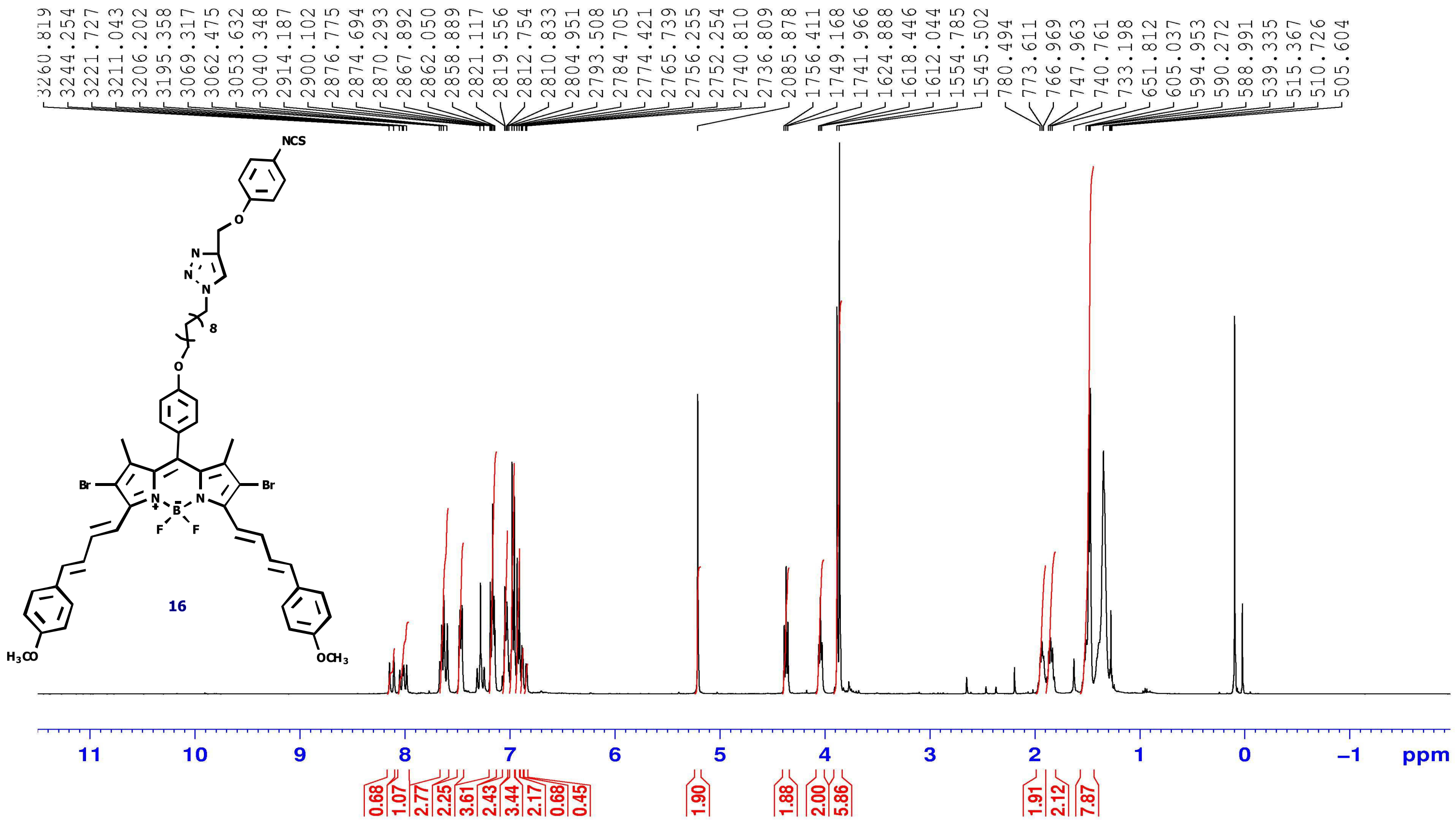

Figure 94: ^{1}H NMR Spectrum of Compound 16

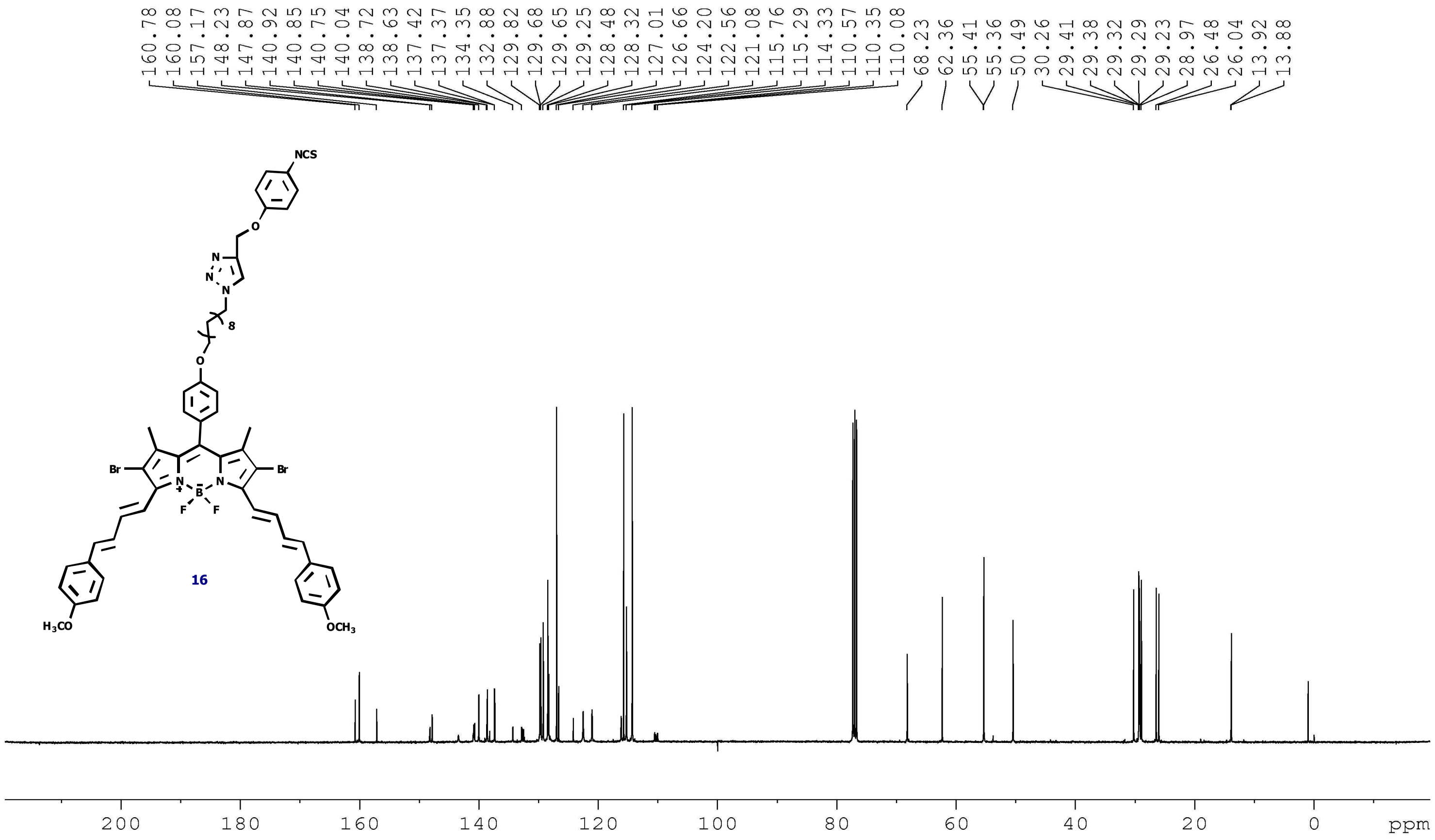

Figure 95: ^{13}C NMR Spectrum of Compound 16